



Selected Mechanical Properties of Polymeric Optical Fiber (POF)

Disertační práce

Studijní program: P3106 – Textile Engineering
Studijní obor: 3106V015 – Textile Technics and Materials Engineering
Autor práce: **Juan Huang, M.Eng.**
Vedoucí práce: doc. Dr. Ing. Dana Křemenáková





TECHNICAL UNIVERSITY OF LIBEREC
Faculty of Textile Engineering ■

Selected Mechanical Properties of Polymeric Optical Fiber (POF)

Dissertation

Study programme: P3106 – Textile Engineering
Study branch: 3106V015 – Textile Technics and Materials Engineering
Author: **Juan Huang, M.Eng.**
Supervisor: doc. Dr. Ing. Dana Křemenáková



Prohlášení

Byla jsem seznámena s tím, že na mou disertační práci se plně vztahuje zákon č. 121/2000 Sb., o právu autorském, zejména § 60 – školní dílo.

Beru na vědomí, že Technická univerzita v Liberci (TUL) nezasahuje do mých autorských práv užitím mé disertační práce pro vnitřní potřebu TUL.

Užiji-li disertační práci nebo poskytnu-li licenci k jejímu využití, jsem si vědoma povinnosti informovat o této skutečnosti TUL; v tomto případě má TUL právo ode mne požadovat úhradu nákladů, které vynaložila na vytvoření díla, až do jejich skutečné výše.

Disertační práci jsem vypracovala samostatně s použitím uvedené literatury a na základě konzultací s vedoucím mé disertační práce a konzultantem.

Současně čestně prohlašuji, že tištěná verze práce se shoduje s elektronickou verzí, vloženou do IS STAG.

Datum:

Podpis:

Acknowledgments

I am very grateful that Technical university of Liberec gives me this opportunity to carry out my doctoral study. With a sense of profound gratitude, I would like to express my heartfelt thanks to doc. Dr. Ing. Dana Křemenáková, prof. Ing. Jiří Militký, CSc., prof. Ing. Jakub Wiener, Ph.D. and doc. Ing. Michal Vik, Ph.D. for their inspiration, support, advice, encouragement, recommendations and fruitful guidance in bringing out this project into a successful end.

I would like to express my sincere gratefulness to prof. Ing. Jaroslav Šesták, DrSc., dr.h.c. from West Bohemian University of Pilsen as an opponent for my SGS projects, and for his cooperation and advices improving my whole study.

I would like to express my deep gratitude to Prof. Weilin Xu from Wuhan Textile University, China, Ing. Vít Lédl, Ph.D. from Toptec center in Turnov, Czech Republic and Prof. B.K. Behera from Indian Institute of Technology Delhi, India to provide me the internship opportunities.

I am very thankful to all laboratory colleagues of Faculty of Textile Engineering for their nice cooperation and assistance in carrying out the measurements, and especially to the workers in my department for their general assistance and cooperation for my study.

I am very thankful to all my friends here for their kind companionship, care and support.

I am deeply thankful to my family for their care and support behind.

Finally, I would like to express my thanks to the people who helped me directly or indirectly in my doctoral study and/or for my pleasant stay in Liberec.

List of Symbols

P	Applied indentation load
R_a	Average roughness
CI	Confidence interval
r_{core}	Constant core radius
k	Constant from power law fitting curve
h_i	Constant from power law fitting curve
a	Constant from power law fitting curve
m	Constant from power law fitting curve
b	Constant related to the slope of normalized $S-N$ curve, fatigue sensitivity coefficient
ϵ	Constant dependent on the geometry shape of the indenter
h_c	Contact depth
R^2	Coefficient of determination
θ_C	Critical incidence angle
h_s	Displacement of the surface at the perimeter of the contact during indentation
$n(r)$	Distribution of refractive index of fiber core
g	Earth acceleration
h	Elastic displacement of indenter
$Q(P_i)$	Empirical quantile function
d	Fiber diameter
h_f	Final depth
F_l	Flexibility
$\Gamma(x)$	Gamma function
l	Gauge length
T_g	Glass transition temperature
H	Hardness
t_H	Holding time during nanoindentation
θ_l	Incidence angle

C_f	Load frame compliance
t_L	Loading time during nanoindentation
k_2	Material constant
e	Mathematical constant
P_{max}	Maximum applied load
θ_{max}	Maximum incidence acceptance angle
σ_{max}	Maximum stress
σ_m	Mean stress level
T_m	Melting temperature
σ_{min}	Minimum stress
\dot{h}	Nominal displacement rate
N	Number of fatigue cycles
N_m	Number of measurements
NA	Numerical aperture
σ_a	Peak of applied pretension stress
ν_i	Poisson's ratio of the indenter
ν	Poisson's ratio of the sample
m	Pretension weight
P_i	Probability of fiber failure
A	Project area of elastic contact
α_c	Ratio of elaborated fatigue strength to ultimate tensile strength
χ_{red}^2	Reduced chi-square
E_r	Reduced modulus
l_0	Reference length
θ'_1	Reflective angle
θ_2	Refractive angle
n	Refractive index
n_a	Refractive index of air
n_{clad}	Refractive index of fiber cladding

n_{core}	Refractive index of fiber core
n_1	Refractive index of medium 1
n_2	Refractive index of medium 2
R_q	RMS roughness
s	Safe spacing between adjacent indentations
C_s	Sample compliance
W_2	Scale parameter in Weibull distribution
W_3	Shape parameter in Weibull distribution
W_1	Shift parameter in Weibull distribution
SD	Standard deviation of mean value
S	Stiffness
$\dot{\epsilon}$	Strain rate
σ	Stress acting nominally in a direction perpendicular to the sample surface during indentation
σ_s	Stress amplitude
n	Stress exponent
$\Delta\sigma$	Stress range
R	Stress ratio
$QT(P_i)$	Theoretical quantile function
t_i	Time when the creep displacement occurs initially
C	Total measured compliance
h_{max}	Total depth or maximum depth
σ_{uts}	Ultimate tensile strength
CV	Variation coefficient of mean
r	Variable core radius
C_m	Velocity of a light wave in a medium
C_v	Velocity of a light wave in vacuum
w	Width of nanoindentation on the sample
m_r	Weibull sample moment
$P(x)$	Weibull distribution

E_i	Young's modulus of the indenter
E	Young's modulus of the sample

List of Abbreviations

ASTM	American society for testing and materials
CVD	Chemical vapor deposition
DVD	Digital versatile disc
DMA	Dynamic mechanical analysis
EMI	Electromagnetic interference
EA	Ethyl acetate
EVA	Ethylene-vinylacetate
FTTD	Fiber to the desk
FTTH	Fiber to the home
FTIR	Fourier transform infrared spectroscopy
GI	Graded-index
HTS	Holding time sensitivity
LCD	Liquid crystal display
LRS	Loading rate sensitivity
PFEP	Perfluoroethylenepropylene
PA 6	Polyamide 6
PC	Polycarbonate
PET	Polyester
PE	Polyethylene
POF	Polymeric/plastic optical fiber
PMMA	Poly(methyl methacrylate)
PFA _s	Poly(fluoroalkyl acrylates)
PS	Polystyrene
PTFE	Polytetrafluoroethylene

PU	Polyurethane
PVC	Polyvinylchloride
PDT	Photodynamic therapy
Q-Q	Quantile-quantile
UV	Ultraviolet
RFI	Radio frequency interference
RMS	Root mean square
SEM	Scanning electron microscopy
SI	Step-index
3D	Three-dimensional
2D	Two-dimensional

Content

Chapter 1 Introduction	1
1.1 History of POF.....	1
1.2 Development and applications of POF fabrics	2
1.2.1 Luminous fabrics	2
1.2.2 POF fabric sensors	4
1.3 Advantages and disadvantages of POF fabrics	4
1.4 Present state of problem.....	5
Chapter 2 Objectives	6
2.1 Major objectives.....	6
2.2 Introduction of thesis frame	6
Chapter 3 State of the Art	8
3.1 Basics of POF	8
3.1.1 Total internal reflection.....	8
3.1.2 Numerical aperture.....	9
3.1.3 Classification of POF.....	9
3.1.4 Structure and materials of POF.....	12
3.1.5 Attenuation mechanism of POF.....	14
3.1.6 Manufacturing techniques of POF	15
3.2 Side illumination of POF	18
3.2.1 Review from literatures.....	18
3.2.2 My state of the art	20
3.3 Nanoindentation properties of polymers.....	20
3.3.1 Introduction of indentation	20
3.3.2 Basic principles of Oliver and Pharr method.....	23
3.3.3 Creep from nose phenomenon	26
3.3.4 Strain rate	27
3.3.5 Applications in interphase properties.....	28
3.4 Fatigue properties of single fiber	29
3.4.1 Introduction of fiber fatigue.....	29

3.4.2 Theory of fatigue.....	30
3.4.3 Fatigue testing methodology.....	31
3.4.4 Analysis of fatigue testing	35
Chapter 4 Experimental Materials and Methods	40
4.1 Materials	40
4.2 Methods.....	40
4.2.1 Tensile testing	40
4.2.2 Strength distribution.....	40
4.2.3 Nanoindentation testing	41
4.2.4 Tension fatigue testing.....	43
4.2.5 Flex fatigue testing.....	44
4.2.6 Scanning electron microscopy	46
4.2.7 Fourier transform infrared spectroscopy.....	46
Chapter 5 Results and Discussion	47
5.1 Tensile properties.....	47
5.2 Strength distribution.....	49
5.3 Nanoindentation properties	53
5.3.1 Surface roughness	53
5.3.2 Loading rate effect on nanoindentation creep.....	54
5.3.3 Holding time effect on nanoindentation creep.....	58
5.3.4 Fiber diameter effect on hardness property	59
5.3.5 Interphase property	61
5.4 Tension fatigue properties.....	64
5.4.1 Extension response under constant stress amplitude	64
5.4.2 Tensile property after tension fatigue testing.....	66
5.5 Flex fatigue properties	70
5.5.1 Bending resistance	70
5.5.2 Flex fatigue behavior	76
Chapter 6 Conclusion and Outlook.....	81
6.1 Conclusion from experiments	81

6.2 Other findings	82
6.2.1 Fluorescent fabrics	83
6.2.2 Lensed POF.....	84
6.3 Future work.....	84
Chapter 7 References.....	86
Chapter 8 Publications	96
8.1 Publications in journals.....	96
8.2 Publications in book chapters	96
8.3 Publications in conferences.....	97
<i>Annex I</i>.....	100

Summary

The integration of polymeric optical fiber (POF) into fabrics has brought a lot of interest in textile design, on the other hand, it also displays the profiles of human beings, animals, objects (warning devices), obstacles (steps and carpets) and the like in places with poor visibility. However, this integration is facing huge problems. The major problems are derived from the poor flexibility, drapability, durability and side illumination of POF fabrics. The Properties of POF are considered as the critical factors which would influence the manufacturing processes and properties of POF fabrics. Compared with traditional textile yarns or filaments, POF is relatively brittle, stiff, and sensitive to bend due to its thick diameter. At present, the diameter of end emitting POF in weaves, knits and embroideries is generally in the range of 0.2 ~ 1.0 mm, the diameter of side emitting POF applied in safety applications (corridors and obstacles) varies in the range of 2 ~ 6 mm or above. The big challenge is to manufacture POF with sufficient flexibility and good side illumination intensity. The side illumination intensity of POF is usually enhanced by surface modifications (chemically and mechanically) or using the fluorescent fabric cover which could also protect the naked POF from mechanical damage and UV radiation and improve the comfort of POF.

This thesis work is aimed to investigation the selected mechanical properties of POF based on the less contributions from the standpoint of the properties of POF integrated fabrics at present, rather than propose new methods to improve the side illumination of POF or propose new manufacturing techniques of POF fabrics. The experimental work starts from tensile testing and the results indicate that, there is an inverse relation between fiber diameter and tensile strength of POF. The strain value decreases as the fiber diameter increases. And the modulus varies significantly and is assumed to be determined by the various changes of tensile strength and strain. As a synthetic polymer fiber, however, POF is not uniform in fiber thickness, the results from strength distribution represent that the gauge length plays an important role in tensile strength. The results evaluated by Weibull distribution indicate that there is a decay exponential relation between tensile strength and gauge length. POF is with the core/cladding structure. The contributions of core and cladding to the mechanical properties of the whole fiber, and the interphase property between core and cladding are investigated by nanoindentation technique. It is observed from the experimental data that the core is harder than the cladding. Both core and cladding show very strong loading rate sensitivity during nanoindentation testing, which could be explained by the visco-elastic properties of polymers. The interphase width is estimated to be in the range of 800 ~ 1600 nm roughly. In the investigation of POF durability, two fatigue testing are taken into account. One is the tension fatigue testing which is applied to measure the strain response of POF under constant stress amplitude. The results demonstrate that both cyclic extension and total extension go up with increasing fatigue cycles. Compared with other fibers, while, 0.5 mm POF has higher total extension but lower cyclic extension than thicker POFs, which could be explained by different applied external stress and different amount of irreversible deformation in each fiber during

fatigue testing. Another is the flex fatigue testing, which is aimed to investigate the flex fatigue lifetime based on the number of bending cycles to break by using the model of fatigue life curve. It is estimated that the fatigue lifetime could be influenced significantly by the testing condition such as the bending angle and speed. In the meanwhile, the flex fatigue sensitivity coefficient is also evaluated and compared with the general value for other materials.

Keywords:

polymeric optical fiber; strength distribution; nanoindentation properties; tension fatigue; flex fatigue

Anotace

Integrace polymerních optických vláken (POF) do textilií je přínosem z hlediska designu na jedné straně, ale na druhé straně umožňuje také zviditelnění obrysů osob, zvířat, předmětů, vymezení překážek (schody, kraje koberců) apod. Při zabudování optických vláken do textilií se sleduje zejména jejich ohebnost, trvanlivost a intenzita vyzařování. Ve srovnání se standardními textilními materiály (příze, hedvábí) jsou některá POF relativně křehká, tuhá a citlivá na ohyb v závislosti na jejich průměru. V současné době je průměr běžně využívaných POF pro tkaniny, pleteniny a výšivky v rozmezí od 0,2 do 1,0 mm. Pro integraci do oděvních textilií s cílem zviditelnění osob lze použít stranově vyzařující optická vlákna o průměru 2-6 mm a např. Pro osvětlení chodeb a vymezení překážek je možno použít optická vlákna o průměru od 6 mm výše. Pro uvedené aplikace je nutno vždy hledat kompromis mezi dostatečnou ohebností a světelným výkonem vláken. Pro zvýšení intenzity vyzařování se používá pokrytí povrchu stranově vyzařujících vláken textilním potahem. Vlákna jsou umístěna v dutině tkaniny nebo opletena textilními přízemi. Textilní potah současně chrání optické vlákno před mechanickým poškozením a vlivem UV záření a zvyšuje komfort při nošení.

Disertační práce je zaměřena na zkoumání vybraných mechanických vlastností POF. Experimentální práce je založena nejprve na zkoumání tahových vlastností stranově vyzařujících optických vláken v závislosti na jejich průměru. S rostoucím průměrem vlákna se relativní pevnost a tažnost snižuje. Modul optických vláken se mění významně spolu se změnami pevnosti a tažnosti. Podobně jako u syntetických polymerních vláken ovlivňuje také upínací délka pevnost polymerních optických vláken. Výsledky získané na základě Weibullova rozdělení indikují exponenciální pokles pevnosti v závislosti na upínací délce. POF mají strukturu jádro/plášť. Příspěvek této struktury i vlastností na rozhraní povrchů mezi jádrem a pláštěm k mechanickým vlastnostem POF byl zkoumán s využitím nanoindentační metody. Bylo zjištěno, že jádro POF je tvrdší než plášť. Obě komponenty, jak jádro, tak i plášť indikují velmi silnou citlivost na rychlosti zatěžování v průběhu nanoindentačního testu, která může být popsána pomocí visko-elastických vlastností polymerů. Odhad šířky mezifáze je přibližně v rozmezí od 800 ~ 1600 nm. Při hodnocení ohebnosti a životnosti (únavy) POF, byly vzaty v úvahu dva typy testování. Nejprve bylo testováno cyklické namáhání založené na měření deformační odezvy POF na konstantní amplitudu zatěžování. Výsledky ukazují, že jak cyklické protažení, tak i celkové protažení souvisí s přírůstkem únavových cyklů. Ve srovnání s jinými vlákny vykazuje POF o průměru 0,5 mm vyšší celkové protažení, ale nižší cyklické protažení, než POF s větším průměrem. To by mohlo být vysvětleno různým množstvím nevratné deformace každého vlákna v průběhu testování únavy. Dále bylo provedeno testování odolnosti v ohybu dle počtu ohybových cyklů do přetrhu. Bylo ukázáno, že tato veličina je významně ovlivněna podmínkami testování, což je úhel ohybu a rychlost. Byl hodnocen také koeficient ohybové citlivosti a porovnán s hodnotami běžnými pro jiné materiály.

Klíčová slova:

polymerní optické vlákno, rozložení pevnosti, nanoindentační vlastnosti, únava při cyklickém namáhání v tahu, únava při opakovaném namáhání v ohybu

摘要

塑料光纤在织物中的应用给纺织领域带来了极大的兴趣和更多的可能性。这不仅仅促进了发光织物的发展，同时也是两个学科的结合。然而，塑料光纤在织物中的应用同时也面临着颇多问题。其中最主要的问题来自于塑料光纤织物的柔韧性，悬垂性，耐久性和发光性能。这些问题的存在归根究底在于塑料光纤本身的性能。塑料光纤的性能直接影响了塑料光纤织物的生产和产品的最终性能。与传统的纺织纱线或长丝相比，纺织用的塑料光纤由于直径比较粗导致其脆且硬，同时对弯曲非常的敏感。目前，应用于纺织中的塑料光纤的直径一般在 0.2 ~ 1.0 毫米范围内。如果降低塑料光纤的粗细，其发光性能也会降低。目前，要想生产出细且发光性能好的塑料光纤，仍然是一个巨大挑战。因此，这就使得对塑料光纤性能的研究显得尤为重要。不仅可以给制造商提供一些实验数据的参考，同时对塑料光纤与纺织品更好的结合和未来的研究提供更丰富的信息。

这篇论文的主要目的是对塑料光纤一些尚未被深入研究的机械性能进行探讨，而不是提出一种新的方法去提高塑料光纤通体发光性能或阐述一种新的塑料光纤织物的生产技术。实验首先研究了塑料光纤的基本拉伸性能，探讨纤维直径对拉伸性能影响。实验结果表明随着塑料光纤直径增加，拉伸强度和拉伸变形或伸长都随之降低。前者的变化可以用弱节理论来解释，当纤维越粗时，纤维表面积越大，表面所包含的缺陷更多，导致拉伸断裂的几率越大。后者变化归因于在拉伸速率一定的情况下，粗纤维的伸长率更低。模量的变化相对较随机，主要是因为模量值的大小取决于拉伸强度的变化与拉伸变形的变化的比值。随后研究了纤维长度对拉伸性能影响。纤维长度对拉伸性能的影响与纤维粗细对其的影响相似。实验结果采用了韦伯分布对拉伸断裂概率分布进行模拟，同时也对纤维长度与拉伸强度之间的关系进行了模拟。塑料光纤具有皮芯双层结构，皮和芯对整根纤维性能的贡献也值得研究。采用纳米压痕技术研究了皮和芯各部分的机械性能，并讨论了塑料光纤本身的粘弹性对纳米压痕实验的影响和塑料光纤皮芯界面的性能。实验表明塑料光纤皮芯界面可能在 800 ~ 1600 纳米范围内。塑料光纤的柔韧性和耐久性采用了疲劳试验进行研究。其中拉伸疲劳试验主要讨论了在一定的应力幅度情况下塑料光纤的应变变化。实验结果得出随着疲劳周期的延长，塑料光纤的每个循环中的应变和总应变都是随之增加。然而与更粗的塑料光纤相比，0.5 毫米的塑料光纤表现出最大的总应变和最小的每个循环中的应变。这有可能是因为每种纤维所受的应力和不可逆的变形不同所导致的。另外一个疲劳试验是弯曲疲劳，着重于对塑料光纤疲劳寿命的研究。实验结果采用韦伯分布来探讨弯曲疲劳测试中纤维断裂的概率分布。同时采用疲劳寿命曲线对塑料光纤的寿命进行模拟，最后计算出塑料光纤弯曲疲劳敏感性系数。

关键词:

塑料光纤；强度分布；纳米压痕性能；拉伸疲劳；弯曲疲劳

Chapter 1 Introduction

1.1 History of POF

A new word called “E-era” is sweeping the whole world due to the conformation of the global village by internet. The transmission of data information from one place to another provides a non-distance communication. The previous major medium for data communication is copper wire, which has been applied as an electric wire since the invention of electromagnet and telegraph in the 1820s [1, 2] and considered as an electrical conductor since the introduction of telephone in 1876 [3]. Copper wire was gradually taken placed by optical fiber due to the effective data communication. Transmitting data information over an optical fiber has a multitude of advantages than over a copper wire. To begin with, the optical fiber is non-conducting, that means, it is safe in all electromagnetic situations and free radio frequency interference (RFI). Besides, the optical fiber works at low voltage. Even a broken or damaged optical fiber would only release a few power, with low temperature. Furthermore, an optical fiber is relatively lighter and can transmit higher bandwidth than a copper wire.

The principle of guiding light by refraction through an optical fiber was initially demonstrated in the early 1840s [4]. Whereas, the optical fiber was widely used as a medium for data communication after more than 100 years due to its increasing quality and decreasing cost, nowadays, it merely takes seconds to transmit data information from the largest libraries. Apart from data transmission, the application fields of optical fiber extend broadly because of the visible merits. For instant, the optical fiber is separated from the light source (diode), making the replacement of light source easy. The optical fiber is controlled without environmental impact, leading to the usage even in the areas with fire or explosion or water [5].

Optical fiber can be generally classified into two categories: glass optical fiber and polymer/plastic optical fiber (POF). Compared with glass optical fiber, POF is easy to handle due to its large numerical aperture, flexibility, light weight, and resistances to impact and vibration. Whereas, POF is sensitive to bend, represents low thermal resistance and high optical attenuation [6].

POF, made of polymers or plastics, was firstly introduced in the 1960s as a substitution of glass optical fiber in data communication in a short distance generally less than 1 km. POF was not utilized universally due to its high optical attenuation. However, POF has received enough attention in the 1990s because of the development of graded-index POF and the achievement of low attenuation [7-10], combined with the successive improvements in both transparency and bandwidth, POF is recently applied as a high-capacity transmission medium [11]. At present, the applications of POF have increased significantly. Apart from the application in data transmission, POF is widely used in optical components (such as optical switches, amplifiers and tunable optical sources), and other extended fields. Some application fields are introduced here,

- Fiber optic network: fiber to the home (FTTH), fiber to the desk (FTTD), etc.
- Auto applications: in-car communications, in-car audio-visual entertainment system, etc.
- Electronic and sensors: computers, digital versatile disc (DVD), etc.
- Industrial control bus system: POF can be connected to the standard protocol interface by converter.
- Lighting and solar energy utilization: interior illumination, waterscape lighting, road lighting, etc.
- Military communications: soldiers' wearable lightweight computer systems, head mount display, etc.
- Therapy: cancer, skin diseases, etc.
- Textiles: luminous cloths, lighting curtains, etc.

1.2 Development and applications of POF fabrics

Textiles can be classified into three categories based on the end uses: clothing textiles, decorative textiles and technical textiles. The demand for textiles has increased dramatically during the last two decades due to the rise in living standard of human beings. However, the increasing demand has brought a big challenge to develop new materials or introduce existed materials to textiles. Even though glass fiber based textile materials have been known for quite a long period of time, the idea of optical fiber based fabrics was arose at the end of twentieth century. The initial optical fiber based fabrics were manufactured for end illumination by cutting the optical fiber at the required point of light emission. Visually, the optical effect on POF based textile fabrics was purely aesthetic. The color, brilliance or shine of POF fabric could be changed from the light reflection on fabric surface with different fiber materials, fabric pattern and fabric density [12]. Recently, following with the development of POF itself and the manufacturing techniques of POF fabric, POF integrated textiles have extended the applications from the photo-metric fields for illumination to the radiometric fields for sensing [13].

At present, there are two major applications of POF in textile fabrics. One is utilized as an active lighting element in fabric structure for lighting purpose, another is used as an optical sensor in fabric structure for sensing purpose. Selected applications regarding these areas are introduced as follows.

1.2.1 Luminous fabrics

Indoor lighting

POFs are designed to be incorporated (woven/weft knitted/embroidered) into fabrics. Once the end of POF is connected to light source, POF fabrics could light up not only on the selected

locations but also laterally on fabric surface. It generates new applications apart from telecommunications. This integration of POF into fabrics creates flexible optical systems, giving opportunities of POF fabrics in indoor lighting applications, such as table cloths for home decoration, curtains for stage decoration as well as cushions for car decoration [14].

Outdoor lighting

POF fabrics with thick POFs have more possibilities for architectural applications: public premises like warning devices, animation apparatuses, and garden decoration as well [15].

Safety

Compared with illuminated panels with fluorescent or reflective materials, POF fabrics exhibit superior active illumination intensity, which explores enormous potential in safety applications. The main application in safety field is the clothes and accessories for policemen, firemen and sportsmen [16]. It is also realized that POF fabrics would contribute significantly to emergency exits, transportation signs, warning devices, and interior equipments in cars.

Fashion and design

The fashionable clothing with POF fabrics brings a lot of virtual enlightenment. POF fabrics used to be designed significantly for clothes and accessories, now it is not a challenge to design POF fabrics into high heels based on the present textile processing technology [17]. Besides, POF fabrics are popular in industrial art products and decoration items like flowers and curtains, which are especially suitable for places with very poor light illumination.

Displays

The idea of flexible display with POF fabrics was initiated around four decades ago. The application was firstly involved in liquid crystal display (LCD) with the backlight system [18] that was made of laminated woven fabrics integrated with POFs. Other flexible flat panel displays [19] were developed afterwards. In the early of twenty-first centuries, a graphically communicative clothing with flexible woven display was established for both static and animated graphics [20]. At present, two-dimensional (2D) flexible displays based on POF fabrics have obtained more interest due to the thin and light fabric structure, drapability, bendability and manifold 2D design prospects [21]. However, the processing of POF fabrics is still problematic due to the insufficient flexibility of POF, and the resolution of fiber grid in fabric structure is not satisfied for high-definition displays [22]. A concept of highly flexible POF made of silicone fibers was introduced [23], however, this kind of POF is usually used for smart clothing in terms of its low optical transparency [24].

Medical technology

Relative homogeneous distribution of light intensity was obtained with a stain weave fabric pattern by French National Institute of Health and Medical Research (INSERM) or in embroidered POF fabrics [25]. The homogeneous distribution of flexible fabric provides the

potential in medical field, for instant, photodynamic therapy (PDT). PDT is a treatment for certain kinds of cancer (pre-malignant or early-stage cancer). The cancer cells could be eradicated by using a photosensitizing agent first and then the radiation treatment of laser light [26] or textile light diffuser [27] with a specific wavelength. The homogeneous distribution of light from POF fabric surface could be also applied onto the uneven surface of human beings to heal the skin diseases.

1.2.2 POF fabric sensors

POF sensors and devices have been reported for a long period of time. POF fabric sensors have been recently popular to transfer signals to processor units for detection [28] or monitoring [29]. There are three general principles of POF fabric sensors [30]. First, the mechanical fluctuations (pressure, stress, strain) onto POFs lead to the microbends and macrobends of POFs. Second, the additives in POF core or cladding material interact with the environment. Last but not the least, the geometrical optical alterations change the light guidance of POF. In all cases, the transmitted light intensity of POF varies in order to measure the required parameters.

Generally, the textile integrated POF sensors are aimed at measuring the physical responses such as pressure [24], stress [31] and strain [32], or applied for biomedical responses based on biological parameters such as breathing [33], sweat [34] and oxygen content [29].

1.3 Advantages and disadvantages of POF fabrics

There are numerous advantages of integrating POFs into traditional fabric structures. First of all, POFs make the fabrics luminous. POF fabrics could emit light not only on the fabric surface but also at required points based on the macrobends of POF or additional surface modifications. In contrast to general electrical products, POF fabrics are immune to electromagnetic interference (EMI), free of electricity and heat. At the same time, POF fabrics can still keep the textile appearance. The dimension of luminous area is flexible, which could be small in centimeters for embroideries or large in meters for weaves and weft knits. Additionally, the separation of light source and POF medium generates simple connection and easy handling of POF fabrics. Furthermore, the use of POFs instead of glass optical fibers in luminous fabrics is beneficial to the flexibility, light weight, durability and small injuries [35].

On the other hand, POF fabrics have some disadvantages. Even though POF fabrics are popular in illumination, decoration, radiation and sensing applications, a lot of potential applications are highly restricted due to the limitations of POF itself. The bendability of POFs is not sufficient enough as traditional yarns, which limits a lot of possibilities in structure design. Thin POFs with side illuminating effect are not commercially available on the market due to the complicated manufacturing processing and poor transmission rate of light rays. In addition, the mechanical properties of POFs are not satisfied at sub-zero temperature. The thermal

stability of POFs is problematic that limits the working temperature significantly. Furthermore, it is still a challenge to reduce the optical loss of POFs.

1.4 Present state of problem

As mentioned above, there are a great deal of applications of POFs in textiles. In the field of POF fabrics, a lot of potential has been restricted by the properties of POF, which not only influence the illumination properties of POF fabric, but also limit the possibilities of integration of POF into fabrics. For example, it is still problematic to commercially manufacture side emitting POFs with diameter less than 0.2 mm. Even though POFs with diameter more than 1 mm could be used as active illuminating elements in emergency or safety textiles in order to give enough light rays in special dark places [16]. The possibility to apply POFs into traditional fabric structures is obviously lower with thicker POFs. Moreover, the bendability of POFs, the technique processing of POF fabric, the illuminating effect, the drapability of POF fabric are influenced by POF properties more or less.

In practical illumination and decoration applications of POF fabrics, the POF diameter used as traditional textile yarns or fibers normally varies from 0.2 mm to 1 mm. In order to obtain clear luminous patterns, the illuminating effect is generally achieved by the macrobends or additional treatments of POFs in woven, weft-knitted and embroidered fabric structures. Generally speaking, in weaves, POFs are laid straightly, the light illumination is obtained by surface modifications and the light loss is quite low; in weft knits (knitted webs/meshes), POFs are arranged in bending shapes, the light illumination is obtained by macrobends and the light loss is higher compared to the first case; while in embroideries, POFs are either bent or set in any free form, the light illumination is achieved by macrobends of POFs and the light loss is highest in all cases. Both mechanical properties and light loss restrict the dimension and market prospects of POF fabrics.

A lot of contributions have been devoted to the manufacturing technology of POF fabrics, the enhancement of side illumination of POFs or POF fabrics, and the improvement of optical loss of POFs induced by mechanical deformations (tensile, bend or compression) of POF. It seems that how to develop the POF fabrics and how to obtain high intensity lateral light on POF fabrics have been catching more attention. However, how the POF properties influence the development and properties of POF fabrics is also very interesting and vital. There are very less literatures focusing on the mechanical properties of POF with a core/cladding structure, the flexibility and the durability of POF itself in details so far, which are important and unresolved issues required to be explored urgently.

Chapter 2 Objectives

2.1 Major objectives

As a synthetic polymeric fiber, POF is expected to be uniform in thickness. As a matter of fact, the fiber diameter, the cladding thickness, as well as the surface roughness are not the same in the direction of fiber length due to the manufacturing processes, packing processes and so on. These variations are difficult to control and could have unexpected effects on the mechanical and optical properties of POF. Thus, the tensile properties of POF in terms of the fiber diameter effect is discussed first. Then, the strength distribution of POF is considered with respect to different gauge lengths in tensile testing.

In order to figure out the contribution of each part (core or cladding) to the properties of the whole fiber, the local mechanical properties of both core and cladding are studied by using nanoindentation technique, and the nanoindentation creep deformation are also taken into account in details due to the inherent visco-elasticity of polymer materials. Apart from the core and the cladding, the interphase between them is also important and investigated by nanoindentation. The dimension or transition zone of interphase is estimated according to the changes of hardness and modulus from cladding to core.

Furthermore, POF subjects to repetitive external forces such as stretches and bends in practical uses. The durability of POF is inevitable to take into account. Two fatigue tests regarding the fiber durability are involved. The tension fatigue testing is mainly to estimate the strain response under constant load amplitude. Then the tensile properties after tension fatigue testing without fiber fracture are discussed. Another is flex fatigue testing, which is measured by Flexometer. The life time of POF is evaluated based on the number of bending cycles to fiber break and the fatigue life curve is obtained consequently. Afterwards, the flex fatigue sensitivity coefficient is estimated based on an empirical equation.

In a word, there are five aspects in mechanical properties selected to study in total: tensile properties, strength distribution, local mechanical properties of both core and cladding and the interphase property between them, tension fatigue properties and flex fatigue behaviours. The goals of this work are to survey the selected mechanical properties of POF which are referred in the applications of POF fabrics and discussed from the point of view of textile background, rather than to offer detailed and standard methodologies to investigate the mechanical properties of POF, or provide new methods of improvement of POF attenuation, or propose new technologies to manufacture POF fabrics. It is aimed to introduce POF to textile fields, present basic and important knowledge of POF itself regarding mechanical properties, and provide links to future for better research work and boarder applications in textiles.

2.2 Introduction of thesis frame

To set the stage, we begin with a brief introduction of POF in Chapter 3, including the basic theory of light propagation in POF, the structure and materials of POF, and the attenuation mechanism of POF. We also introduce the manufacturing techniques of POF in order to provide the general understanding of structured fiber formation of POF. Nowadays, the side illumination of POF has obtained more attention, and a lot of efforts have been made to improve the side illumination of POF. One part of my PhD work is presented here to provide another possibility to enhance the side illumination of POF. Afterwards, we mainly review the selected mechanical properties of POF from previous literatures. We initially introduce the basic principles of nanoindentation testing in terms of local mechanical properties of materials. In addition, we discuss the strain rate during nanoindentation for better understanding of the time-dependant deformation and viscoelasticity of polymers. Then we review the theory of fatigue testing, followed by the testing methods and the analysis based on modelling of fatigue testing.

In Chapter 4, we mainly introduce the materials and methods employed for selected mechanical tests in this thesis work.

In Chapter 5, we initially discuss the effects of fiber diameter and gauge length on the tensile property and the strength distribution of POF, respectively. The nanoindentation properties of POF in regard to the local mechanical properties of both core and cladding, the creep deformation and the interphase property between two parts. Then we analyze the results from both tension fatigue testing and flex fatigue testing based on the strain response and *S-N* curve, respectively.

In Chapter 6, we summarize all the results from Chapter 5, present other findings from my PhD study such as the utilization of fluorescent fabric to enhance and even the side illumination of POF and the development of lensed POF by laser treatment to improve the light gathering or light distribution of POF, finally, we introduce the future work that will be considered next.

In Chapter 7, we list all the references clearly.

In Chapter 8, we present all the publications in journals, books and conferences.

Chapter 3 State of the Art

3.1 Basics of POF

3.1.1 Total internal reflection

The ratio of the velocity of a light wave in vacuum C_v to the velocity of a light wave in a medium C_m is described as the refractive index n of the medium and is presented as:

$$n = \frac{C_v}{C_m} \quad (3.1)$$

If there are two semi-infinite media (thin medium 1 and thick medium 2), the corresponding refractive indices n_1 and n_2 have the relationship: $n_2 > n_1$. It is assumed that a light ray passes from the optically thin medium 1 under an angle θ_1 (from the normal to the interface) to the optically thick medium 2 through an interface between these two media. Then a part of the incident energy is reflected back into the medium 1 under the same angle θ'_1 and a part of it is refracted into the medium 2 under the angle θ_2 . This refracted ray is bent away from the interface to the normal, as shown in Figure 3.1a. The refraction can be expressed by:

$$\frac{\sin \theta_1}{\sin \theta_2} = \frac{n_2}{n_1} \quad (3.2)$$

Equation (3.2) represents the Snell's law of refraction.

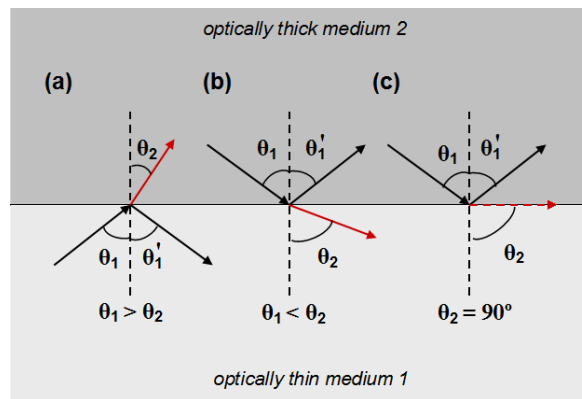


Figure 3.1 Schematic representation of the Snell's law of refraction and total internal reflection.

The same phenomenon is observed when a light ray passes from the medium 2 of n_2 to the medium 1 of n_1 , but here the refracted ray is bent away from the normal to the interface, as shown in Figure 3.1b. But at a particular angle of incidence called as critical angle ($\theta_1 = \theta_C$)-refracted light beam passes perpendicular to the normal ($\theta_2 = 90^\circ$), i.e. grazes along the interface, as shown in Figure 3.1c. When the angle of incidence increases beyond θ_C , all incident lights are totally reflected back, nothing is transmitted. This phenomenon is called as

total internal reflection, which is the fundamental optical effect for light propagation through optical fibers. The critical incidence angle (θ_c) is given by:

$$\theta_c = \arcsin\left(\frac{n_2}{n_1}\right) \quad (3.3)$$

3.1.2 Numerical aperture

Numerical aperture NA determines the light gathering power of an optical fiber. A light ray (with an incidence angle θ_1) to be guided through the fiber is given by:

$$n_a \cdot \sin \theta_1 \leq \sin \theta_{max} = NA = \sqrt{n_{core}^2 - n_{clad}^2} \quad (3.4)$$

where n_{core} and n_{clad} are the refractive indices of fiber core and cladding, respectively, n_a is the refractive index of air and θ_{max} is the maximum incidence acceptance angle. It can be schematically represented in Figure 3.2.

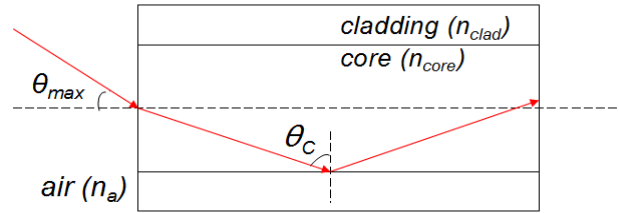


Figure 3.2 Maximum acceptance angle of light in an optical fiber.

The quantity $\sin\theta_{max}$ is commonly known as numerical aperture of an optical fiber. Therefore, generally, NA is related to the difference of refractive indices of fiber core and cladding. A large NA generates more modes and eases the problems of installation. Usually, NA of POF is larger as compared to glass optical fiber [36].

3.1.3 Classification of POF

Classification based on refractive index distribution

In an optical fiber, light rays propagate from one place to another to transmit the data information through fiber core. The core profile or refractive index distribution determines the light propagation in an optical fiber. Based on this relation, an optical fiber is either step-index (SI) or graded-index (GI) fiber, which can be schematically illustrated in Figure 3.3.

In SI optical fibers, the refractive index of fiber core is constant and its distribution $n(r)$ is definitely independent on core radius r , as explained in Equation (3.5), which allows the light rays to propagate in straight lines, as shown in Figure 3.3A.

$$n(r) = \begin{cases} n_{core} & 0 < r < r_{core} & \text{core} \\ n_{clad} & r > r_{core} & \text{cladding} \end{cases} \quad (3.5)$$

where r_{core} is the constant core radius.

In GI optical fibers, the refractive index of fiber core is changeable and its distribution is dependent on core radius, as expressed in Equation 3.6, which shows parabolic profiles in propagating paths, as described in Figure 3.3B.

$$n^2(r) = \begin{cases} n_{core}^2 \left[1 - \frac{n_{core}^2 - n_{clad}^2}{n_{core}^2} \left(\frac{r}{r_{core}} \right)^2 \right] & 0 < r < r_{core} \quad \text{core} \\ n_{core}^2 \left[1 - \frac{n_{core}^2 - n_{clad}^2}{n_{core}^2} \right] = n_{clad}^2 & r > r_{core} \quad \text{cladding} \end{cases} \quad (3.6)$$

Based on the theory of total internal reflection, light rays received in an optical fiber could propagate forward in different paths in fiber core. In both SI and GI optical fibers, each light ray experiences many bounces from the interface between core and cladding to fiber core. After each reflection, the light ray transmits with a certain shape corresponding to the refractive index distribution of core. In another word, a guided mode of an optical fiber refers to lots of light rays propagating in particular shapes.

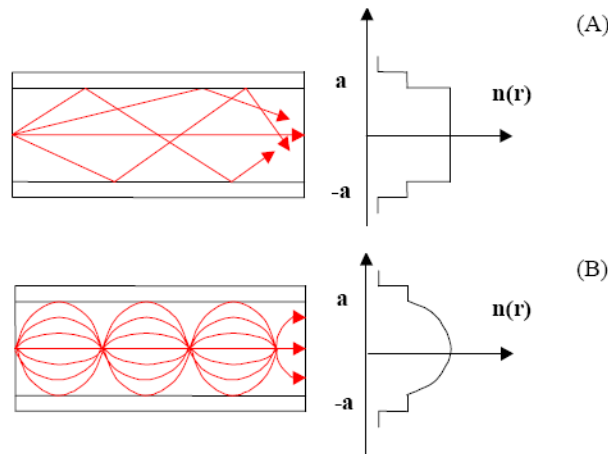


Figure 3.3 Schematic representation of refractive index distribution of an optical fiber: (A) step-index; (B) graded-index [37].

In SI optical fibers, the places of reflection are different, the light rays travel in different directions, that is to say, the time difference exists in different propagating paths, leading to the mode dispersion.

In GI optical fiber, both reflection and refraction occur due to the parabolic refractive index distribution of core which decreases along the fiber axis to the interface between fiber core and cladding, therefore, light rays travel a smaller distance at a faster velocity in the area near to fiber axis. In an ideal situation, all the light rays could reach the fiber axis at the same time and generate only one mode accordingly. This phenomenon alleviates the optical loss caused by modal dispersion [36].

Classification based on data transmission

The light rays in an optical fiber could generate at least one mode that is the fundamental mode, based on this, optical fibers are categorized into single-mode and multimode fibers.

A single-mode optical fiber corresponds to a comparatively small core diameter that is around 8-10 μm . It allows only the fundamental mode in ray tracing, leading to the low optical loss and high bandwidth or information capacity.

A multimode optical fiber requires a relatively large core diameter that allows the analysis with a geometric ray-tracing model. This type of optical fiber describes different light intensity distributions. According to the core size and numerical aperture, multimode optical fibers could support more than 100 modes. Multimode optical fibers are easy for light launch and connection, and also available for usage of cheap light sources (e.g. LEDs) other than laser diodes which are usually used for single mode optical fibers. However, multimode optical fibers have a significant disadvantage that is the high modal dispersion, the bandwidth or information capacity decreases due to its dependence on mode, resulting in the reduced information transportation directly. The bandwidth of multimode optical fibers could be optimized by adjusting core size, numerical aperture and fiber refractive index [36].

Classification based on illuminating effect

Light rays could emit out from different places of POF and give various luminous patterns. Based on this concept, POF could be majorly classified into two kinds: end emitting POF and side emitting POF [38]. Figure 3.4 illustrates the basic difference of light transmission in both fibers.

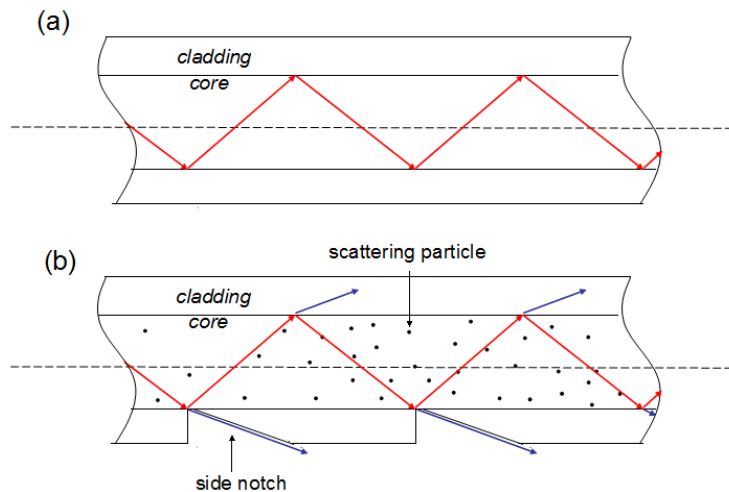


Figure 3.4 Light transmission in POFs: (a) end emitting POF; (b) side emitting POF.

End emitting/illuminating/glow POF is one kind of POFs, which only allows light rays to emit from the fiber end. The light rays propagate forward in POF according to the total internal

reflection. This fiber is generally designed for data communication and its optical loss is relatively low.

Side emitting/illuminating/glow POF can transmit light rays from both fiber end and fiber surface. This phenomenon is called side illumination or lateral illumination. This special illuminating characterization of side emitting POFs gives rise to a lot of potential in textile fabrics. Side emitting POF is usually manufactured by either reducing the difference between refractive indices of fiber core and cladding or increasing the asymmetry of core/cladding geometry. Besides, the side illuminating effect could be also achieved by surface modifications [39-42].

3.1.4 Structure and materials of POF

POF structure

POF is made of two main parts, as pictured in Figure 3.5, the inner part represents fiber core and the outer parts is normally composed of fiber cladding and jacket. In some cases, the outer part is only cladding in naked POFs. Generally speaking, POF core diameter is in the range of 0.2 ~ 1.0 mm, POF cladding is 0.02 ~ 0.05 mm thicker than POF core [36], and POF jacket thickness varies according to various manufacturers and applications.

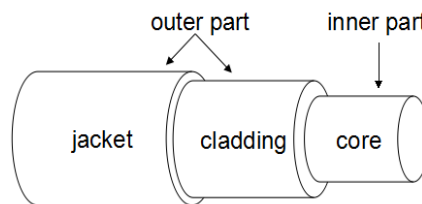


Figure 3.5 Description of POF structure.

POF core materials

As an optical waveguide, the transparency of fiber materials is vital. In order to produce a fiber, the fiber or film forming ability of these materials is also important. The thermoplastics, which possess high transparency and are easy to form fibers or films, are proven as the best core materials for POF, such as poly(methyl methacrylate) (PMMA), polystyrene (PS) and polycarbonate (PC) which are three well-known materials for POF core [43-47], the corresponding basic information are shown in Figure 3.6 and Table 3.1.

In above three polymers, PMMA and PS are used as POF core materials for normal condition end use, PC has higher glass transition temperature so that it is developed for high temperature applications. Compared with POFs based on these core materials, PMMA core POF has smaller optical loss than the other two kinds [43-47].

In addition, deuterated polymers and fluoropolymers could be also applied as POF core materials [43-45]. Both polymers are not suitable enough due to their drawbacks. Deuterated

polymers show very low refractive index that leads to difficulties to find suitable cladding materials, large water absorption, bulk polymerization and high production cost even though they reduce the optical loss. Fluoropolymers have high optical loss due to high crystalline and difficult fiber drawing caused by high melt viscosity. At present, pure PMMA is most common as POF core material.

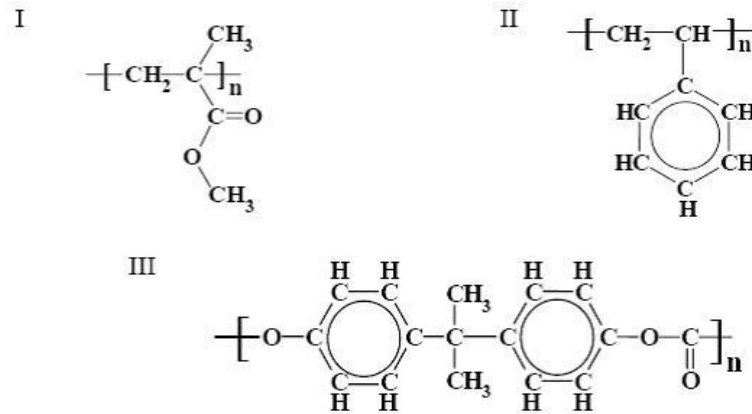


Figure 3.6 Molecular structure: (I) PMMA; (II) PS and (III) PC [36].

Table 3.1 Basic characteristics of polymers for POF core materials [48-50].

	PMMA	PS	PC
Refractive index	1.49	1.6	1.584 ~ 1.586
Density [g/cm ³]	1.17 ~ 1.20	0.96 ~ 1.04	1.20 ~ 1.22
Melting temperature (T_m) [°C]	160	240	155
Glass transition temperature (T_g) [°C]	105	100	147
Upper working temperature [°C]	60 ~ 80	60 ~ 80	115 ~ 130
Water absorption (ASTM)	0.3 ~ 0.4	0.03 ~ 0.1	0.16 ~ 0.35
Transparency	high	high	high
Fiber forming ability	good	good	good

POF cladding materials

Apart from the good film forming ability, there is another main requirement for POF cladding materials, the refractive index of cladding should be close and a little smaller than the refractive index of core. Additionally, POF cladding should provide good mechanical/chemical/thermal resistances for POF core.

Fluorinated polymers are not developed as POF core materials, however, they are suitable as POF cladding materials. Fluorinated polymers are with multiple strong carbon-fluorine bonds, leading to good chemical resistance.

There are two widely used fluoropolymers in POF cladding: copolymers of fluoroolefins and poly(fluoroalkyl acrylates) (PFAs) [51]. PFAs are preferred due to a lot of advantages such as easy photo-polymerization, high transparency, good adhesion characteristics and so on. In present market, a great deal of PFAs are mainly utilized in cladding materials in optical fibers.

POF jacket materials

The use of jacket in POFs is mainly aimed to protect POFs and determine the ultimate properties like mechanical/chemical/thermal resistances which decide the durability or lifespan of POFs in various end uses. The possible POF jacket materials are polyvinylchloride (PVC), polyethylene (PE), polypropylene (PP), polyamide 6 (PA 6), copolymer of ethylene-vinylacetate (EVA), perfluoroethylenepropylene (PFEP), polyurethane (PU), polytetrafluoroethylene (PTFE) [43].

3.1.5 Attenuation mechanism of POF

The primary importance has been given to understand and reduce their optical transmission loss since the development of POF. Table 3.2 shows the sources of loss factors which represent the optical loss mechanism of POF [36].

Table 3.2 Optical loss factors of POF [36].

Type	Mechanism	Origin
Intrinsic	Absorption	<ul style="list-style-type: none"> • Higher harmonics of C-H absorption • Electronic transitions
	Rayleigh Scattering	<ul style="list-style-type: none"> • Density or refractive index fluctuations • Orientation fluctuations • Composition fluctuations
Extrinsic	Absorption	<ul style="list-style-type: none"> • Transition metals • Organic contaminants • Absorbed water
	Scattering	<ul style="list-style-type: none"> • Dust, micro voids and fractures • Fluctuations in core diameter • Orientation birefringence • Core-cladding boundary • Micro and macro voids

The intrinsic loss factor is mainly caused by basic fiber-material properties. Materials properties such as absorption and scattering (Rayleigh) are the main impulses of the intrinsic loss factor. The contribution of intrinsic loss factor to the total attenuation is higher than that of the extrinsic loss factor and therefore it can be a major source of the optical loss in POFs. The extrinsic loss factor is caused chiefly by external contaminations in the fiber core and physical imperfections in the fiber.

3.1.6 Manufacturing techniques of POF

A lot of manufacturing techniques of POF have been developed since the introduction of POF. Based on the classification of POF, the manufacturing techniques could be distinguished in terms of the refractive-index profile, SI and GI. Both of them are separated according to the continuity of process flow.

Manufacturing techniques of SI POF

The manufacturing techniques of SI POF are described in Figure 3.7. The discontinuous techniques consist of heat-drawing technique and batch extrusion technique [52]. There are generally two steps in heat-drawing technique: preform preparation and drawing process. The preform could be produced by either wet or dry process. The polymerization of core and cladding are separated in dry process or in the same process in wet process. After the preparation of preform made of both core and cladding, the preform held in a holding fixture is heated above the glass transition temperature from the bottom side in an oven by a furnace, in order to decrease its viscosity for drawing process. In some cases, the preform consists of core only, a downstream coating or extrusion process for cladding preparation is necessary. This technique benefits to the technical simplicity, technical flexibility and good quality of final products [46, 53-58].

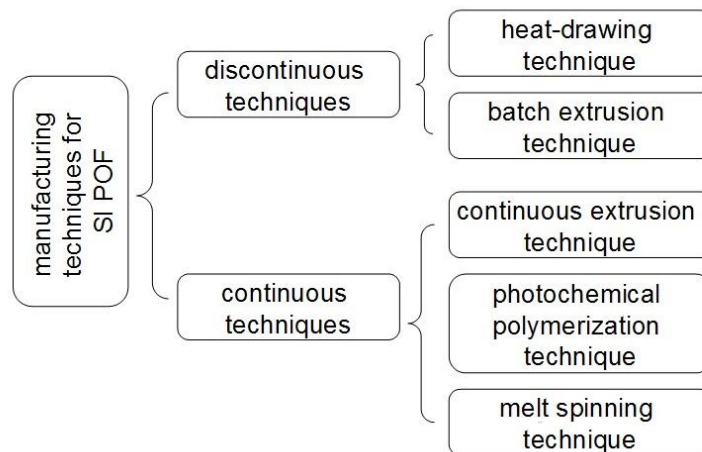


Figure 3.7 Classification of manufacturing techniques of SI POF.

Similarly, there are also two steps in batch extrusion technique. The polymerization of fiber core starts first to form the core polymer melt that is conveyed to a spinning nozzle, then the cladding polymer is melt and conveyed into another spinning nozzle, finally the batch extrusion process completes. This techniques is with low technical difficulty and small thermal degradation of polymers. On the other hand, the productivity of this technique is comparaticely low [57-59].

The continuous techniques include continuous extrusion, photochemical polymerization and melt spinning process. In the continuous extrusion technique, the polymerization of core materials initiates in a reactor and then continues through the extruder. The cladding material could be either applied in the same spinning nozzle for core or in a downstream process. This technique gives rise to the good productivity and purity of POF. However, the whole investment of this technique is costly, in the mean time, the polymerization and extrusion processes are difficult to control [46, 53-57].

In the technique of photochemical polymerization, both core resin and cladding resin are pumped into a mixing chamber where the cladding resin coats onto the core resin. The mixed resins go through a spinning nozzle to form a structured fiber. The fiber is then irradiated with an ultraviolet (UV) lamp to initiate the crosslinking process [53, 56].

The melt spinning technique is similar but less complex to the continuous extrusion technique because the raw materials are polymer granulates rather than polymer monomers. The core polymer granulates are molten in an extruder and then pumped into a spinning nozzle, the cladding material could be applied by either a co-extrusion process or a downstream process, the same as the application of cladding material in continuous extrusion technique. This technique gives rise to a high productivity, but also results in more expenses on melt spinning equipments and high attenuation due to the impurities in polymer granulates [53, 58, 59].

Manufacturing techniques of GI POF

Compared with SI POF, GI POF has different refractive-index profile that allows high data rate or bandwidth, and also requires more complex manufacturing processes. The general manufacturing techniques of GI POF are shown in Figure 3.8.

In discontinuous techniques, the emphasis is to achieve a refractive-index profile in a preform, the distribution of refractive-index gradient is fixed by polymerization. In interfacial-gel polymerization technique, different monomers are filled in a PMMA tube, a gel layer grows on the side of the rotated PMMA tube. The distribution of a refractive index gradient is made up due to the different diffusion rates of monomers with various molecular masses [60, 61].

The chemical vapor deposition (CVD) technique means that a preform is produced by CVD method. The raw materials are vaporized and deposited on the inner surface of a cylindrical tube to establish a refractive-index gradient [62].

The centrifugation technique indicates that a preform is produced by using a centrifuge. The refractive-index profile could be formed by the monomer with different densities or by a monomer mixture with a continuously or stepwise changing composition [53, 56].

The diffusion technique refers to two main materials: a rod composed with a monomer with high refractive index, a cylindrical reactor filled with a monomer with low refractive index. The rod is laid in the center of the rotated cylindrical reactor. The diffusion of the rod material leads to a refractive-index gradient [53].

The photochemical polymerization technique involves in a step of UV radiation. A mixture of monomers are filled into a glass cylinder which is irradiated with UV lamp to launch the polymerization [53, 56].

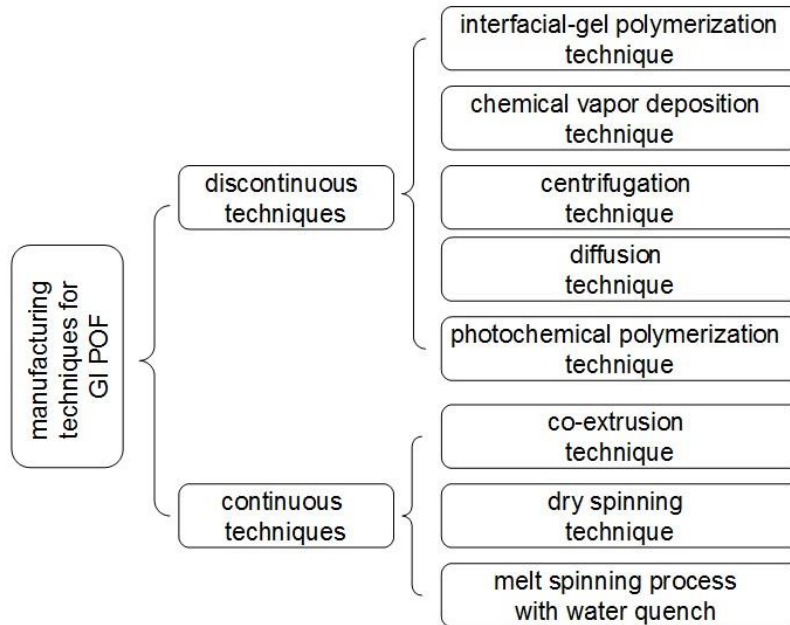


Figure 3.8 Classification of manufacturing techniques of GI POF.

In continuous techniques, the major point is to produce a refractive-index profile in a modified spinning process. The co-extrusion technique is related to three possibilities. One possibility is to create an index profile by using a special die block. Simply speaking, different raw materials in respective channels are pumped into the first mixing chamber to set up an axial distribution of materials based on the different channel gap or length. The mixture is fed to the second chamber to change all materials into a radial distribution [24]. Another is the co-extrusion combined with diffusion and UV irradiation processes. The co-extrusion process is similar as the photochemical polymerization technique, but the raw materials are polymeric solutions rather than polymer resins or monomers. A mixed solution with a step-index profile is created in the spinning extruder and flows through a spinning nozzle. Then the fiber is heated in a hot diffusion zone to form a radial concentration gradient. The distribution of a refractive-index profile is fixed by photochemical polymerization with a UV lamp [63]. The last possibility is established by injecting a diffusible material into a polymer melt through a centered capillary tube at the inside of a die block [37].

The dry spinning technique requires a thermoplastic polymer with low refractive index and at least one monomer with high refractive index to form a mixture. After the melt and homogenization, the mixture is fed to the spinning nozzle. Then the monomer is volatilized

from the surface of fiber and a concentration gradient creates. The distribution of a refractive-index profile is fixed by polymerization induced by UV irradiation [64].

In the technology of melt spinning process with water quench, the polymer granulates are molten in an extruder. The molten polymer is pumped into a spinning pump and fed into a spinning nozzle to form a fiber. The fiber passes through the air between the spinning nozzle and water quench, and then is cooled fast in a water quench. The cooling rate decreases from the fiber surface to center. A radial temperature gradient creates, leading to a radial density gradient of the cooled polymer. Therefore, a refractive-index profile is obtained based on the relation between density and refractive index [52, 65].

In summary, compared with continuous techniques, discontinuous techniques for both SI POF and GI POF obtain fibers with high purity, low attenuation, high accuracy and more adjustment in refractive-index profiles, as well as low productivity [66]. The selection of manufacturing techniques is totally dependent on the demands of optical fibers and the costs of selected manufacturing techniques.

3.2 Side illumination of POF

3.2.1 Review from literatures

The side illumination of POF is preferred in the luminous applications. Compared with end emitting optical fiber, side emitting optical fiber shows stronger lighting effect since light can escape from fiber surface due to either the surface defects or the large difference between core refractive index and cladding refractive index. Side emitting POFs with small fiber diameter are difficult to manufacture and therefore a lot of efforts have been devoted to the development of side illumination of optical fibers by surface modifications [39-42], including both physical methods (like side notches, asymmetry of core/cladding geometry, micro bends of fiber and surface abrasion) and chemical methods (like solvent etching, addition of radiation scattering particles into fiber core/cladding).

Im *et al.* used three methods to improve the surface modification [67]. The first method called chemical etching was processed with ethyl acetate (EA), the second was related to mechanical abrasion, which was accomplished by sandpapers. The last one was conducted with the combination of the first two methods, the mechanical abrasion went first and the chemical etching continued after that. The SEM pictures of POFs before and after surface modifications are shown in Figure 3.9. The corresponding images of side illuminating effect are given in Figure 3.10.

The results from both figures indicate that both chemical and mechanical methods could be used to improve the side illumination of POF, especial the combination shows the strongest side illumination intensity. While, these methods lead to the decrease in tensile properties of POF dramatically, which could result in the POF fracture during the manufacturing process of POF fabrics. In order to eliminate this influence, the chemical coating method was applied to

POF surface. However, the notched POF presents even worse tensile properties after coating treatment.

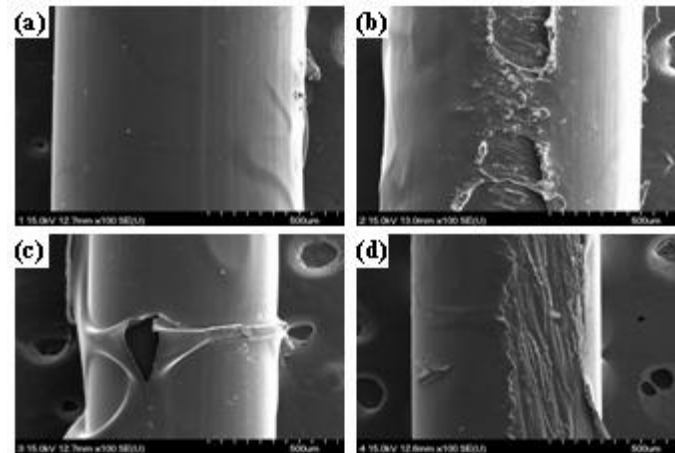


Figure 3.9 POF images: (a) bare; (b) physically rubbed with sandpaper; (c) etched with EA; (d) physically scratched and then solvent-etched [67].

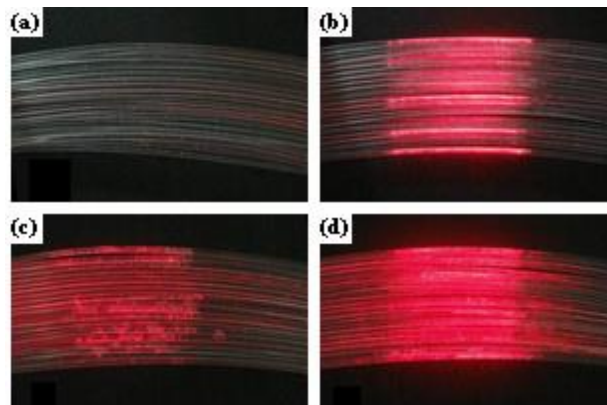


Figure 3.10 POF arrays with side illuminating effect: (a) bare; (b) physically rubbed with sandpaper; (c) etched with EA; (d) physically scratched and then solvent-etched [67].

Shen *et al.* focused on the improvement of side illumination of POF by laser treatment [42]. The laser technique was employed to create the notches in the designed places on POF surface, in order to enhance the side illuminating effect of bent POF, as shown in Figure 3.11. The results indicate that both notches and bends could improve the side illumination of POF, but the bending radius has no effect on the side illumination of POF at the points with notches. Meanwhile, the authors also pointed that POF fabric display could be achieved by laser treatment.

In a word, the surface modifications with both mechanical and chemical methods can improve the side illumination of POF to some extent. However, the mechanical properties of POF might be also influenced accordingly.

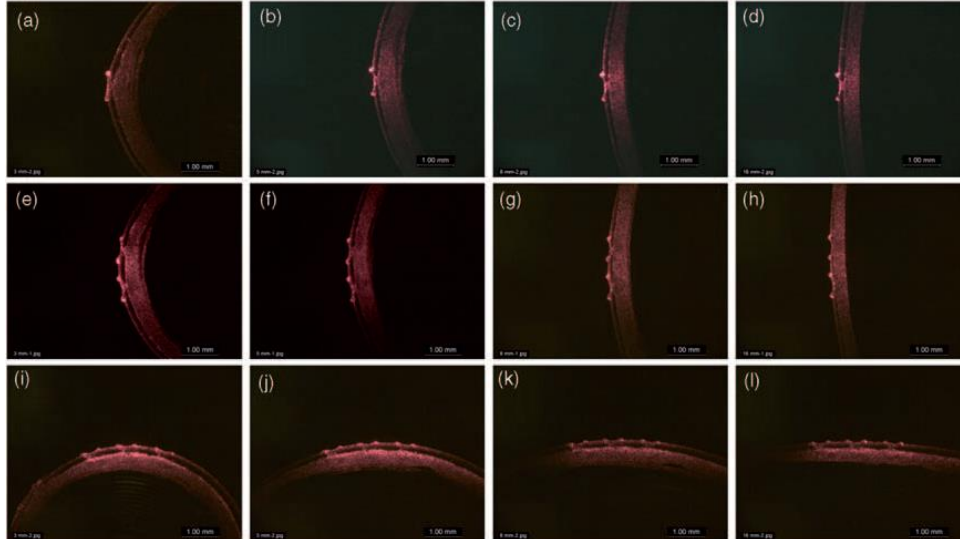


Figure 3.11 Light illuminating effect of POFs with different numbers of notches at various bending radii of 3, 5, 8 and 16 mm, respectively: (a)-(d) one notch; (e)-(h) two notches; (i)-(l) three notches [42].

3.2.2 My state of the art

The side illuminating effect of POF was enhanced by the combination of laser treatment and titanium dioxide fine particles. The parameters of side illumination intensity and attenuation coefficient were discussed in details. The corresponding methods and results are presented in the publication shown in Annex I.

3.3 Nanoindentation properties of polymers

3.3.1 Introduction of indentation

With the increasing requirement of heterogeneous materials (such as functional graded materials, nanomaterials, fiber strengthened composites, etc.) in electronic, mechanical, aerospace, biomedical and environmental engineering fields, a critical evaluation method with high load and displacement resolutions is urgent to be developed, in order to predict the surface properties, the failure behaviours, the reliability as well as the design improvements of such materials. In the past decades, great contributions have been made in the development of techniques of probing the mechanical properties at the very first surface molecular layers or on the submicron scale [68-70]. With the development of instrument engineering, the continuous force and displacement could be conducted with an indentation [71-74]. The data of both load and displacement could be utilized to calculate the mechanical properties such as hardness,

modulus and stiffness of materials. With the improvement of displacement resolution of instrument, the small indentation even in submicron scale is able to be observed. This kind of instrument with good displacement resolution is considered as a microprobe for investigation of mechanical properties [69, 75, 76].

In indentation techniques, the most frequently measured parameters for mechanical properties are elastic modulus and hardness, which could be calculated based on the analysis of the elastic response relating to the maximum contact area with the indenter shape [77]. The critical problem is derived from the elastic contact that was initially taken into account in the 1880s. In 1882, Hertz considered the elastic contact differences from two spherical surfaces with various elastic constants and radii [78], providing the experimental and theoretical information for contact mechanics. In 1885, Boussinesq firstly brought about a method for the situation of loading a rigid and axisymmetric indenter onto an elastic material [79], providing the basis for indenters with various geometries like cones and cylinders [80, 81]. In 1945 and 1965, Sneddon raised the relations of load, displacement and contact area for any indenter geometry [82, 83], which can be expressed as:

$$P = ah^m \tag{3.7}$$

where P is the applied indentation load, h is the elastic displacement of indenter, both a and m are constants from the power law fitting curve. The value of m for different indenter geometries is various, as given in Table 3.3.

Table 3.3 Values of exponent m in different indenter geometries [77].

Parameter	Value	Indentation shape
	1	Flat cylinder
m	1.5	Spheres in the limit of small displacement
	2	Cones

It is complex to model the indentation contact including both elasticity and plasticity. In 1948, Tabor originally did the experiments in terms of the investigation of mechanical properties by the method of indentation with hardened spherical indenters [84]. In 1961, Stillwell and Tabor conducted the similar measurements with conical indenters [85]. All these contributions considered the indentation after the indenter is unloaded and the elastic deformation reverses. Based on the measurements for metals with different indenters, Tabor generalized that the total amount of reversed deformation is precisely associated to the elastic modulus and the size of indenters.

From the early 1970s, a lot of contributions have been made to examine the elastic modulus by the load and displacement sensing displacement testing [86-89]. The load and displacement

data are drawn in Figure 3.12. The stiffness S is the slope of the upper part of the unloading curve, which is expressed in Equation (3.8). The reduced modulus is obtained by assuming that the contact area is the same as the optically measured area of the hardness indentation after the indenter is unloaded, as shown in Equation (3.9). Therefore, the modulus is determined.

$$s = \frac{dP}{dh} = \frac{2}{\sqrt{\pi}} E_r \sqrt{A} \quad (3.8)$$

$$\frac{1}{E_r} = \frac{1 - \nu^2}{E} + \frac{1 - \nu_i^2}{E_i} \quad (3.9)$$

where A is the project area of elastic contact, E_r is the reduced modulus, E and ν are the Young's modulus and Poisson's ratio of the sample, and E_i and ν_i are the Young's modulus and Poisson's ratio of the indenter. Equation (3.8) was then proved to be useful not only for the conical indenters, but also for spherical, cylindrical indenters and others as well [87].

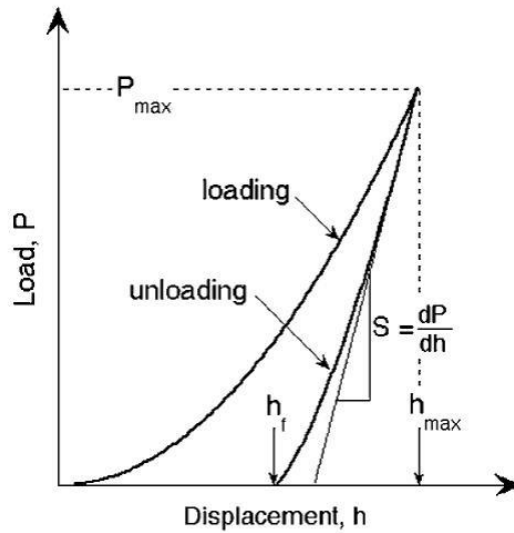


Figure 3.12 Schematic illustration of load-displacement data by instrumented micro-hardness testing [77, 90].

From the early 1980s, the load and displacement sensing indentation methods were considered as the very useful techniques to investigate the mechanical properties of thin films and surface layers by producing the submicron indentations [71-74]. In order to understand the contact area clearly, rather than by assuming that the optically measurement of hardness impression equals the contact area, researchers tried to find the relationship between the contact area and indentation depth. It is estimated that the area of the cross section of indenter is a function of the distance from indenter's tip, which is also called the shape function [68, 69]. In 1986, Doerner and Nix finally raised a method based on the assumption that the initial part of the unloading curve is linear. The depth at the zero load of this linear curve was employed to

calculate the contact area according to the shape function. Then the modulus could be also determined.

However, the initial part of unloading curve for many materials is not linear in practical [77]. In 1992, based on a lot of measurements for a variety of materials, Oliver and Pharr found that it is efficient to apply Equation (3.7) to define the unloading data [77]. In the meanwhile, by utilization of a special dynamic technique, they observed that the stiffness value varies continuously and immediately once the indenter starts unloading. Thereby, they proposed a new method (called Oliver and Pharr method) with the basis of experimental and theoretical work, which has been widely adopted for a long period of time. Until 2004, Olive and Pharr provided the new understanding of mechanics of elastic-plastic contact, which has been used since then [90].

3.3.2 Basic principles of Oliver and Pharr method

The Oliver and Pharr method was originally developed to investigate the mechanical properties of materials from the load and displacement data in one complete cycle of loading and unloading with sharp, geometrically self-similar indenters like the Berkovich triangular pyramid, it is found that this method could be also used for indenters with axisymmetric geometries including spheres [90].

In the load-displacement curve of one loading-unloading cycle in Figure 3.12, the deformation during loading period includes both elastic and plastic responses. While in the unloading period, only elastic deformation recovers, that's why the hardness impression exists finally. On the other hand, the reversed plastic deformation could be negligible according to the finite elements simulations [91]. Based on these conceptions, the Oliver and Pharr method is applied for the materials which have no recovery of plastic deformation during unloading period [90].

Table 3.4 Values of fitting parameters observed in nanoindentation experiments with a Berkovich indenter [77].

Material	a [mN/nm ^m]	m	Correlation coefficient
Aluminium	0.2650	1.38	0.9999
Soda-lime glass	0.0279	1.37	0.9999
Sapphire	0.0435	1.47	0.9999
Fused silica	0.0500	1.25	0.9999
Tungsten	0.1410	1.51	0.9999
Silica	0.0215	1.43	0.9999

As discussed before, in Doerner and Nix method, the upper part of the unloading curve is assumed to be linear when the indenter is unloaded. In Oliver and Pharr method, the unloading curves are observed to be nonlinear and could be defined by the power law equation:

$$P = a(h - h_f)^m \quad (3.10)$$

where h_f is the final displacement in indentation testing, a and m are the constants from power law fitting curve [77]. The corresponding values of these two constants are listed in Table 3.4, according to the experiments of nanoindentation testing with a Berkovich indenter, the power law exponent m varies in the range of 1.2 ~ 1.6, with an exception when m equals 1 for flat punch. Another exception occurs when m equals 2 for Berkovich indenter of which the axisymmetric equivalent is a cone. Moreover, the indenter behaves like a paraboloid when m equals 1.5 [82].

Figure 3.13 gives one example of a cross section of an indentation in terms of the surface profile of a material. The total or maximum displacement h_{max} is expressed as:

$$h_{max} = h_c + h_s \quad (3.11)$$

$$h_s = \epsilon \frac{P_{max}}{S} \quad (3.12)$$

where h_c is the contact displacement that is the vertical depth along which the contact is made, h_s is the displacement of the surface at the perimeter of the contact. ϵ is a constant that is dependent on the geometry shape of the indenter. Some common values of ϵ are represented in Table 3.5.

Table 3.5 Punch parameter in indentation data analysis [77].

Parameter	Value	Indentation shape
ϵ	1	Flat cylinder
	0.75	Paraboloid
	0.72	Cones

Based on the Equations (3.11) and (3.12), h_s could be expressed as:

$$h_s = h_{max} - \epsilon \frac{P_{max}}{S} \quad (3.13)$$

where P_{max} is the maximum load.

A method was proposed to determine the area function, which is based on the assumption that the elastic modulus is independent on the indentation depth. This method is followed by the modelling of the load frame and the sample [77],

$$C = C_s + C_f \quad (3.14)$$

where C is the total measured compliance, C_s is the sample compliance, C_f is the load frame compliance. Since there is a reciprocal relationship between the sample compliance and the contact stiffness, the Equation (3.14) could be transferred into:

$$C = \frac{\sqrt{\pi}}{2E_r} \frac{1}{\sqrt{A}} + C_f \quad (3.15)$$

It is observed that there is a linear relationship between the total compliance and the value of $A^{-1/2}$ if the reduced modulus is constant. The intercept of the linear curve is exactly the value of the load frame compliance.

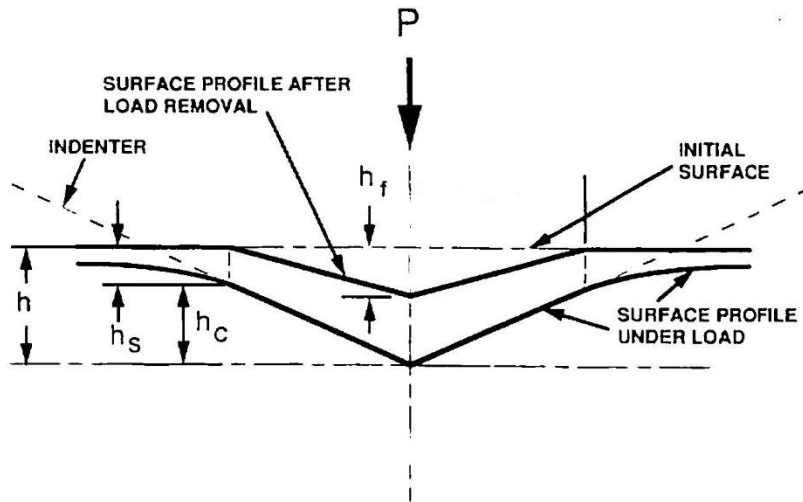


Figure 3.13 Schematic illustration of a cross section of an indentation [77].

To figure out the load frame compliance and the area function, aluminium is chosen as the sample due to its low hardness and large indentations made in indentation testing. Through the experiments with aluminium, it is found that the area function for a perfect Berkovich indenter can be defined as:

$$A = A(h_c) = 24.5h_c^2 \quad (3.16)$$

The initial assumption at the area function is made and expressed as:

$$A = A(h_c) = 24.5h_c^2 + C_1h_c^1 + C_2h_c^{1/2} + C_3h_c^{1/4} + \dots + C_8h_c^{1/128} \quad (3.17)$$

The area function, that is the indenter shape function, should be carefully calibrated by independent experiments and the deviations from non-ideal geometric shapes of indenters should be also considered seriously.

Once the contact area is determined, the hardness H is estimated as follows:

$$H = \frac{P_{max}}{A} \quad (3.18)$$

3.3.3 Creep from nose phenomenon

The values of hardness, Young's modulus and stiffness of polymers can be obtained from the load-displacement behaviour carried out by applying the increasing load and decreasing load to the surface with a shaped indenter. Measurements on mechanical properties of polymer surface can provide improved understanding of molecular structure of the material itself, manufacturing and polymerization processes. When nanoindenter contacts the polymeric surface and penetrates into the polymer, additional difficulties for the indenter to go inside the polymer are caused by the complicated viscoelastic-plastic response that is typical characterization of such kind of material. Polymer has highly strain-dependent and strain rate-dependent properties and shows substantially different behaviours when the indentations are proceeded under different contact conditions. The viscoelastic-plastic response of such material, therefore, can provide the values of hardness and elastic modulus, which are usually a function of the imposed contact conditions, such as the geometry of the contact and the penetration depth (i.e. the strain), the loading rate (or strain rate) [92, 93] and the ambient temperature [94, 95].

There is a key limitation of normal indentation technique applied in polymers, which is the nose phenomenon with a round shape of data at the load-unloading peak, as shown in Figure 3.14 [94]. If the loading rate control has the higher priority than the displacement rate control, at the initial stage of unloading period, the polymer that is in contact with the indenter might response the creep effect, which means, when the unloading begins, the indenter intends to go further slightly other than go back immediately.

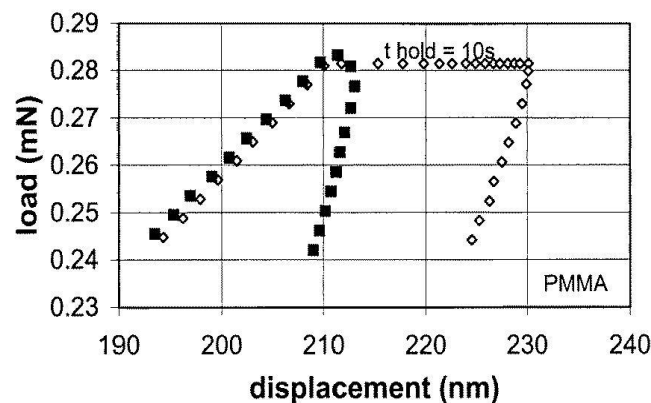


Figure 3.14 Nose problem and a holding segment at the peak load of load-displacement data of PMMA [94].

This nose phenomenon, which may be found in view of the highly time-dependent deformation nature of polymers, may be caused by the complex viscoelastic-plastic response of such

materials and influence the evaluation of contact displacement of the surface markedly, resulting in effects on the evaluation of indentation hardness and modulus.

Briscoe and Sebastian studied the elastoplastic response of PMMA by indentation method with rigid conical and spherical indenters [96]. The associated intrinsic error in experimental data was described and partially solved with an estimation of the tip defect.

Briscoe analyzed the influences of the nose phenomenon of four polymeric systems [94]. The results reflect that there is no elastic or viscoelastic recovery observed at the incipient unloading, the power law assumption is thus infeasible. A method was thus proposed to eliminate the nose effect. An enough period of time is considered at the peak load, in order to let the materials reach a mechanical equilibrium before the unloading starts, as shown in Figure 3.14.

3.3.4 Strain rate

The strain rate $\dot{\epsilon}$ is normally defined as the imposed rate of indentation deformation, which is related to the displacement rate or the loading rate of indenter. Generally speaking, the direction of deformation depth is perpendicular to the surface of sample, that is to say, the strain rate changes perpendicularly to the sample surface. The equation of strain rate is expressed as [94]:

$$\dot{\epsilon} = k_2 \left(\frac{\dot{h}}{h} \right) \quad (3.19)$$

where k_2 is a material constant, usually equals 1 [94], h is the indentation displacement, \dot{h} is the nominal indentation displacement rate.

Ma *et al.* investigated the loading rate sensitivity of nanoindentation creep of films and the strain rate was discussed with Equation (3.19) [97]. The nominal displacement rate \dot{h} is the first derivation of indentation displacement h versus time t , as shown in Equation (3.20). The indentation displacement is obtained by the empirical fitting formula in Equation (3.21) [92, 94, 97],

$$\dot{h} = \frac{dh}{dt} \quad (3.20)$$

$$h = a \cdot (t - t_i)^m + kt + h_i \quad (3.21)$$

where a , m , k and h_i are fitting constants, t_i is the time when the creep displacement occurs initially in real experiments.

They also analyzed the value of stress exponent n which is defined as the slope of the curve of $\log(\text{strain rate})$ versus $\log(\text{stress})$:

$$n = \frac{\partial(\log(\dot{\epsilon}))}{\partial(\log(\sigma))} \quad (3.22)$$

$$\sigma \sim P/h^2 \quad (3.23)$$

where σ is the stress acting nominally in a direction perpendicular to the sample surface in depth-sensing indentation technique.

3.3.5 Applications in interphase properties

With the development of instrument technique, the load-displacement indentation method could be applied in nanometer-scale displacement and smaller load range, which refers to the nanoindentation technique. At present, nanoindentation is widely used to measure the mechanical properties of materials than other testing methods, e.g. dynamic mechanical analysis (DMA) and Instron. One popular application is the investigation of interphase properties of composites.

The interphase properties between matrix (metal, clay or polymers) and reinforcement (fibers or fabrics) could be estimated based on various depths and spacings of indentations in a line from matrix to reinforcement. The differences of hardness and modulus of points indicate the interphase width between matrix and reinforcement. The width of nanoindentation on specimens w is dependent on the nanoindentation depth h due to the geometry of Berkovich indenter [98],

$$w = 2h \frac{\tan 65.3^\circ}{\tan 30^\circ} = 7.532 h \quad (3.24)$$

$$s = 2w \quad (3.25)$$

where 65.3° and 30° are the constant parameters of Berkovich indenter. s is the safe spacing that the adjacent plastic deformation zones will not be overlapped by each other. For instant, when the nanoindentation depth is 80 nm, the calculated nanoindentation width is 0.603 μm , the spacing is 1.205 μm , which means 1.3 μm is enough to avoid the overlapping of the plastic deformation zones.

Hodzic *et al.* studied the polymer-glass interphase of polymer/glass composite materials by nanoindentation and reported that the plastic deformation zone resulted from the stress forms when the indenter goes inside the specimens, and it is reliable to measure the interphase width by nanoindentation technique, in the conjunction with the nano-scratch technique [99].

Lee *et al.* investigated the interphase properties between cellulose fiber and PP matrix in a cellulose fiber-reinforced PP composite by nanoindentation technique [100]. The gradient of hardness or modulus is supposed to associate with the width of the transition zone. However, the results from three-dimensional (3D) finite element analysis indicate that the interphase width of even a perfect interface without any property transition is almost the same as experimental value. They assumed that the nanoindentation could not measure the exact

interphase properties in the case that the distance between two adjacent indentations is at least 8 times larger than the indentation size.

Even though there are some limitations of nanoindentation technique in the measurement of the interphase properties of composites, nanoindentation testing is still an active method in this field.

3.4 Fatigue properties of single fiber

3.4.1 Introduction of fiber fatigue

The flexibility and versatility are also the factors of ultimate failure of textile materials. Failure, related to the durability of material, has been the subject for decades. During the usage of materials, more than 80 ~ 90% of all structural fracture is resulted from fatigue failure. Fatigue performance of fiber determines the effect of aging in order to predict the long term behaviour of fiber with respect to the mechanical properties in applied fields. Not only the fiber manufacturers investigate the fiber fatigue performance, there is also an interest to perform the fiber properties in textile field. During the manufacturing processes of fabrics, the strength loss of fiber occurs due to the repeated stresses, which increases the fiber fracture in manufacturing, packing or using period. For better in-depth understanding of the fracture and failure of textile based products, the fatigue property of fiber is particularly vital [101].

The term “fatigue” has a lot of definitions in practical uses. Fatigue, in material science, is defined as the weakening of a material due to the repeated application of stresses and strains, which leads to the progressive and localized structural damage like cracking and failure [67].

Generally, the fatigue failure of material is either caused by the small cyclic forces and occurs within the elastic or fully reversible region in stress versus strain curve. The first study of fatigue is related to the material-metal by Albert in the 1940s [102]. While, the concept of fiber fatigue is far complex than metal fatigue. The major difference between them is that the fiber tends to buckle under compression and the metal could not. That is why the fiber can display good flexibility and drapability. Due to the flexibility of fibers, on the other hand, the ultimate failure is usually resulted from mixed failure modes such as tensile, torsional and flexural failures. Furthermore, all polymer fibers represent the visco-elastic behaviour in tensile testing. The elastic region corresponds to the strain reversibility and the plastic region is related to the bond breakage. Both regions are not well defined in fibrous materials [101]. Thus, the confused and complex fiber fatigue could be considered as a very simple situation and might be misunderstood.

The general knowledge of fatigue behaviour of single fibers could be explained by tension fatigue. However, POF is very sensitive to bend. The diameter of textile fibers is usually in the range of 5 ~ 40 μm and the diameter of technical fibers varies from 10 μm to 25 μm [103]. The POF diameter in POF fabrics is generally more than 0.1 mm. Compared with the traditional textile fibers, POF in fabrics is less flexible. The fiber failure and optical loss of POF induced

by bends should be not neglected. Thereby, both tension fatigue and flex fatigue of POF are required to be investigated.

3.4.2 Theory of fatigue

There are two kinds of fatigue for fibers: static fatigue and dynamic fatigue. Static fatigue happens to a fiber under small constant external force. The fiber stretches gradually and breaks at the weakest point. Dynamic fatigue is a phenomenon of a fiber under cyclic loading and unloading processes. The deformation is accumulated gradually, leading to the fiber fracture finally. In the method of dynamic fatigue, there are two categories. If the external force is constant, the deformation accumulates, this is recognized as creep. If the deformation is constant, the external force decreases, this is relaxation.

In the investigation of dynamic fatigue with the constant applied load, the stress versus time curve can be described in Figure 3.15, which is considered as the classical fatigue testing based on the constant amplitude experiments. Stress cycle is characterized by stress range $\Delta\sigma$ that is equal to the difference between the maximum stress σ_{max} and the minimum stress σ_{min} . The stress ratio R , the mean stress level σ_m and the stress amplitude σ_s can be expressed as follows [104],

$$R = \frac{\sigma_{min}}{\sigma_{max}} \quad (3.26)$$

$$\sigma_m = \frac{(\sigma_{min} + \sigma_{max})}{2} \quad (3.27)$$

$$\sigma_s = \frac{(\sigma_{max} - \sigma_{min})}{2} \quad (3.28)$$

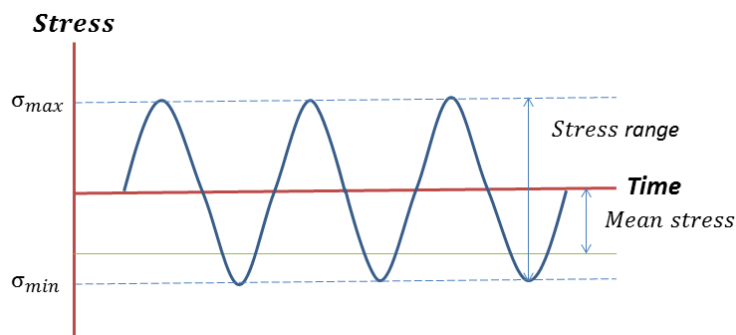


Figure 3.15 Cyclic variation of stress in fatigue test.

The stress life method is one of the classical fatigue methods, the basis of this method is $S-N$ curve (stress versus cycle curve, Wöhler curve or fatigue life curve) which is dependence of σ_s (for $\sigma_m = 0$) or $(\sigma_s + \sigma_m)$ on the number of fatigue cycles N to failure. The fatigue testing may be carried out with one kind load (such as compressing, bending, twisting, torque or tension) during one cycle, or different kinds of loads during one cycle. Three significant tensions, therefore, are distinguished [105]. One-side

tension means that σ_{max} has the same sign as σ_{min} . Two-side tension indicates that σ_{max} has different value as well as different sign from σ_{min} . While pulsing tension or zero suppressed tension is the case that σ_{max} has different sign but the same absolute value from σ_{min} , that is, the mean stress level $\sigma_m = 0$ and the stress ratio $R = -1$.

3.4.3 Fatigue testing methodology

Tension fatigue testing

There are a multitude of categories about fatigue testing of single fiber. Tension fatigue and flex fatigue are most discussed. Generally, the tension fatigue is conducted by the instruments of tensile testing. In the early tensile technique, Krause proposed a method of static tension fatigue of optical fiber [106], as shown in Figure 3.16. A single fiber is held at both ends with two capstans which are also used to give tension to fiber. The fiber is threaded through an environmental chamber and the testing condition is controlled by a constant temperature bath. It is worth noting that the ends of environmental chamber should be well sealed with rubber, in order to avoid the coating layer to strip or damage from the whole optical fiber. At present, the most common instrument for tension fatigue is Instron.

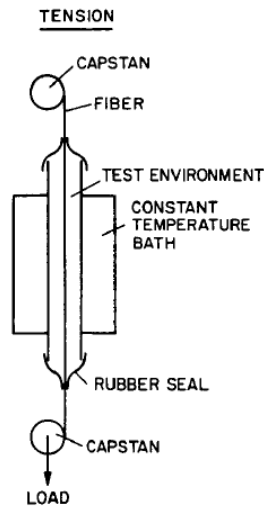


Figure 3.16 Schematic diagram of apparatus for tension fatigue testing of optical fiber [106, 107].

Bunsell firstly revealed that there is a fatigue mechanism in synthetic polymer fiber-nylon fiber in 1971 [108]. When the nylon fiber is loaded cyclically under the steady condition, the fiber fracture could not occur. The fiber fracture happens with the cyclic load from zero minimum load to 50% of break load. The images of fiber fracture show that one end of the fracture fiber has a tail in length of about five times of fiber diameter, as observed in Figures 3.17a and 3.17b. Moreover, a transverse crack is visible, which indicates that a small transverse crack develops and expands along the fiber at an angle of 5° to the fiber axis, as shown in Figure 3.17c. When

the transverse crack propagates half of the fiber, the left part of fiber cross section undertakes all the stress, which results in the ultimate ductile fracture, as described in Figure 3.17d [109].

Bunsell investigated the fatigue mechanism of other polymer fibers such as polyamide, polyester, and polyacrylonitrile fibers in 1974 [110]. Very similar findings are obtained in the investigation and the fatigue fracture of these fibers occurs with a cyclic load from zero to 60% of tensile strength.

The static fatigue of optical fibers was presented by Olshansky in 1976 [111]. The theory of crack growth is applied to analyze the fiber failure of optical fibers subjecting to the long-term loading at a constant stress in a corrosive environment. According to the knowledge that the stress intensity factor at the crack tip is dependent on the flaw size and a geometric factor, the stress corrosion failure distribution is assumed based on the original flaw distribution.

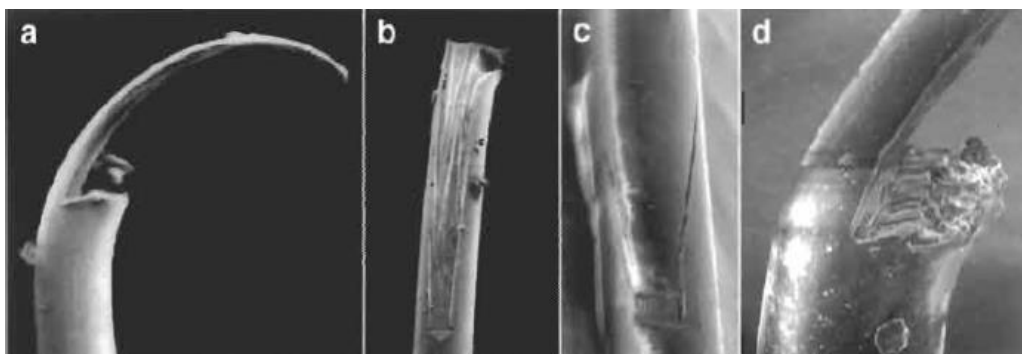


Figure 3.17 Tensile fatigue fracture of nylon fibers [108]: (a-b) fracture tails; (c) small transverse crack; (d) final structure of fracture.

Kurkjian systematically reviewed the investigation of fatigue of silica optical fibers in 1989 [112]. The fatigue behaviour of optical fiber is related to the environmental conditions. In general terms, the flaws in fibers are considered as sharp flaws. The failure strain of optical fiber could be predicted as a function of temperature and absolute humidity. It is summarized the fatigue “knee” of $\log(\text{stress})$ versus $\log(\text{time})$ curve for optical fibers in the conditions of various temperature, relative humidity, pH value, as well as the existence of coating. The fatigue limit of optical fiber is also discussed, since below the stress limit, the strengthening is possible to occur even though there is no degradation. At last, it is generalized that the time dependence of fatigue and aging are not clear for optical fibers in lightguide applications.

Flex fatigue testing

The flex fatigue could be carried out with different apparatus, and the static bending fatigue apparatus used in mandrel bending technique are shown in Figure 3.18.

In the mandrel bending technique [107], the fiber is wound around a precision-ground mandrel. The bending stress is related to the bending radius. In order to minimize the damage of fiber

by touching the mandrel and adjacent windings, the optical fiber should be coated with a protective layer. Another fatal shortcoming of this technique is the holding part of fiber ends. Some methods are chosen to hold both fiber ends. The fiber ends could be either fixed with glue/tapes or gripped mechanically. However, these methods might lead to the premature failure due to the stress concentration or other reasons.

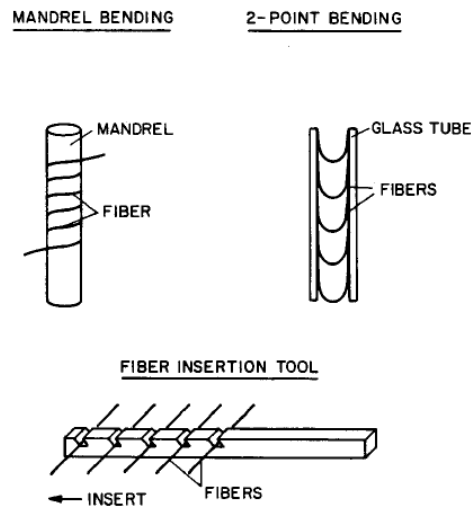


Figure 3.18 Schematic diagram of apparatus for bending fatigue testing of optical fiber [107].

In the two-point bend technique [113], several fibers are bent and inserted into a glass tube. The bending stress is determined by the internal diameter of glass tube. The fiber insertion is finished with the aid of fiber insertion tool, without any influence of fiber loops, as shown in the bottom of Figure 3.18. The fiber fracture is under the acoustic surveillance, when the transducer output crosses a limit, the trigger circuit will launch a pulse which is recorded by a chart recorder.

Compared with mandrel bending technique, the two-bend point technique is more useful due to its advantages. First of all, it is more convenient to test many fiber at once, which saves a lot of time for failure estimation in bending state. At the same time, there is no gripping problem and the glass tube could protect the fibers from accidental damage. Both naked fibers and coated fibers can be investigated by two-bend point technique. Furthermore, the dynamic strength test is obtained directly in this technique [114]. However, there is also some disadvantages which make this technique improper in some cases. For example, the fiber length is short and not suitable to predict the fatigue lifetime of long fibers. The internal diameter of glass tube determines the applied stress and the measured fiber length, resulting in the unclear influence on fatigue lifetime. Moreover, it is inappropriate when the fiber fatigue takes place during fiber mounting and environmental equilibration [107]. Last but not the least, this

technique requires the fibers to be loaded in a bend state, which means, weak fibers are not suitable in this method.

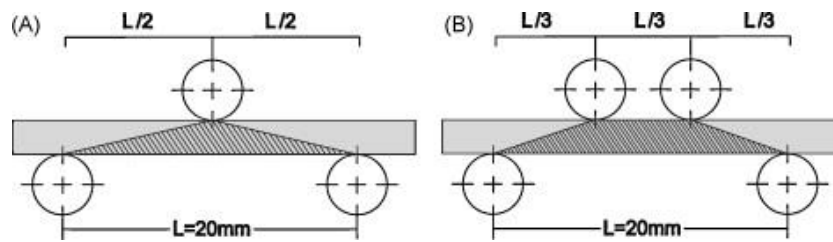


Figure 3.19 Bending fatigue testing: (A) 3-point; (B) 4-point [115].

In the investigation of bending fatigue, there are some other techniques for single fibers. The three-point bending technique and the four-point bending technique are shown in Figure 3.19. In both techniques, the upper rollers are moved downwards at a constant speed to apply the load to samples that are supported by the outer rollers. The former is more common for polymers, the latter is more popular in wood and composite. There are still some disadvantages of these conventional apparatuses, some modified ones are introduced. Nelson proposed a novel four-point bend test for weak fiber samples [116], as shown in Figure 3.20. In this system, the fiber is in touch with four pins: two inner pins on the compressive surface, two outer pins on the tensile surface. The two loading (outer) pins are mounted on a translation stage which is driven by a computer controlled stepper motor. The fiber failure is monitored by using acoustic detection. This modification offers several advantages such as no gripping problem and premature failure, inexpensive manufacturing of this apparatus and so on. However, the high friction between fiber and pins in the case of high deflection might cause the fiber failure during loading, the tested fiber length is short even though it is longer than a two-point sample, and the linear beam bending theory might be not appropriate due to the nonlinear relationship between fiber stress and applied load or displacement.

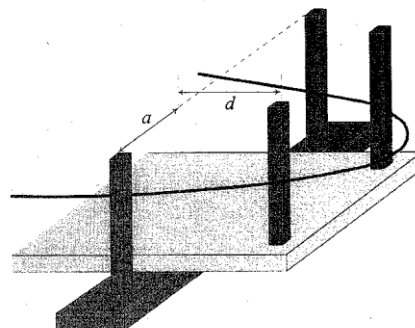


Figure 3.20 Schematic diagram of a modified four-point bending apparatus for fatigue testing of optical fiber [116].

In the practical experiments, the fatigue testing methodology is selected due to different fiber materials. For example, for Kevlar and wool fibers, the surface wear is dominant, the flex testing in terms of non-pin contact should be chosen. For nylon and polyester fibers, the situation is more complex. The failure forms are associated with the bending forces [109].

3.4.4 Analysis of fatigue testing

In general, the results of fatigue testing are analyzed based on fatigue modelling. Fatigue modelling is classified in various ways. One classification of fatigue modelling is introduced here based on the existing fatigue models [117].

Fatigue life models

The fatigue life models are applied for the estimation of fatigue lifetime based on the dependence of stress or strain on fatigue cycles in fatigue life curve ($S-N$ curve, rather than the analysis of degradation mechanism of samples. The prediction of fatigue life based on $S-N$ curve is quite simple. Once the constant amplitude loading is analyzed, the fatigue life then could be predicted.

The $S-N$ curve based approach in fatigue life prediction is employed to investigate the fatigue behaviour of single fiber and composites. Qian used this method to compare the fatigue behaviour between glass fiber and fiber bundles, and found that the glass fiber has longer fatigue life than fiber bundles at low strain rate [118]. Sendekyj investigated the fatigue characterizations of composite materials and proposed three assumptions [119]:

- (1) $S-N$ curves can be expressed by equations. One example is given in Figure 3.21;

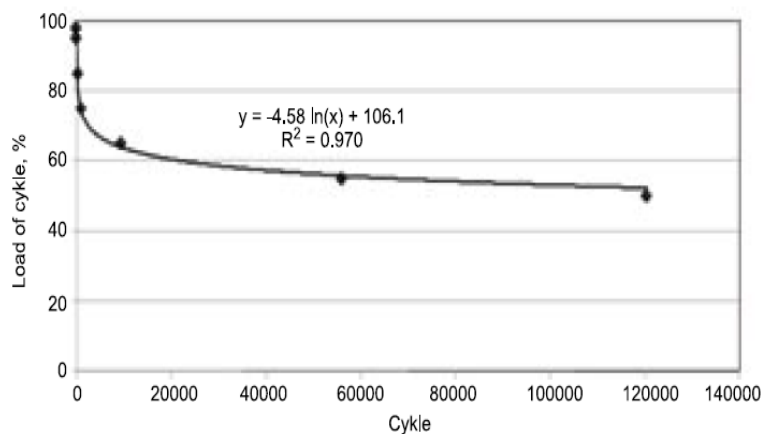


Figure 3.21 Schematic illustration of $S-N$ curve for wool yarns [120].

- (2) The static strength is associated with the fatigue life and residual strength at runout termination in fatigue cyclic testing;

- (3) The static strength data can be evaluated by two-parameter Weibull distribution.

At present, it is widely recognized and accepted that the fiber strength can be described by Weibull distribution. The fiber strength distribution can be generally derived from these assumptions [121, 122]: fiber failure happens to some specific place with catastrophic flaw and fracture probabilities at individual places are mutually independent; the fracture mechanism can be characterized by Weibull distribution function $P(x)$.

The function of three-parameter Weibull distribution is expressed as:

$$P(x) = 1 - \exp \left[-\frac{l}{l_0} \left(\frac{x - W_1}{W_2} \right)^{W_3} \right] \quad (3.29)$$

where W_1 is the shift parameter, W_2 is the scale parameter and W_3 is the shape parameter, l is the gauge length, l_0 is the reference length.

If $W_1 = 0$, Equation (3.29) turns into two-parameter Weibull distribution:

$$P(x) = 1 - \exp \left[-\frac{l}{l_0} \left(\frac{x}{W_2} \right)^{W_3} \right] \quad (3.30)$$

The mean fiber strength $E(x)$ is estimated by:

$$E(x) = W_1 + W_2 \cdot \left(\frac{l}{l_0} \right)^{-1/W_3} \cdot \Gamma \left(1 + \frac{1}{W_3} \right) \quad (3.31)$$

When $l = l_0$, Equation (3.29) and Equation (3.30) are transferred as:

$$P(x) = 1 - \exp \left[-\left(\frac{x - W_1}{W_2} \right)^{W_3} \right] \quad (3.32)$$

$$P(x) = 1 - \exp \left[-\left(\frac{x}{W_2} \right)^{W_3} \right] \quad (3.33)$$

And the mean fiber strength $E(x)$ is written as:

$$E(x) = W_1 + W_2 \cdot \Gamma(1 + 1/W_3) \quad (3.34)$$

The suitable selection of moments [123] was carried out and three nonlinear equations were created to calculate the three Weibull parameters. Cran used this technique for estimation of the three parameters of Weibull distribution [124]. Parameters W_1 , W_2 , W_3 can be estimated from the following equations:

$$W_3 = \frac{\ln(2)}{\ln(m_1 - m_2) - \ln(m_2 - m_4)} \quad (3.35)$$

$$W_1 = \frac{m_1 \cdot m_4 - m_2^2}{m_1 + m_4 - 2m_2} \quad (3.36)$$

$$W_2 = \frac{m_1 - W_1}{\Gamma(1 + 1/W_3)} \quad (3.37)$$

where $\Gamma(x)$ is the Gamma function. m_r is the so-called Weibull sample moment that is:

$$m_r = \sum_{i=0}^{N-1} \left(1 - \frac{i}{N_m}\right)^r (x_{(i+1)} - x_{(i)}) \quad (3.38)$$

where $x_{(0)} = 0$ when $i = 0$.

For two-parameter Weibull distribution:

$$W_3 = \frac{\ln(2)}{\ln(m_1) - \ln(m_2)} \quad (3.39)$$

The quantile-quantile (Q-Q) plot and Weibull distribution based on Equation (3.32) could be combined to estimate the distribution of number of fatigue cycles to break [125]. Classical Q-Q plot is based on comparison of empirical quantile function $Q(P_i) \approx x_{(i)}$ with chosen theoretical quantile function $QT(P_i)$. The probability estimator:

$$P_i = \frac{i}{N_m + 1} \quad (3.40)$$

where P_i is the probability of fiber failure, N_m is the number of measurements. The values of fiber tensile strength are arranged in a rising order and so-called increasing order statistics are as follows:

$$x_{(1)} < x_{(2)} < \dots < x_{(n)} \quad (3.41)$$

Corrected Weibull three Q-Q plot is obtained with the linear fitting function $y = ax+b$. Here:

$$y = \ln[-\ln(1 - P_i)] \quad (3.42)$$

$$x = \ln(x_{(i)} - W_1) \quad (3.43)$$

$$a = W_3 \quad (3.44)$$

$$b = -W_3 \ln(W_2) \quad (3.45)$$

There are some other methods to calculate the Weibull shift parameter W_1 . W_1 is generally estimated with following equations:

$$\widehat{W}_{10} = x_{(1)} \quad (3.46)$$

$$\widehat{W}_{10} = 0.5 x_{(1)} \quad (3.47)$$

where $x_{(1)}$ is the lowest value or the first value in order statistics.

Then the Weibull scale parameter is calculated by:

$$\widehat{W}_{20} = \frac{2.989}{\ln[(\tilde{x}_{0.97} - x_{(1)})/(\tilde{x}_{0.17} - x_{(1)})]} \quad (3.48)$$

where $\tilde{x}_{0.97}$ and $\tilde{x}_{0.17}$ are the quantile values.

Wyckoff described another method that is related to the scale parameter described in Equation (3.48) [126],

$$\widehat{W}_{11} = \bar{x} - \frac{(x_{(1)} - \bar{x})}{N^{-1/\widehat{W}_{20}} - 1} \quad (3.49)$$

Zenbil deducted that the shift parameter could be expressed with the first two values in order statistics [127],

$$\widehat{W}_{12} = \bar{x} - \frac{x_{(2)} - x_{(1)}}{C(W_2)} \quad (3.50)$$

$$C(W_2) = N_m \left[\left(\frac{N_m}{N_m + 1} \right)^{1/W_2} - 1 \right] \quad (3.51)$$

where W_2 is calculated from Equation (3.48) as well.

Zanakis proposed a new calculation method based on $x_{(i)}$ only [128],

$$\widehat{W}_{13} = \frac{x_{(1)}x_{(N_m)} - x_{(2)}^2}{x_{(1)} + x_{(N_m)} - 2x_{(2)}} \quad (3.52)$$

where $x_{(2)}$ is the second lowest value in order statistics, $x_{(N_m)}$ is the highest value in order statistics.

Another simple estimate is a combination of all order statistics [129, 130]:

$$\widehat{W}_{14} = 2x_{(1)} - (1 - e) \sum_{i=1}^N x_{(i)} / e^i \quad (3.53)$$

where e is a mathematical constant and equals 2.71828 approximately. More calculation methods for Weibull parameters are summarized in [131].

Phenomenological models for residual stiffness or strength

In residual strength or stiffness models, the degradation of strength or stiffness of materials is discussed. There is an inherent failure criterion in residual strength models, which reveals that the failure takes place if the applied stress is the same as the residual strength [60, 132]. In residual stiffness models, it is assumed that the failure happens if the modulus declines to a critical value. For instant, Hahn [133] and O'Brien [134] elaborated that when the fatigue secant modulus is equal to the secant modulus in a static test, the fatigue failure happens.

Progressive damage models

In this category, progressive damage models describe the fatigue failure of material with specific defects like the transverse matrix cracks. In the crack growth study, the crack generally grows when the material is under a constant stress in a corrosive environment, e.g. water or water vapour.

The crack with critical size grows at a critical velocity when the product of the applied stress and the crack size is the same as the fracture toughness; in addition, the crack grows at a subcritical velocity when the applied stress is less than the critical value. The fatigue behaviour is influenced by both temperature and relative humidity [112, 135].

Chapter 4 Experimental Materials and Methods

4.1 Materials

The materials employed in this thesis were naked POFs, prepared by Grace POF Co., Ltd., Taiwan. Table 4.1 shows the basic characterization of POFs. All POFs display the same structure that possess core and cladding layers. All cores have the same polymer that is PMMA, all claddings have the same composition which is blended by PMMA and polytetrafluoroethylene (PTFE/Teflon), and the corresponding refractive indices are 1.49 and 1.42, respectively. There are five diameters in total, the minimal bending radii of all POFs are the same and eight times of fiber diameter.

Table 4.1 Technical data of all POFs.

Basic properties	Grace POF
Core material	PMMA
Cladding material	PMMA/Teflon
Jacket material	no
Fiber diameter [mm]	0.25/0.4/0.5/0.75/1.0
Core refraction index	1.49
Cladding refraction index	1.42
Numerical aperture	0.44
Wavelength [nm]	400 ~ 780
Limit of bending radius	$8 \times$ fiber diameter

4.2 Methods

4.2.1 Tensile testing

The basic mechanical properties of single fiber regarding the tensile properties were investigated at first. The stress-strain experiments for all POFs were carried out on Instron at 20 °C and 65% relative humidity. The testing speed was set as 300 mm/min. The gauge length was 100 mm. 50 times were averaged for each.

4.2.2 Strength distribution

The relationship of fiber strength and gauge length of 0.75 mm POF was investigated by Instron at 20 °C and 65% relative humidity. The testing speed was designed as 100 mm/min. The gauge lengths were chosen as 30, 50, 75, 100, 150 and 200 mm. 50 times were averaged for each.

The tensile fiber strength distribution was estimated by Weibull distributions described in Equation (3.29) and Equation (3.30). The most direct and simple experimental method to obtain Weibull parameters is the single fiber test with large number. The failure probability P_i is obtain as follows [136],

$$P_i = \frac{i - 0.3}{N_m + 0.4} \quad (4.1)$$

where N_m is the number of measurements. The values of fiber tensile strength are arranged in a rising order.

The dependence of fiber strength on gauge length was estimated by Equation (3.31).

4.2.3 Nanoindentation testing

The nanoindentation testing in terms of hardness property, creep deformation and interphase property between core and cladding of 0.5 mm POF were proceeded by Hysitron with a three-side pyramidal Berkovich diamond indenter. The typical load-displacement curve of POF is presented in Figure 4.1. The effects of fiber diameter and cross section direction on hardness property were also discussed.

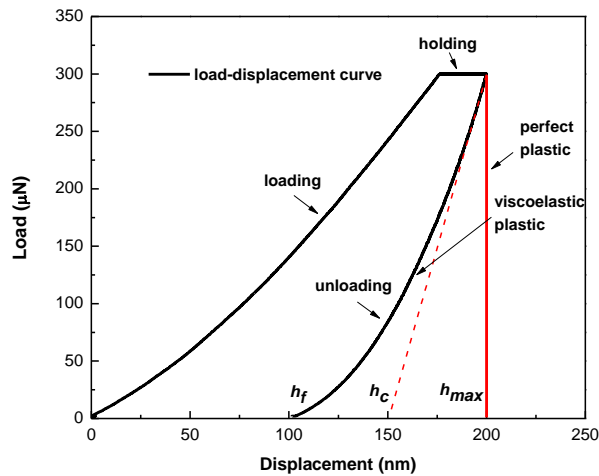


Figure 4.1 Typical load-displacement curve of POFs.

The preparation of latitudinal and longitudinal cross sections of 0.5 mm POF for nanoindentation testing is described below:

- (1) For preparation of latitudinal cross sections, a bundle of fibers were put into suitable cables which were inserted into appropriate holes of button for normal clothes. Super glue was used to fix all parts as an unmovable unit. The cable with fibers inside was cut in both sides of the button.
- (2) For preparation of longitudinal cross sections, the fibers were arranged straightly one by one on the glass slides (1 cm × 1 cm) by using the super glue.
- (3) Both fibers in buttons and on glass slides were polished by polishing papers with different sizes. The smallest particle diameter of polishing papers used was 1 micro. Then the samples were fine-polished with W0.5 water-based diamond polishing paste until the surface roughness was small enough for nanoindentation testing. All samples

were polished in the clockwise direction manually with the speed of 50 ~ 60 times per minute. The samples in latitudinal cross section and longitudinal cross section were prepared at last.

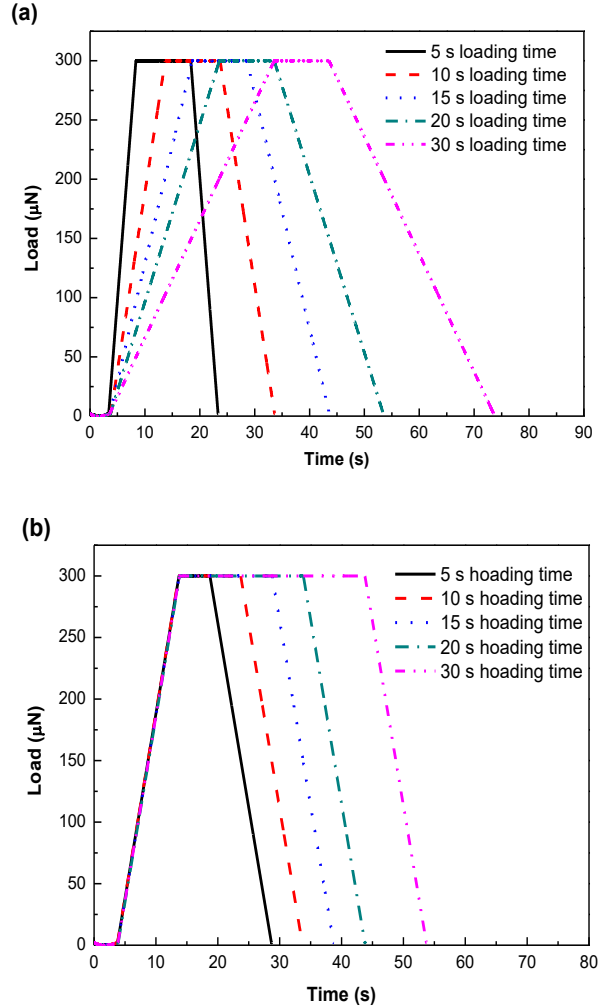


Figure 4.2 Experimental design of nanoindentation creep testing of 0.5 mm POF under 0.3 mN maximum load: (a) loading rate sensitivity; (b) holding time sensitivity.

The nanoindentation testing for 0.5 mm POF was conducted in two ways: when the holding time t_H was 10 s, the loading time t_L varied from 5 s to 30 s (Figure 4.2a); when the loading time was 10 s, the holding time shifted from 5 s to 30 s (Figure 4.2b). For both ways, the unloading time was the same as the loading time and the maximum load was set as 0.3 mN.

The interphase properties between core and cladding in POF was also investigated by nanoindentation technique. The maximum nanoindentation depths were 120, 80, 40 nm and relevant spacings of 1900, 1300, 700 were used to avoid overlapping of plastic deformation zones between adjacent indents, one example is given in Figure 4.3. POFs were tested from cladding to core in the line through the center of cross section.

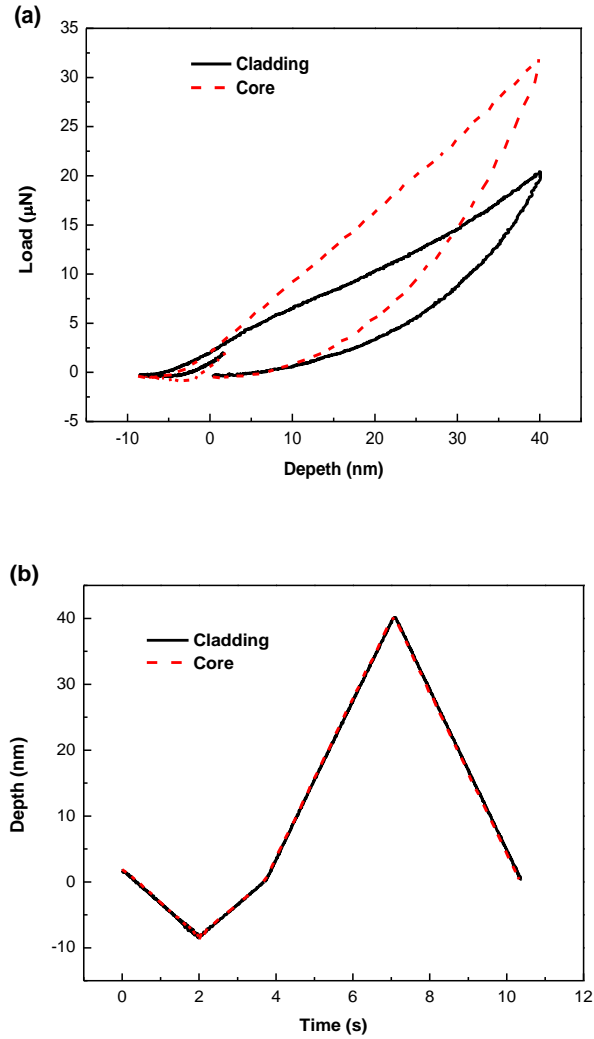


Figure 4.3 Experimental data for interphase properties of POF under 40 nm maximum depth and 400 nm spacing: (a) load-depth curve; (b) depth-time curve.

4.2.4 Tension fatigue testing

In this investigation, the tension fatigue testing of selected POFs was proceeded by Instron at 20 °C and 65% relative humidity. Due to the comparatively visible strain response during the stress-strain testing, the force was uncontrollable during tension fatigue testing even though the sensitive force sensor was utilized. For thin POFs, the strain responses under tension fatigue testing corresponding to creep were totally unexpected. Therefore, only the results of POFs with diameters of 0.5 mm, 0.75 mm and 1.0 mm were discussed here.

Each sample was measured with constant applied load that was relevant to its ultimate tensile strength. The loading time was the same as unloading time, which was 2.5 s. The initial gauge length was 100 mm. 20 times were averaged for each.

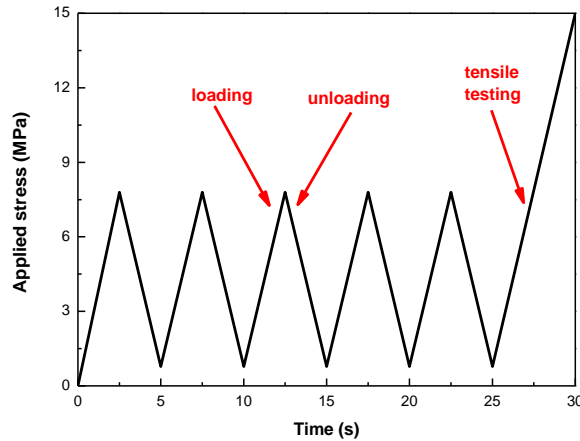


Figure 4.4 Testing design for tension fatigue of 0.5 mm POF under 5 fatigue cycles.

In the program of tension fatigue testing, the maximum applied load was 60% of maximum tensile strength and the minimum applied load was 10% of the maximum applied load (the stress ratio was 0.1), as shown in Figure 4.4. Tensile testing after tension fatigue testing was also conducted under the same experimental conditions described in section 4.2.1. The practical stress-strain curve combined with tension fatigue testing and tensile testing after that of 0.5 mm POF under 5 fatigue cycles is illustrated in Figure 4.5.

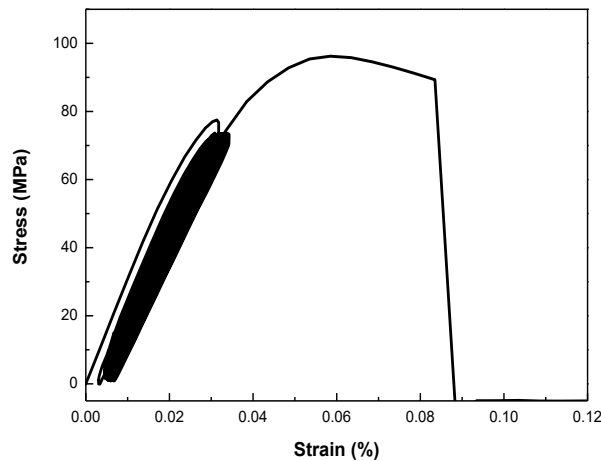


Figure 4.5 Practical stress-strain curve of 0.5 mm POF in tension fatigue testing under 5 fatigue cycles and subsequent tensile testing.

4.2.5 Flex fatigue testing

The flex fatigue properties of all POFs were carried out on Flexometer described in Figure 4.6 at 20 °C and 65% relative humidity. The testing was aimed to evaluate the flex fatigue lifetime of POF based on the number of bending cycles to failure.

This testing was with zero suppressed tension which means the stress level is zero, the maximum stress exhibits the different sign and the same value as the minimum stress. The POFs with 300 mm length were clamped to the upper jaw that provided an adjustable pre-swing radius for measurements, and inserted into the lower jaw which makes fibers move in the vertical direction rather than horizontal direction. The measurements can be performed manually after disconnection of transmission system, which is suitable for very brittle materials. The swing angle in this work was designed in the range of $20 \sim 160^\circ$, and the drive motor connected to the upper jaw was set as 100 which was related to the swing speed of 116 times per minute. Figure 4.6 shows the fiber under both straight state (solid lines) and bending state (dash lines). The movement of fiber is repeatable and starts from the middle place to the right side first, then to the left side. The testing could stop manually when the fiber failure happens. When the fiber is in the left part, left bending occurs; when the fiber is in the right part, right bending occurs. The fiber is only bent during the bending zone that is 8 cm, as described in Figure 4.6, from the edge of the upper jaw to the edge of the lower jaw. The weight m could be applied to the free end of POFs. 10 samples can be tested at the same time. 50 times were averaged for each type of POFs.

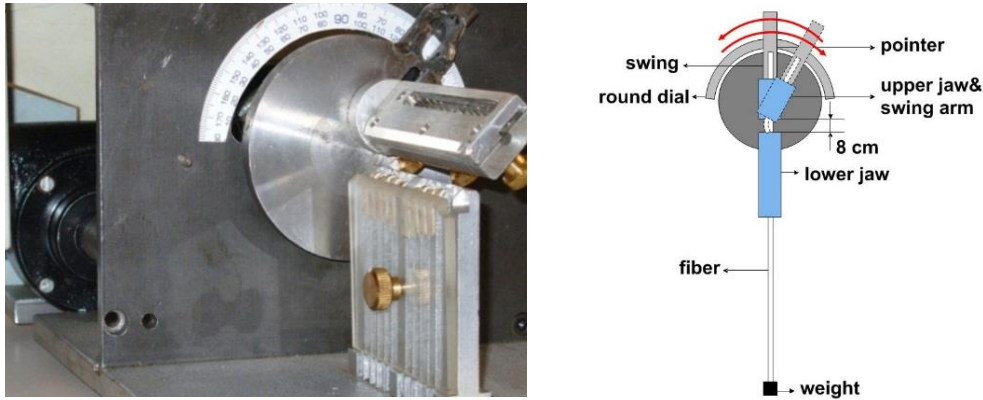


Figure 4.6 Prototype device to measure resistance to bending (left) and corresponding schematic diagram of side view (right).

In this work, the Q-Q plot and Weibull distribution based on Equation (3.32) were combined as the exploratory data analysis method to estimate the proper distribution of number of bending cycles N . The relations among fiber diameter, number of bending cycles and flexibility were also estimated based on the double logarithmic curves.

The flexibility F_l of single fiber is given as follows:

$$F_l = \frac{64}{E\pi d^4} \quad (4.2)$$

where d is the fiber diameter, E is the initial modulus.

The flex fatigue behavior of 0.25 mm POF was investigated by Flexometer as well. The pretension σ related to the external force from the weight m was calculated based on ultimate tensile strength σ_{uts} ,

$$\sigma = \frac{mg}{\pi(d/2)^2} = \alpha_c \cdot \sigma_{uts} \quad (4.3)$$

where g is the earth acceleration (9.80665 m/s²), α_c is the ratio of elaborated fatigue strength to ultimate tensile strength based on the experience. Generally speaking, the empirical value of α_c is in the range of 50 ~ 98% for tensile testing and bending technique.

The fatigue sensitivity coefficient could be calculated according to Equation (4.4) from the normalized $S-N$ curve,

$$\frac{\sigma_a}{\sigma_{uts}} = 1 - b \cdot \log(N) \quad (4.4)$$

where σ_a is the peak of applied pretension, the constant b related to the slope of the normalized $S-N$ curve is considered as the fatigue sensitivity coefficient. The value of b is remarkably close to 0.1 for chopped E-glass strand composites [105].

4.2.6 Scanning electron microscopy

The surface morphology of fiber fracture after tensile testing and flex fatigue testing was observed by scanning electron microscopy (SEM) at 20 kV acceleration voltage, after gold coating.

4.2.7 Fourier transform infrared spectroscopy

The Fourier transform infrared spectroscopy (FTIR) spectra was applied to investigate the material of POF cladding, which was recorded with FTIR spectrometer that was continuously purged with pure nitrogen gas (40 mL/min), in order to eliminate the spectral contributions caused by the atmospheric water vapor.

Chapter 5 Results and Discussion

5.1 Tensile properties

The results from tensile testing of all POFs are illustrated in Figure 5.1. It is observed from the figure that the fiber diameter has an evident influence on tensile property. Both tensile strength and strain change in the same manner for all POFs, which drop as the fiber diameter rises. There is an opposite relation between tensile strength or strain value and fiber diameter.

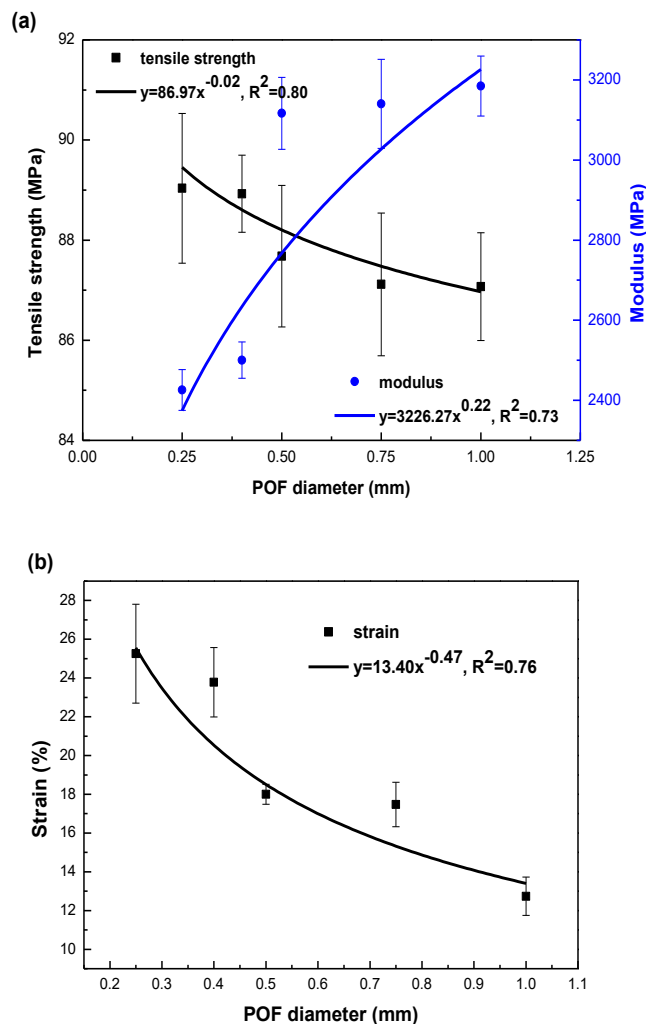


Figure 5.1 POFs with different diameters: (a) tensile strength and modulus; (b) strain.

The phenomenon in tensile strength might be explained by the weakest-link theory. The surface flaws that occur with a statistical nature increase with large surface area, which leads to small tensile strength. The crosshead speed for all POFs keeps constant, that is to say, the extension rate of crosshead for each POF is the same. The thin fiber is generally less stiff than the thick fiber. The ability of deformation for thin fiber is higher and the corresponding extension is

larger. Thereby, the thick fiber initiates lower strain rate as expected. Beside, POF has two layers, which are made of different materials, representing different mechanical properties. The thicker the POF diameter, the larger the interface area, the more uneven the adhesion force between layers. Therefore, the thick POF is estimated to fracture with small values of tensile strength and strain.

The results of modulus are surprising because it is contrary to the widely accepted assumption that the material modulus is an intrinsic property and should be constant. In present investigation, it points out that the thicker the fiber diameter, the higher the fiber modulus of POF. The similar phenomenon of modulus has been found in [137]. It might reveal that the increases in both strength and strain with small fiber diameter are attributed to the accumulation of each point in fiber, or distributed over the whole mass of fiber. The value of modulus is thus changed as a result of dissimilar increases in strength and strain. The reason for such behavior might be related to the non-linear ductile properties (bi-linear curve with an obvious “knee” shown in Figure 5.2) and the visco-elastic behavior of POF.

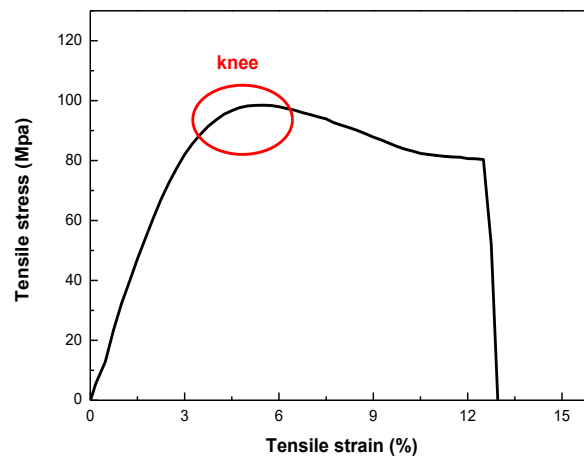


Figure 5.2 Practical stress-strain curve of 0.5 mm POF.

As a new material introduced in textile applications, POF has different fracture mechanism in tensile testing from textile fibers. In the tensile fracture mechanism of textile fiber, when an external force is applied on a fiber, at the initial stretching state, the main deformation of fiber comes from the deformation of bond length and bond angle of macromolecular chains. The stress-strain curve is nearly straight, in accordance with Hook's law. In the simple spring and dashpot model, the elastic part is assumed as the spring which stores as much energy as possible, the plastic part is considered as the dashpot which resists as much energy as possible. When the external force is applied, the perfectly elastic material can return to the original shape, the same as the visco-elastic material, even though it will take time to do so due to the viscous components. While, the plastic material cannot return to its original shape.

If the external force keeps on increasing, the macromolecular chains in the amorphous region deform further in order to overcome the secondary bond force between molecular chains. At this moment, a part of macromolecular chains are straight, and intense chains could break or pull out from the irregular crystalline region. The breakage of secondary bond force results in the dislocation and slippage of macromolecular chains in amorphous regions. Accordingly, the fiber deformation is significant and the modulus decreases. It is considered that the fiber steps into the yield zone [138].

When the dislocated macromolecular chains are basically straight and parallel to each other, the distance of macromolecular chains is close, the new secondary bond force might form between macromolecular chains. If the fiber is still under stretch, the deformation of fiber is mainly resulted from the changes of bond length and bond angle of molecular chains, as well as the breakage of secondary bond force between molecular chains. It is considered that the fiber goes into the strengthening zone. The fiber modulus increases further until the breakage of fiber macromolecular chains, and most of the secondary bond force occurs. Thereby, the fiber fracture takes place [138].

The situation in PMMA based POF is more complicated. First of all, the material of PMMA presents its own characterizations during tensile testing. At room temperature, there are two kinds of molecular bonds in fiber networks in PMMA: stretching and non-stretching. The 3D network, formed by curled molecular chains with non-stretching molecular bonds, is filled with molecular chains with stretching molecular bonds. Before PMMA reaches its yield limit, both two fiber networks are under rigid glassy state, the external force is shared by both networks. Therefore, below the yield limit, the material is elastic. When PMMA exceeds its yield limit, the stretching curled molecular chains could change conformation, and are stretched along the direction of external force, finally, PMMA deforms, and the force is fully applied to the fiber network with non-stretching curled molecular chains. Even if the force is unloaded, the stretching curled molecular chains cannot recover to its original length since they are straight already. Meanwhile, they restrict the movement of fiber network with deformed non-stretching curled molecular chains. That means, the non-stretching fiber network is consolidated in PMMA, which results in a permanent plastic deformation [139]. Secondly, the core/skin structure of POF requires more consideration in the differences between core characterization and cladding characterization, the interphase property between core and cladding, the fiber evenness in length and so on.

5.2 Strength distribution

Figure 5.3 shows the values of tensile strength, modulus and strain from the tensile experiments of 0.75 mm POF with different gauge lengths. The results indicate that the gauge length plays an important role in tensile properties. With the increment of gauge length, the value of tensile strength drops slightly, the strain value decreases markedly and the modulus increases visibly.

The phenomenon in tensile strength might be explained by the weakest-link theory, as discussed in section 5.1. The crosshead speed for all fibers with six lengths is the same, which means the extension rate of crosshead for each fiber keeps the same, as a result, the longer fiber initiates lower strain rate. The modulus value increases with increasing gauge length. The reason behind it could be attributed to the modulus calculation method mentioned previously which is dependent on the different changes in strength and strain.

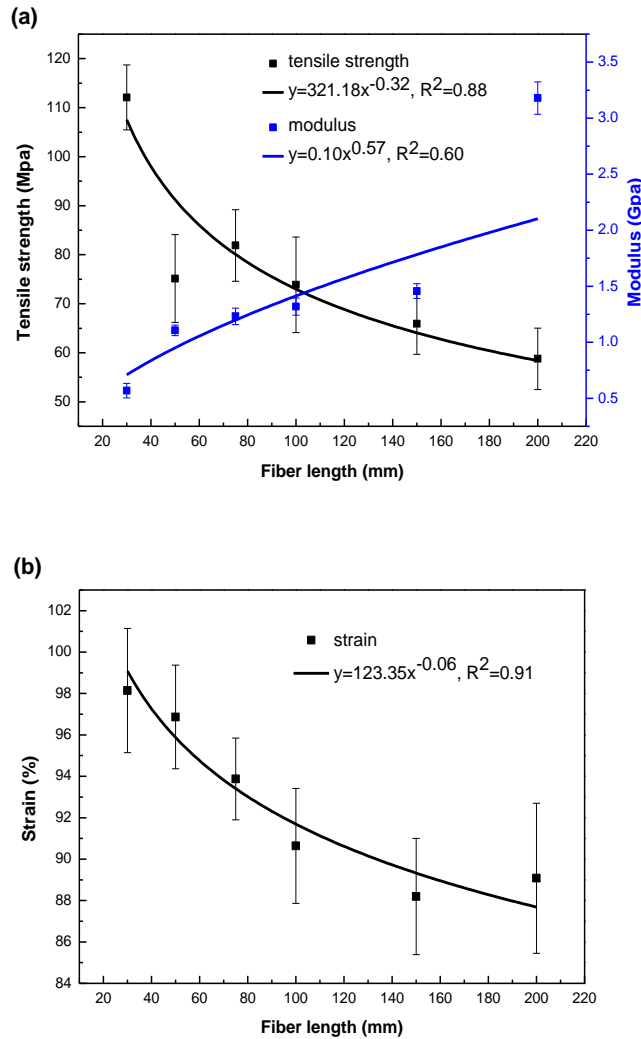


Figure 5.3 0.75 mm POF with different gauge lengths: (a) tensile strength and modulus; (b) strain.

Figures 5.4-5.5 present the experimental and theoretical results of probability of fiber failure of 0.75 mm POF with six gauge lengths. It is observed from these figures that it is almost coherent between experimental and theoretical results by using both two-parameter and three-parameter Weibull strength distributions when the gauge length is assumed to be the same as the reference length, even though some fitting results are not perfect enough, e.g. the fitting curve of two-parameter Weibull distribution for 30 mm gauge length, as shown in Figure 5.6.

Moreover, there is no obvious difference between results based on two-parameter and three-parameter Weibull strength distributions. It implies that both two-parameter and three-parameter Weibull strength distributions could be good models for estimation of strength distribution of 0.75 mm POF when the gauge length equals the reference length.

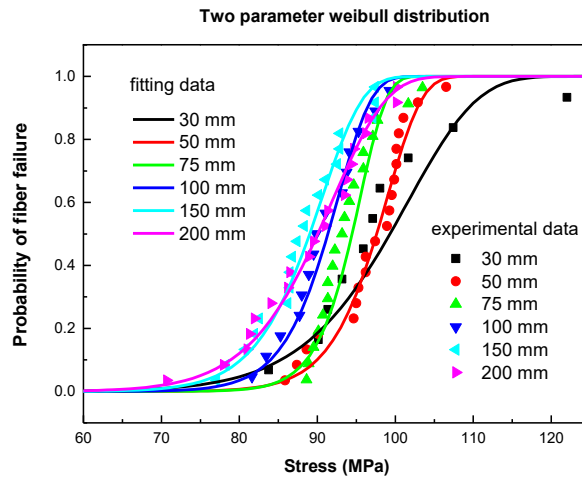


Figure 5.4 Two-parameter Weibull strength distribution of 0.75 mm POF with different gauge lengths ($l = l_0$).

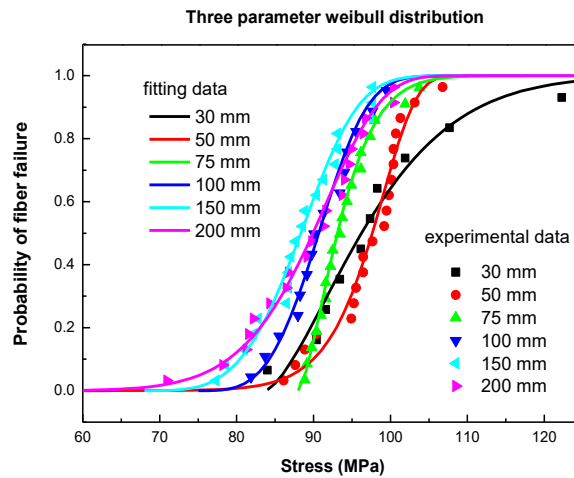


Figure 5.5 Three-parameter Weibull strength distribution of 0.75 mm POF with different gauge lengths ($l = l_0$).

However, when the gauge length is assumed to be 1 mm, the two-parameter Weibull strength distribution gives an inconsistent fit, as shown in Figure 5.6. There is an evident shift between experimental data and fitting data.

It is summarized that, therefore, the three-parameter Weibull strength distribution is more preferred to be the model of estimation of strength distribution of 0.75 mm POF in terms of various gauge lengths.

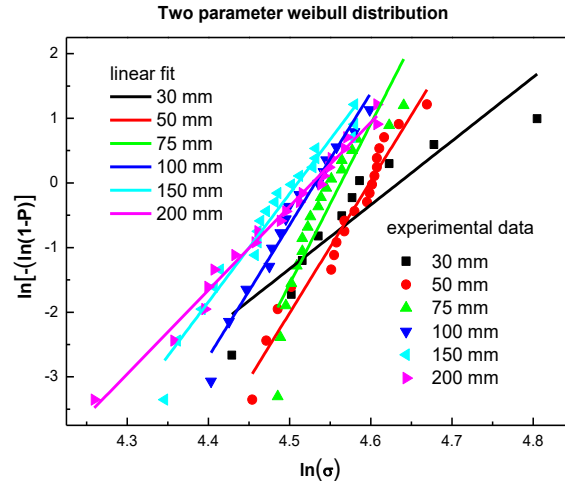


Figure 5.6 Plots of $\ln(-\ln(1-P))$ versus $\ln(\sigma)$ of 0.75 mm POF with different gauge lengths ($l = l_0$).

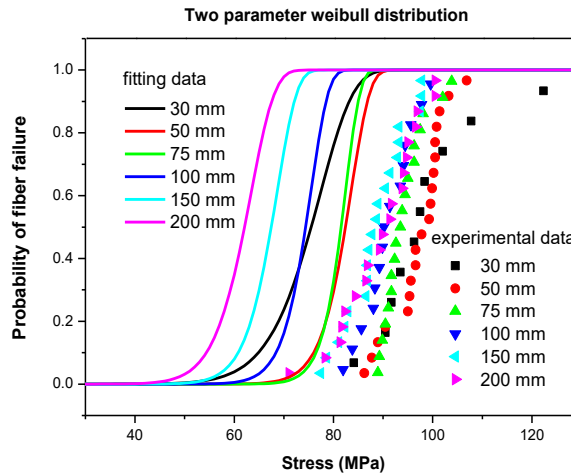


Figure 5.7 Two-parameter Weibull strength distribution of 0.75 mm POF with different gauge lengths ($l_0 = 1$ mm).

The three-parameter Weibull distribution can be used to not only estimate the strength scatter, but also predict the dependence of strength on gauge length. The Weibull shift parameter W_l is the lower limit of strength and equals to 70.7716 MPa from Figures 5.4-5.5, the scale and shape parameters can be obtained from the fitting equation of Weibull distribution based on 1 mm reference length, as shown in Equation (5.1),

$$y = -33.04 + 9x \tag{5.1}$$

Here, $W_3 = 9$ and $W_2 = 39.38$.

The variance of mean fiber strength is predicted and described in Equation (5.2), and the relationship between mean fiber strength and gauge length is shown in Figure 5.8,

$$y = 70.77 + 37.29x^{-0.11} \tag{5.2}$$

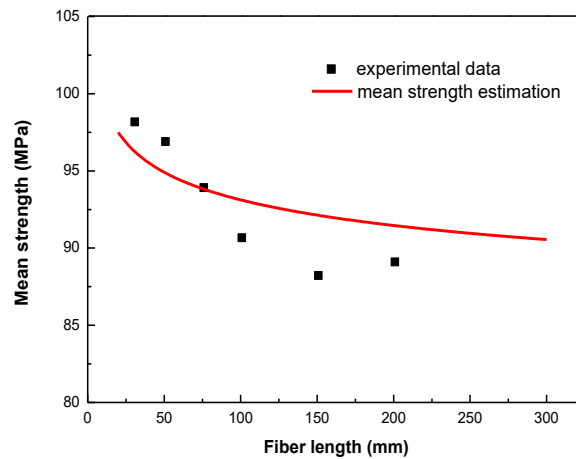


Figure 5.8 Relation between mean fiber strength and gauge length of 0.75 mm POF.

5.3 Nanoindentation properties

5.3.1 Surface roughness

In the measurement of topography of samples, the scan size of all images was set as $5 \mu\text{m}$. One example is shown in Figure 5.9 and the relevant image statistics are given in Table 5.1.

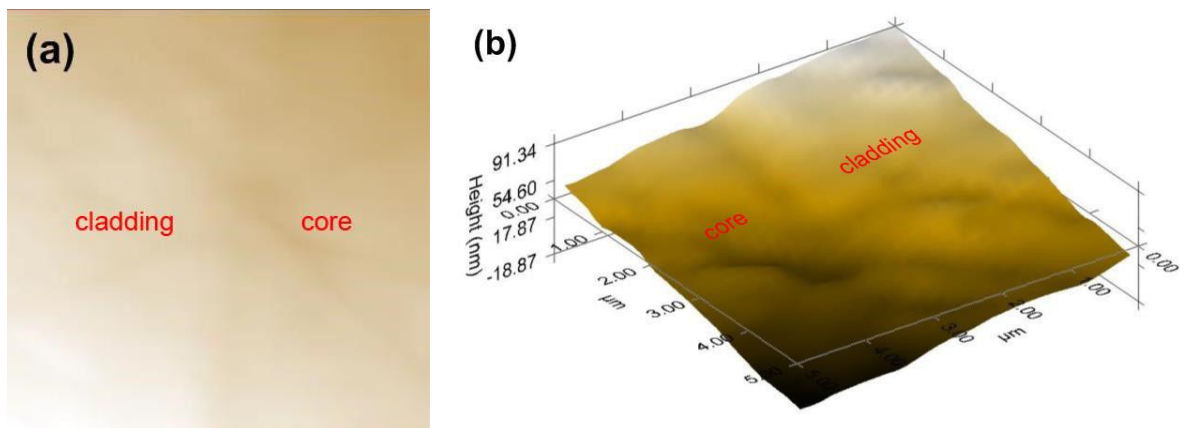


Figure 5.9 Latitudinal cross section of 0.5 mm POF: (a) 2D height image; (b) 3D height image.

The POF cladding in Figure 5.9 is on the left-hand side in 2D image, which is in the right part of 3D image. The left part represents the POF core. It is observed that the sample surface is not absolutely smooth, there are some small peaks and valleys in both images, which could be attributed to the manual polishing processes.

The value of nanoindentation depth should be larger than the root mean square (RMS) surface roughness in order to minimize the influence of surface roughness on testing results [140]. The value of root mean square surface roughness for each sample is less than 40 nm in this investigation.

Table 5.1 Whole image statistics of latitudinal cross section of 0.5 mm POF.

Parameters	Values
Project area [μm^2]	25
RMS roughness (R_q) [nm]	33.415
Average roughness (R_a) [nm]	21.694
Mean height [nm]	29.053
Max height [nm]	94.181
Min height [nm]	-392.754
Peak-to-valley [nm]	486.934

5.3.2 Loading rate effect on nanoindentation creep

The nanoindentation creep displacements of core and cladding of 0.5 mm POF latitudinal cross section with different loading times are shown in Figure 5.10, the corresponding fitting parameters based on Equation (3.21) is listed in Table 5.2.

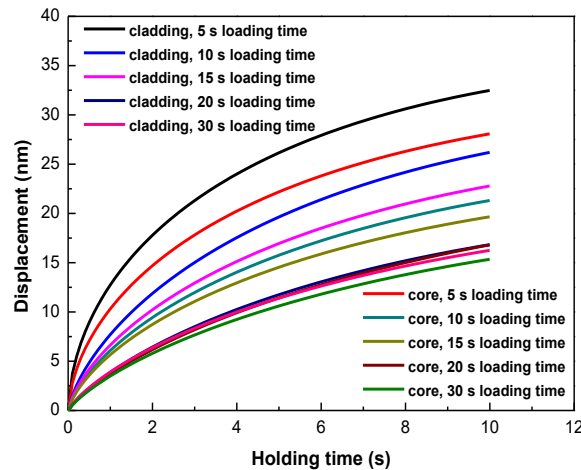


Figure 5.10 Creep displacement of 0.5 mm POF with different loading rates.

First of all, the fitting equation gives a good fit to all experimental data with high values of coefficient of determination R^2 and small values of reduced chi-square χ_{red}^2 , as seen in Table

5.2. Secondly, all the curves in Figure 5.10 change in the similar manner. The creep displacement goes up distinctively at the beginning stage of holding period corresponding to the transient creep, and then raises at a relatively gentle increasing rate at the followed steady-state stage [141]. Moreover, the higher the loading rate (the lower the loading time), the bigger the creep displacement. It could be ascribed to the lower strain rate with smaller loading rate, therefore, the longer time is required to reach the maximum load, resulting in the creep deformation during the loading time [142]. It could be also explained by the dislocation substructure that is formed beneath the indenter due to different indentation stresses with various strain rates, and this substructure might play a significant role in the subsequent creep behavior [143].

Table 5.2 Parameters of fitting curves of creep displacement versus holding time of 0.5 mm POF ($t_i = 0$ s).

t_L [s]	0.5 mm POF	Values				Statistics	
		h_i	a	m	k	χ_{red}^2	R^2
5	cladding	294.487	15.483	0.587	-2.740	0.023	0.9996
	core	185.857	13.054	0.628	-2.741	0.016	0.9996
10	cladding	323.429	14.535	0.813	-6.828	0.011	0.9997
	core	260.459	11.424	0.815	-5.334	0.007	0.9998
15	cladding	361.729	11.921	0.802	-5.283	0.013	0.9996
	core	270.930	10.139	0.803	-4.481	0.013	0.9995
20	cladding	-895.480	-45.385	1.020	49.249	0.007	0.9997
	core	4291.454	177.633	0.995	-173.936	0.005	0.9997
30	cladding	733.988	17.448	0.939	-13.538	0.013	0.9993
	core	5876.499	172.532	0.995	-169.042	0.014	0.9992

Figure 5.11 (a) gives one example with the sample under the condition of 10 s loading time and 10 s holding time, the results show a good fitting match with experimental data by Equation (3.21) based on the coefficient of determination $R^2 = 0.9998$. The corresponding strain rate is calculated by Equation (3.19), as illustrated in Figure 5.11 (a). It is observed that, at the very early beginning of holding period, the displacement increases markedly at a high strain rate from $0.05 \sim 0.025 \text{ s}^{-1}$, representing the transient creep. With the increment of holding time, the displacement increases at a gradually saturated strain rate at 0.005 s^{-1} with respect to a steady-state strain [141]. Figure 5.11 (b) shows the related stress exponent.

The variation of stress exponent of 0.5 mm POF at different loading times is displayed in Figure 5.12. It is discovered from this figure that the loading time or loading rate plays a significant role in stress exponent value. The stress exponent decreases gradually with increasing loading time. In this investigation, the maximum indentation depth is approximately 300 nm that is still less than 10% of the sample thickness ($1 \sim 1.5 \text{ cm}$), in another word, the influence of substrate is the least [144]. It is convincing that the stress exponent can be calculated from the curve of

log(strain rate) versus log(stress), as illustrated in Figure 5.11 (b). It is concluded that the stress exponent is sensitive to the loading time or loading rate, and 0.5 mm POF has a very strong loading rate sensitivity (LRS) in stress exponent.

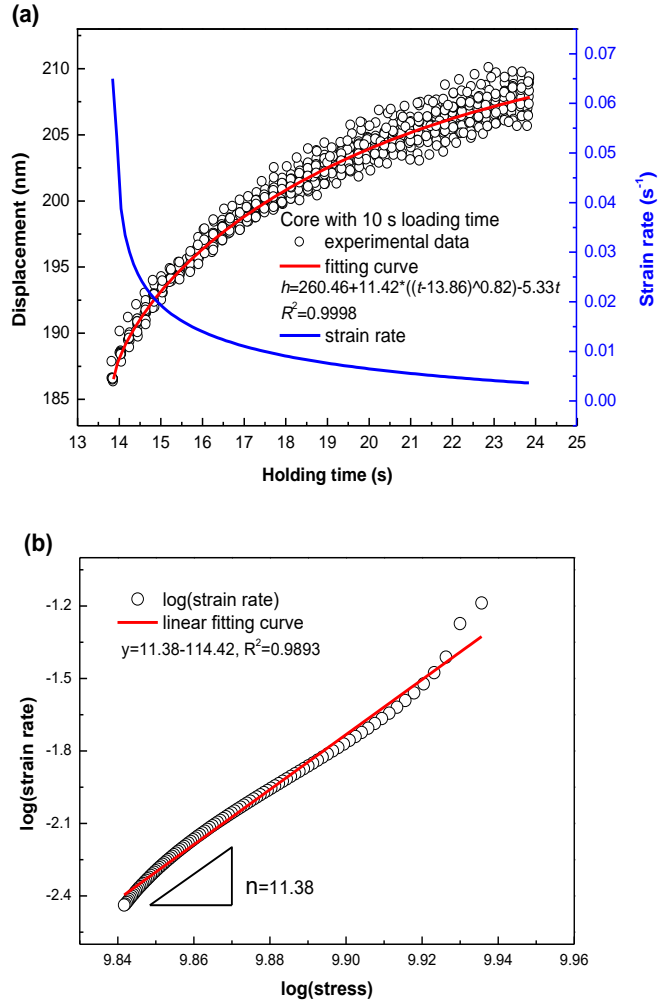


Figure 5.11 0.5 mm POF core with 10 s holding time and 10 s loading time: (a) curves of displacement and strain rate versus holding time; (b) corresponding curve of log(strain rate) versus log(stress).

To understand the creep mechanism of 0.5 mm POF in depth, both values of hardness and elastic modulus are investigated at various loading times, as shown in Figure 5.13. For all samples, both hardness and elastic modulus increase with decreasing loading time or increasing loading rate. When the loading time is lower, the loading rate is higher, the shorter time is allowed to creep, and the smaller indent is created in the end of holding period, which leads to greater hardness due to the smaller contact area according to Equation (3.18). The higher elastic modulus at higher loading rate implies that, with higher loading rate, the less creep occurs during the loading period, and the creep phenomenon could remain in the subsequent unloading time when the elastic modulus is measured.

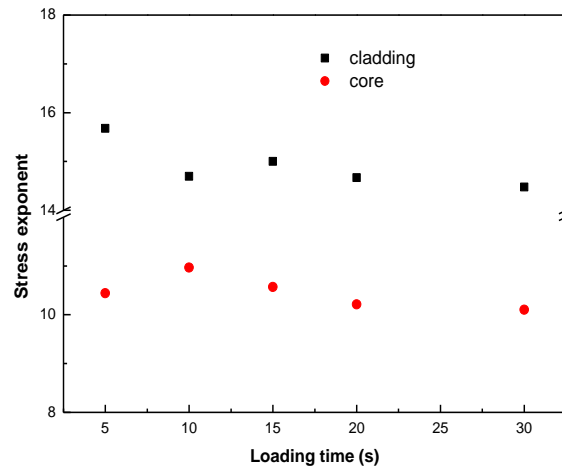


Figure 5.12 Dependence of stress exponent on loading time of 0.5 mm POF.

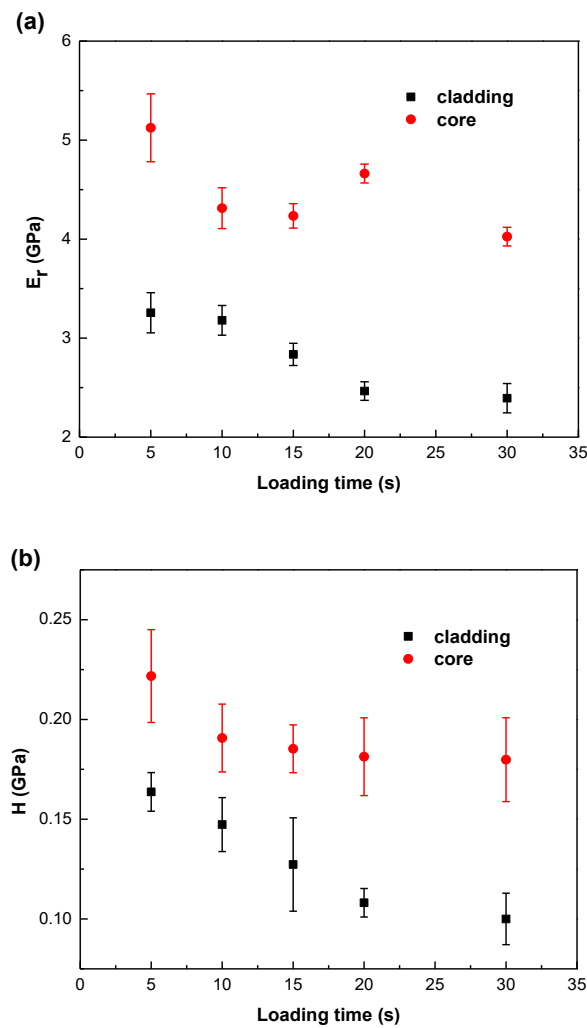


Figure 5.13 0.5 mm POF with 10 s holding time: (a) elastic modulus; (b) hardness.

Based on the theory of Oliver and Pharr method, the contact between indenter tip and sample surface is assumed to be purely elastic during the unloading process. In fact, the contact is far from purely elastic. The creep phenomenon during unloading period could result in the overestimated value of contact stiffness [145-147].

The creep phenomenon in 0.5 mm POF might be induced by plasticity or micro-structure. Given that the fiber is constituted by core and cladding, the interphase between two parts is not clear. The variation of micro-structure in each part may influence its creep phenomenon unexpectedly. It is urgent to figure out the interphase property of 0.5 mm POF. Furthermore, the intrinsic creep mechanism of POF requires more investigation in future.

5.3.3 Holding time effect on nanoindentation creep

The holding time effect on nanoindentation creep of 0.5 mm POF latitudinal cross section is discussed here. There is no doubt that the displacement increases as the holding time goes up, as shown in Figure 5.14. For both core and cladding, the values of hardness and elastic modulus decrease with the increase in holding time, as shown in Figure 5.15. The longer holding time could provide the indenter to create a larger contact area, leading to the higher value of hardness. At the same time, the longer holding time could also provide enough time for sample to creep, which means the less creep phenomenon could be observed during the unloading period when the modulus is calculated.

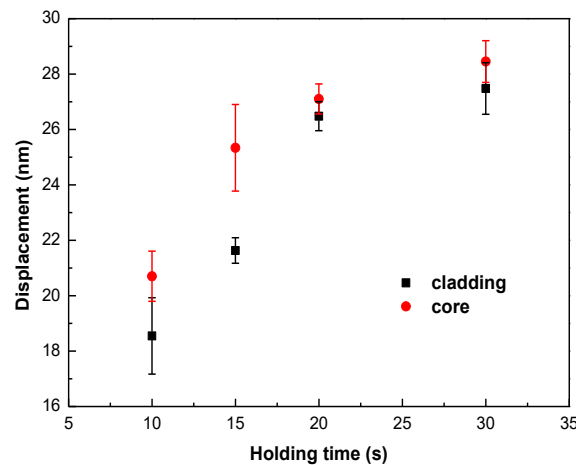


Figure 5.14 Displacement of 0.5 mm POF with different holding times.

On the other hand, the changes of hardness and elastic modulus are visibly smaller in the testing at various holding times than in the testing at various loading times. It indicates that holding time sensitivity (HTS) of 0.5 mm POF in nanoindentation creep might be less evident than LRS.

Furthermore, the results of cladding at 10 s holding time are imperfect, which might be caused by the manual polishing processes. The surfaces of fiber samples are not absolutely smooth,

which might affect the contact areas. Generally, it is more difficult to polish soft materials than hard ones (like metal). In present work, it is relatively easy for core to produce a smooth surface with less time during which the cladding is uneven. It would lead to the unexpected data in final results. Moreover, the limited number of measurements for each condition may also influence the results.

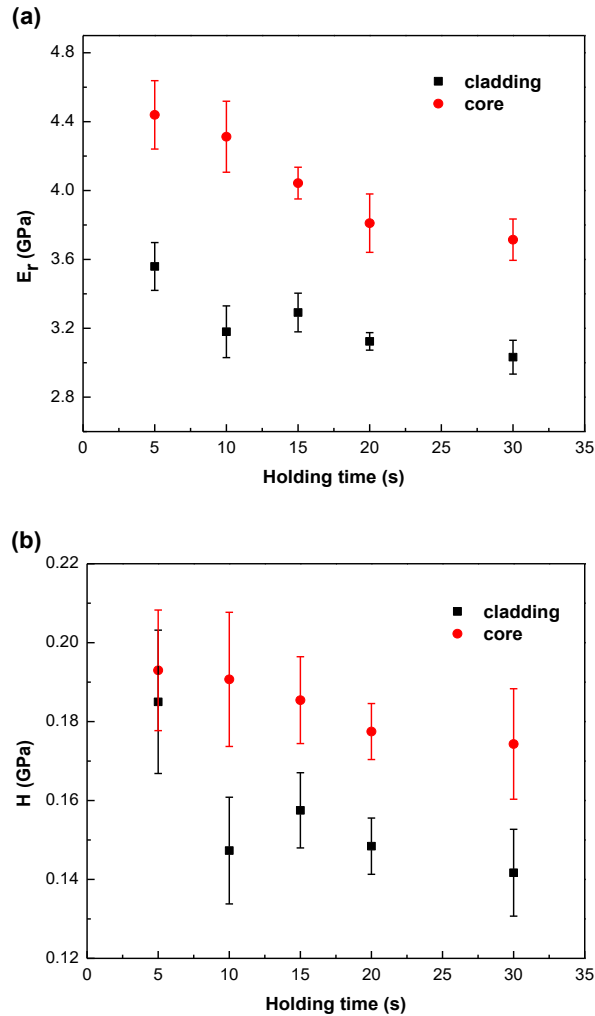


Figure 5.15 0.5 mm POF with 10 s loading time: (a) elastic modulus; (b) hardness.

5.3.4 Fiber diameter effect on hardness property

Figure 5.16 illustrates the effects of fiber diameter and cross section direction on the values of hardness and elastic modulus. It is observed that the results are different with different fiber diameters. The values of hardness and modulus are higher with thicker fiber diameter. The results of investigation of effect of cross section direction indicate that the higher values of hardness and modulus could be obtained in the longitudinal cross section of POF during nanoindentation testing.

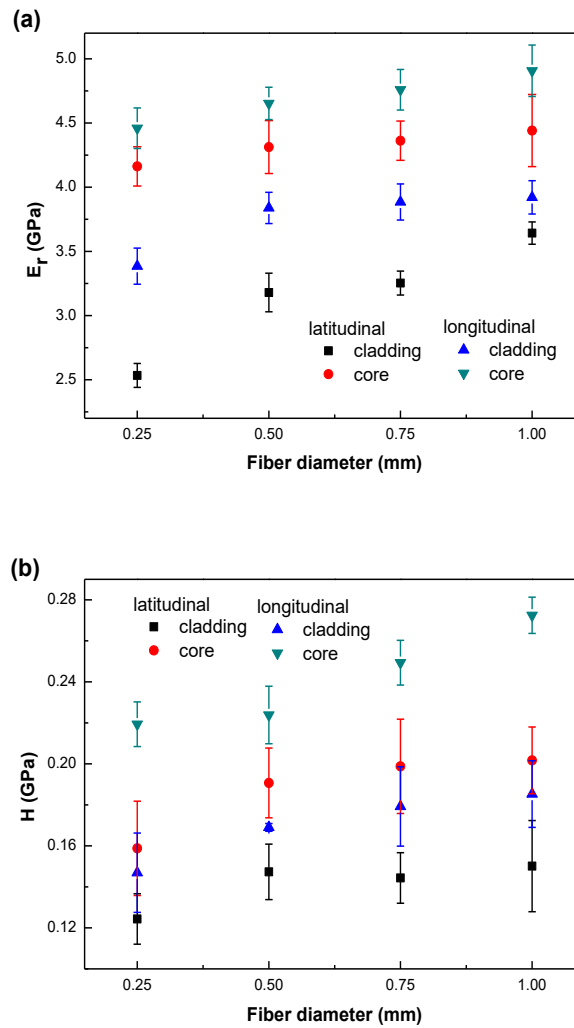


Figure 5.16 POFs with different diameters and different cross sections: (a) elastic modulus; (b) hardness.

It is widely accepted that the properties should be the same with the same materials. However, the experimental results vary evidently. The reason behind it could be due to the different surface roughness caused by the manual polishing processes for sample preparation. The surfaces of samples are not absolutely smooth and could not possess the same surface roughness, as shown in Figure 5.17, which might affect the contact areas during nanoindentation testing, leading to various results. It might be also attributed to the unknown intrinsic properties of POFs in different cross sections or with different diameters, and the limited number of measurements.

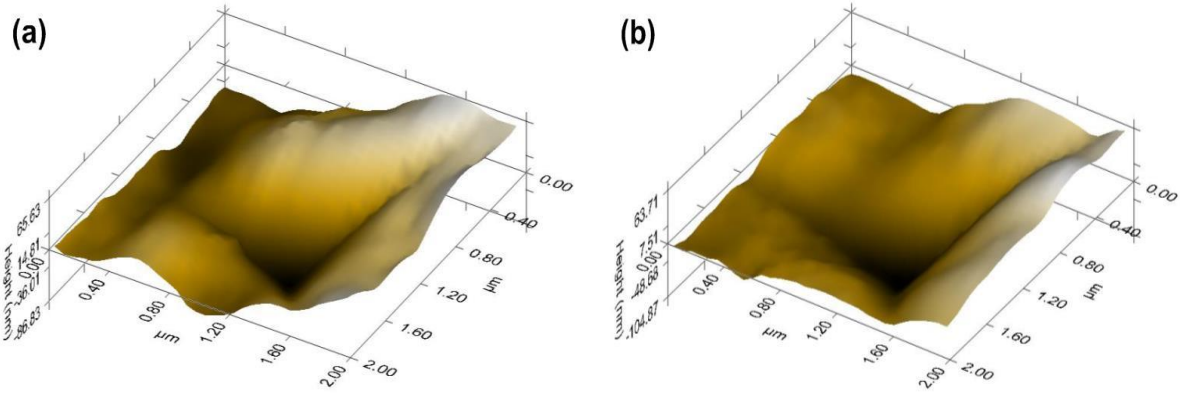


Figure 5.17 Indent images of longitudinal cross section of 0.5 mm POF: (a) cladding; (b) core.

5.3.5 Interphase property

According to the RMS surface roughness in Table 5.3, 120 nm nanoindentation depth (approximately 3 times of the value of RMS) is totally sufficient to investigate the relatively constant elastic modulus and hardness of 0.5 mm POF. Based on the Equation (3.24) and Equation (3.25), the spacing between adjacent indents is designed as 1900 nm. The results in Figure 5.18 indicate that the interphase thickness between core and cladding is less than 1900 nm due to no point existing in transition zone (considered as interphase region) between two groups of values.

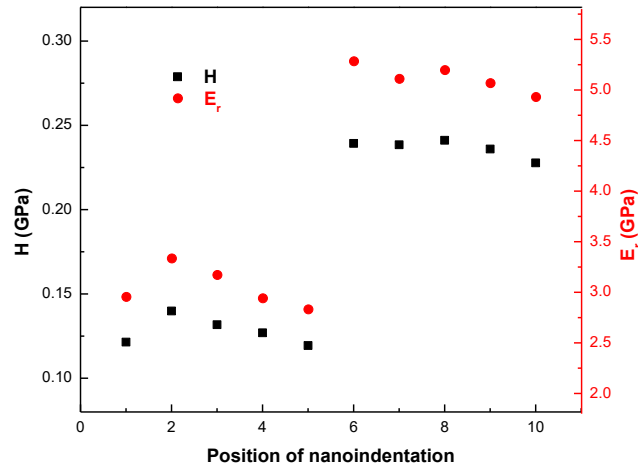


Figure 5.18 Hardness and elastic modulus of 0.5 mm POF with 120 nm depth and 1900 nm spacing.

There is only one apparent point in the transition zone in Figure 5.19 when the nanoindentation depth reduces to 80 nm (approximately 2 times of the value of RMS). 1300 nm spacing is chosen as the interval between any two adjacent indenters, which means, there are two possibilities of nanoindentation in the interphase region. Either the only one point is located in

the middle area of interphase region with the width of 0 ~ 2600 nm, or the point is very close to the border lines of interphase region with the width of 0 ~ 1300 nm, as shown in Figure 5.20. However, it is still hard to predict the exact interphase width with only one indent. When the nanoindentation is near to the core, the plastic zone would be restricted due to the greater elastic modulus and hardness of core than those of cladding. To obtain more effective interphase width, the nanoindentation depth should be smaller.

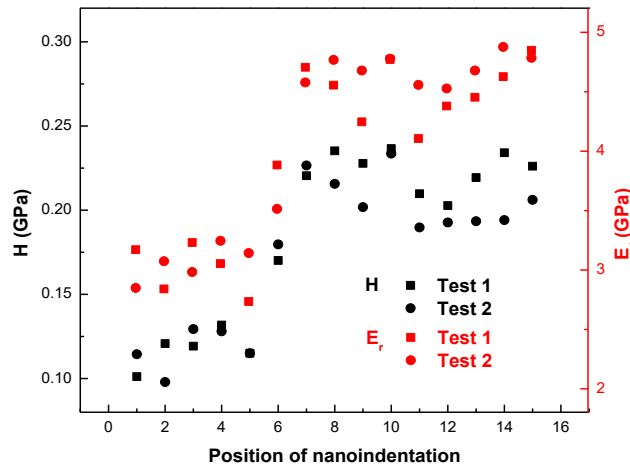


Figure 5.19 Hardness and elastic modulus of 0.5 mm POF with 80 nm depth and 1300 nm spacing.



Figure 5.20 Possibilities of one indent with 80 nm depth and 1300 nm spacing in the interphase region.

When the nanoindentation depth declines to 40 nm (close to the value of RMS), the spacing between each two adjacent indentations is around 700 nm, two indents in the transition zone could be observed in both values of hardness and elastic modulus, as shown in Figure 5.21. Apparently, there are three possibilities of indent locations, as given in Figure 5.22. Accordingly, it is estimated that the interphase width could be in the range of 700 ~ 1900 nm, which is still a wide range and not satisfied enough with the minimum nanoindentation depth.

When the nanoindentation depth is 40 nm, the nanoindentation width is calculated as 302 nm, which means, the minimum safe spacing to avoid the overlapping of the plastic zones between each two adjacent indents is 608 nm. If the spacing is 302 nm, each two adjacent indents would be connected rather than overlapped, while the plastic zones would be definitely overlapped.

In this case, the overlapped plastic zones would affect the following results, whereas it is still meaningful to estimate relatively effective interphase width with minimum nanoindentation depth and more sensitive spacing.

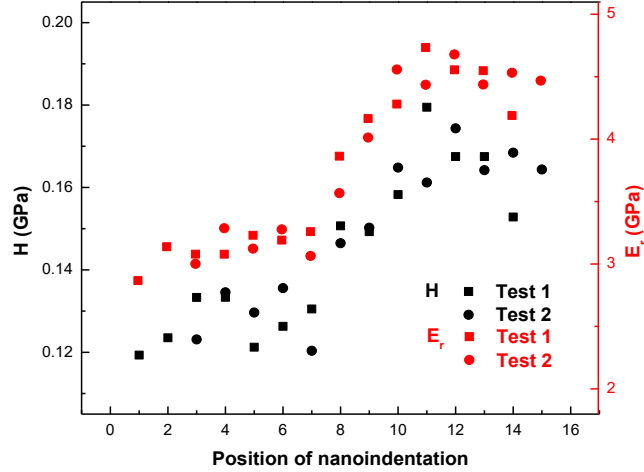


Figure 5.21 Hardness and elastic modulus of 0.5 mm POF with 40 nm depth and 700 nm spacing.

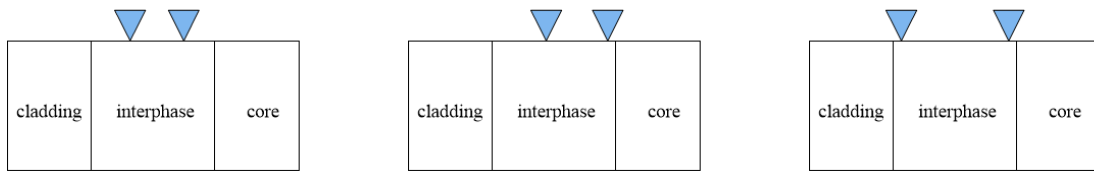


Figure 5.22 Possibilities of two indents with 40 nm depth and 700 nm spacing in the interphase region.

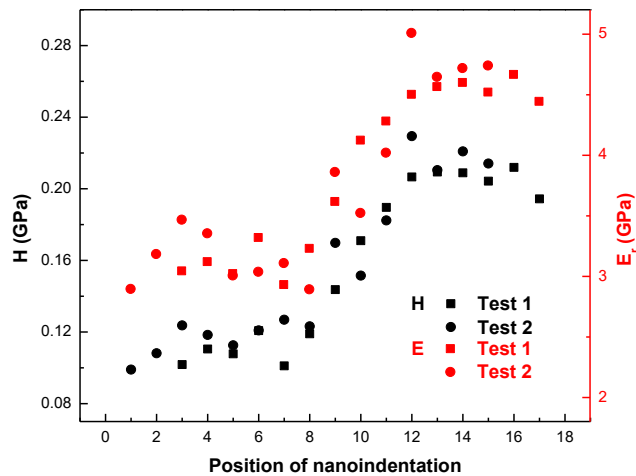


Figure 5.23 Hardness and elastic modulus of 0.5 mm POF with 40 nm depth and 400 nm spacing.



Figure 5.24 Possibilities of three indents with 40 nm depth and 400 nm spacing in the interphase region.

The corresponding results are summarized in Figures 5.23-5.24. There are three indents during the transition zone and two possibilities of indent locations in the interphase region. Based on the above results, the interphase width could be estimated as 800 ~ 1600 nm.

5.4 Tension fatigue properties

5.4.1 Extension response under constant stress amplitude

Figure 5.25 depicts the variations of total extension and cyclic extension of selected POFs during tension fatigue testing. It is observed that, under the same alternating external stress, both total extension and cyclic extension go up evidently with the increment of total fatigue cycles. Moreover, both corresponding increasing rates decline gradually with increasing fatigue cycles.

During the dynamic fatigue testing, the applied strength is generally less than the yield strength. The fundamental reason resulting in the fatigue of plastic material is caused by the viscoelasticity. Under the alternating external stress, the deformation of molecular chains in plastic material always lags behind the stress, which could produce the internal friction, leading to a large amount of heat. This part of heat might accumulate due to the poor thermal conductivity, consequently, the temperature of material itself increases, resulting in the partial softening and melting. The fatigue failure is affected by a lot of factors, such as the internal defects, internal shrinkage, surface scratches, nicks, and roughness of plastic material.

Under the same alternating external stress, the plastic material might have two kinds of deformations, one is reversible and another is not. When the deformation is caused by the changes of bond length and bond angle in molecular chains, it is instantaneous and small; when the deformation is caused by the change of conformation of molecular chains, it is large. Both changes are elastic deformation and reversible, while the latter one needs time to relax. Thus, it is observed that the extension of POF is recoverable visibly when the applied load is minimum, as shown in Figure 5.26. When the deformation is caused by the relative slippage of molecular chains, it is irreversible and needs longer time to accumulate. This kind of deformation in dynamic fatigue testing is recognized as viscous deformation.

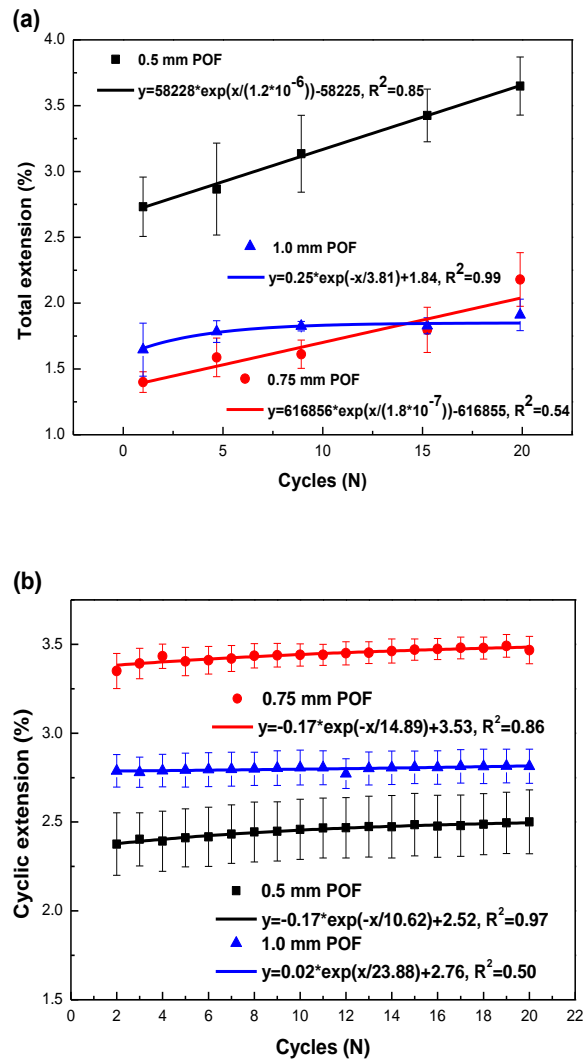


Figure 5.25 POFs in tension fatigue testing: (a) total extension; (b) cyclic extension.

During dynamic tension fatigue testing, if the unloading time is not sufficient for elastic deformation to recover completely or a part of deformation is resulted from the viscous deformation, the extension at the point of maximum applied load for each cycle would accumulate gradually and the total extension thus goes up with increasing fatigue cycles, as shown in Figure 5.26.

Moreover, it is visible from Figure 5.25 that the fiber diameter has different influences on values of total extension and cyclic extension. POF with 0.5 mm diameter displays higher total extension value and lower cyclic extension value than POFs with 0.75 mm and 1.0 mm diameters. According to the results from tensile testing, the fiber diameter also plays a role in strain value. However, the reason behind it is more complex. The initial gauge lengths and the loading times for three POFs are the same, while the maximum applied loads are different, that is to say, the crosshead speeds are different. The thinner the fiber diameter, the lower the breaking load in tensile testing, the slower the crosshead speed in tension fatigue testing, and

the lower the extension rate of fiber. Relatively speaking, the thinner POF has more time to deform during tension fatigue testing. In this case, it is more possible for bond lengths and bond angles to extend, and molecular chains to go straight and slip. Therefore, the total extension should be higher for thinner POF.

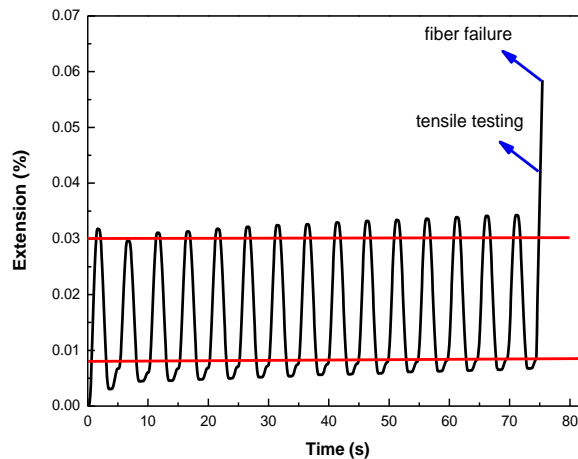


Figure 5.26 Extension versus time curve of 0.5 mm POF in tension fatigue testing with 15 fatigue cycles.

The reason for low cyclic extension for 0.5 mm POF could be due to the high value of extension at the point of minimum applied load in each fatigue cycle shown in Figure 5.26. The recovered elastic deformation is the difference between the extension at the point of maximum applied load and the extension at the point of minimum applied load during the same loading cycle, which is considered as the cyclic extension. Given that the unloading time is relatively sufficient for elastic deformation of thinner fiber to recover, it is assumed that a large proportion of viscous deformation might exist during each fatigue cycle and accumulate gradually in thinner fiber.

5.4.2 Tensile property after tension fatigue testing

Figures 5.27-5.29 exhibit the changes of tensile properties of POFs after tension fatigue testing before fiber fracture.

The number of fatigue cycles has an evident effect on the tensile properties. With the increase in fatigue cycles, the values of tensile strength, modulus and strain decrease markedly with 1 and 5 fatigue cycles, and decline slightly after 5 fatigue cycles. It is observed that the decreasing rates of all values vary with various fiber diameters. The thicker the POF, the higher the decreasing rate. The similar phenomena could be also found in Figure 5.30, which presents the relationship between the area under stress-strain curve and the fatigue cycles for three POFs. It indicates that the thicker fiber is more sensitive to tension fatigue cycles during dynamic tension fatigue testing. It might be explained by the large interphase area between core and

cladding in thick POF, which could result in the high possibility of uniformity problem of interphase adhesion. Another reason could be attributed to the various proportion of core or cladding in all POFs. The ratio of core to cladding is variable in different fibers according to the results in Table 5.3 and Figure 5.31. That means, the respective contributions of core and cladding to the mechanical properties of the whole fiber are not the same in each POF. In addition, the cladding is not perfectly even in thickness. The results of measures diameters and corresponding standard deviations *SD* and variation coefficients *CV* of all fibers by image analysis are shown in Table 5.3. Even though the cladding is a relatively thin layer in POF, while its role in fiber properties could not be ignored due to its different material composition.

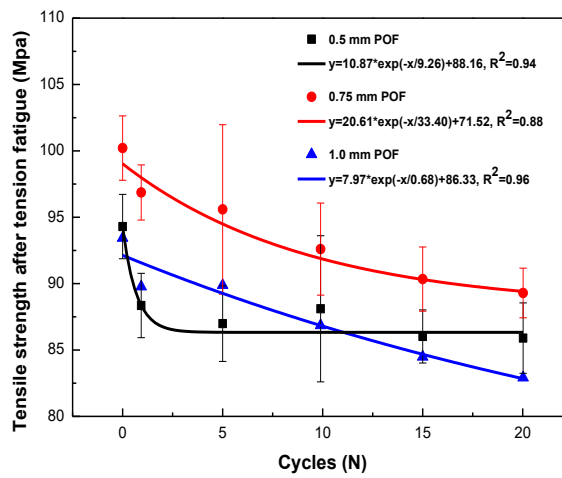


Figure 5.27 Tensile strength of POFs after tension fatigue testing.

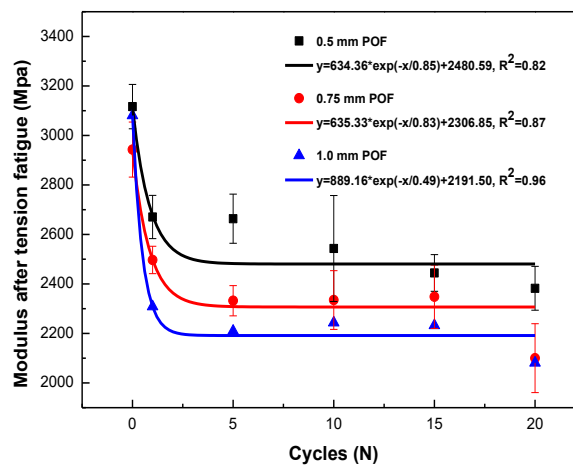


Figure 5.28 Modulus of POFs after tension fatigue testing.

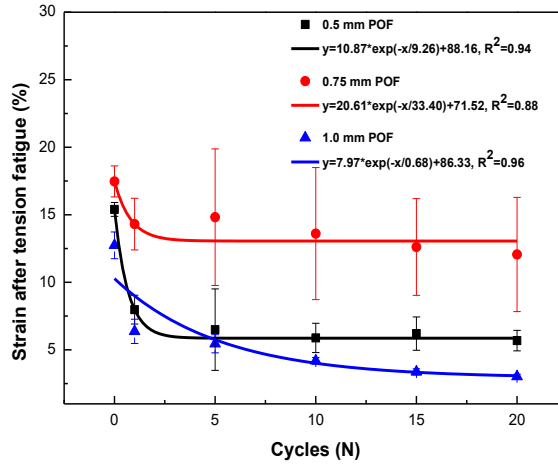


Figure 5.29 Strain of POFs after tension fatigue testing.

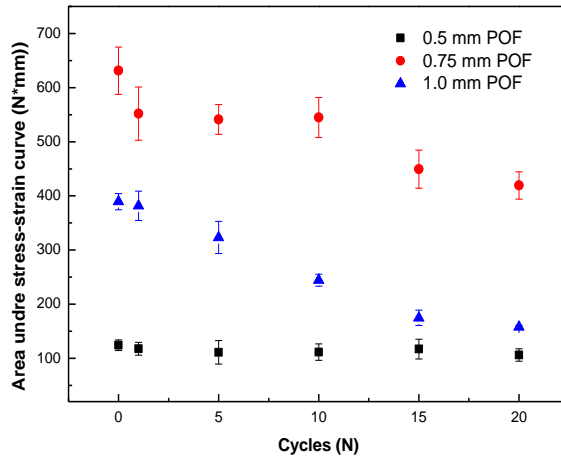


Figure 5.30 Comparison of areas under stress-strain curves of POFs after tension fatigue testing.

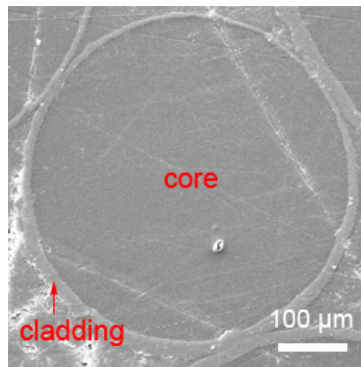


Figure 5.31 SEM image of latitudinal cross section of 0.25 mm POF.

Table 5.3 Measured diameters of fiber and core of all POFs by image analysis.

d [mm]		Measured d [μm]	SD [μm]	CV [%]
0.25	fiber	239.63	12.70	5.13
	core	225.49	11.59	4.97
0.4	fiber	398.67	2.25	0.56
	core	376.73	2.12	0.56
0.5	fiber	510.50	3.78	0.74
	core	483.03	3.98	0.83
0.75	fiber	742.48	4.20	0.56
	core	703.45	3.98	0.56
1.0	fiber	934.45	4.38	0.47
	core	888.31	4.48	0.50

As given in Table 4.1, the material of cladding is composed of PMMA and PTFE. Figure 5.32 gives one example of the FTIR analysis. It describes the peaks of infrared absorption for cladding material of 1.0 mm POF.

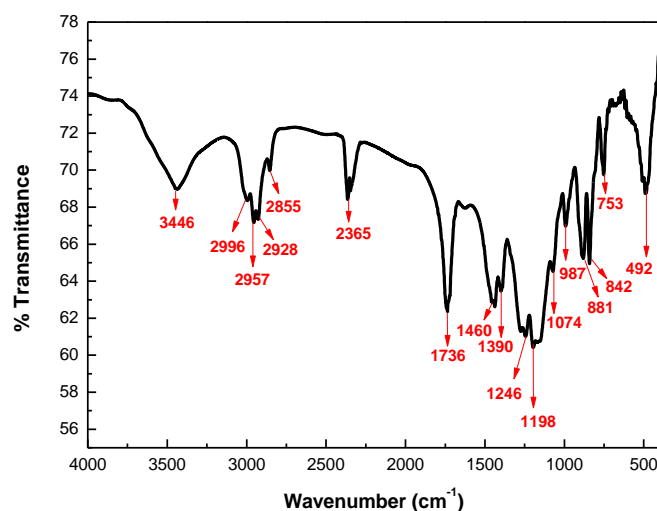


Figure 5.32 FTIR of cladding material of 1.0 mm POF.

It is observed from the figure that there is a broad absorption band at 3446 cm^{-1} , which is ascribed to the $-\text{OH}$ group stretching. The four bands at the wavenumber from 2855 cm^{-1} to 2996 cm^{-1} could be attributed to the $\text{C}-\text{H}$ bond stretching vibrations of the $-\text{CH}_3$ and $-\text{CH}_2-$ groups. The sharp and strong absorption band at 1736 cm^{-1} is due to the existence of the acrylate carboxyl group. The two continuous bands at 1460 and 1390 cm^{-1} are both assigned to the α -methyl group vibrations, which have another absorption band at 753 cm^{-1} . The next two peaks at 1246 cm^{-1} and 1198 cm^{-1} are ascribed to the presence of $\text{C}-\text{F}$ bond. The following weak

absorption band at 1074 cm^{-1} is attributed to the C–O bond. The visible absorption bands at the wavelengths of 881 cm^{-1} and 987 cm^{-1} belong to the –O–CH₃ group. The absorption bands at 842 cm^{-1} and 492 cm^{-1} are resulted from the –CH₂– groups. There is an evident absorption at 2365 cm^{-1} , which might be caused by the addition of carbon dioxide during the processes of sample preparation. It is confirmed that the cladding is made of PMMA and PTFE.

The mixture of PTFE into PMMA can change the properties of material. PTFE is a kind of soft polymers, its modulus is only 0.5 GPa but its strain reaches to 250 ~ 350 % [147]. The different ratio between core and cladding in POFs could lead to the unexpected results of mechanical properties. In a word, it is not easy to investigate the tension fatigue properties of POF with respect to the effect of fiber diameter on extension response.

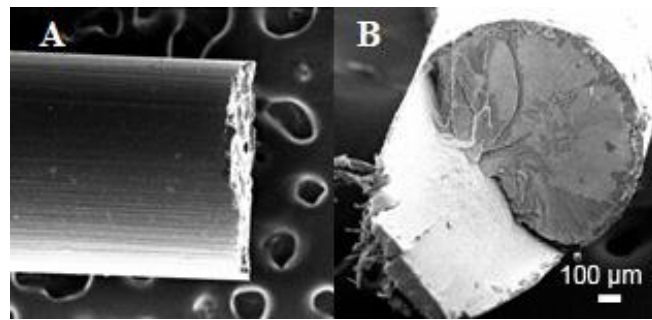


Figure 5.33 Fracture surfaces of 1.0 mm POF from tensile testing: (A) side view; (B) end view.

Moreover, it is noticed that the strain value decreases markedly to a balance state than the values of tensile strength and modulus for all POFs. The strain value is higher than metals but lower than a lot of polymers. POFs applied in this work are relatively brittle, as proved by the fracture images in SEM pictures in Figure 5.33, it is observed that 1.0 mm POF with comparatively smooth and flat fracture surfaces suffers less degradation in tensile properties and fails with less relaxation of damage progression. It implies that POFs present a high strain sensitivity in tensile testing after dynamic tension fatigue testing.

5.5 Flex fatigue properties

5.5.1 Bending resistance

The mean values of repeated bending cycles N to break of all POFs and the values of corresponding 95% confidence interval CI of mean, SD and CV are given in Table 5.4. It is observed that the fiber diameter plays a significant role in bending resistance of POF. The number of bending cycles to break of 0.25 mm POF is approximately 5 times higher than that of 0.5 mm POF and almost 22 times higher than that of 1.0 mm POF. The smaller the fiber diameter, the higher the bending cycles to break. The similar phenomenon could be also

discovered in other four parameters. It indicates that the thinner POF could display higher bending resistance under the same situation.

Table 5.4 Statistics description of number of bending cycles to break of all POFs.

d [mm]	N [cycles]	Lower 95% CI [cycles]	Higher 95% CI [cycles]	SD [cycles]	CV [%]
0.25	1699.46	1507.33	1891.59	676.04	39.78
0.4	1062.84	850.65	1275.03	746.64	70.25
0.5	301.47	248.05	354.89	181.95	60.36
0.75	124.15	111.36	136.93	44.02	35.46
1.0	73.46	67.23	79.68	20.96	28.53

Figures 5.34-5.43 illustrate the results in regard to the typical Q-Q plots and Weibull probability plots. It is visible that the combination of Q-Q plot and Weibull distribution can give a good fit to most of experimental data.

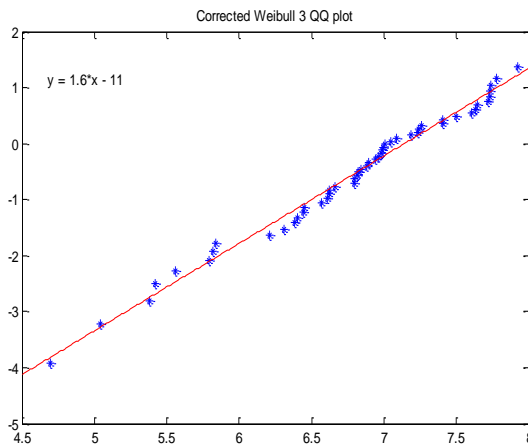


Figure 5.34 Q-Q plot of 0.25 mm POF.

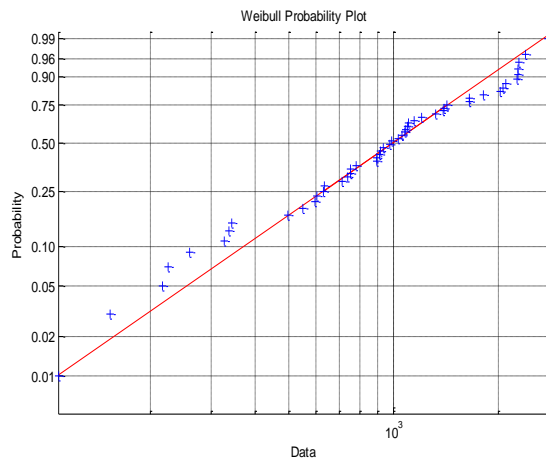


Figure 5.35 Weibull probability plot of 0.25 mm POF.

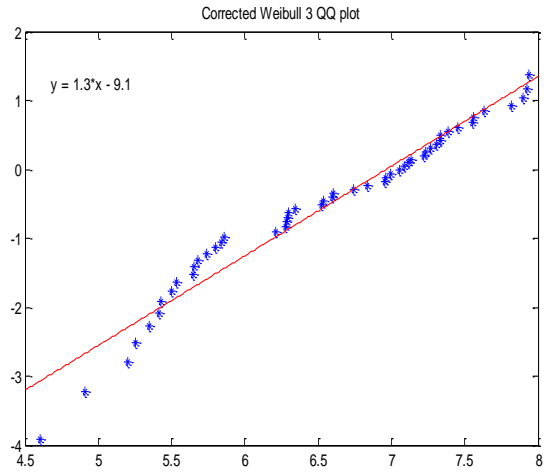


Figure 5.36 Q-Q plot of 0.4 mm POF.

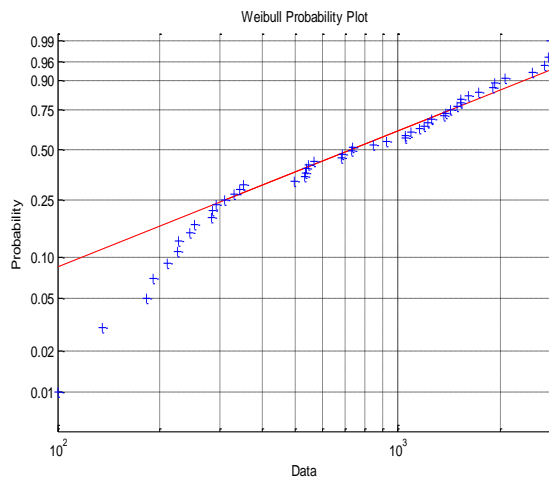


Figure 5.37 Weibull probability plot of 0.4 mm POF.

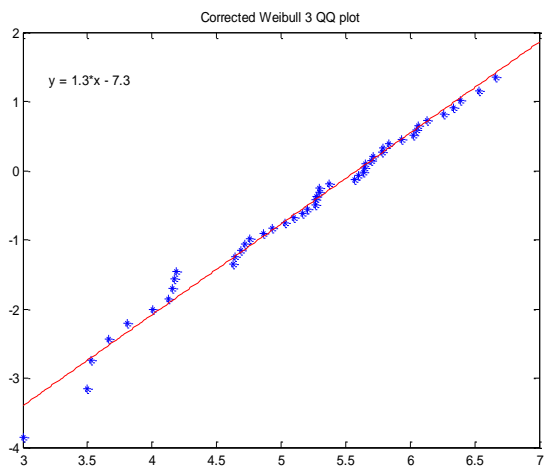


Figure 5.38 Q-Q plot of 0.5 mm POF.

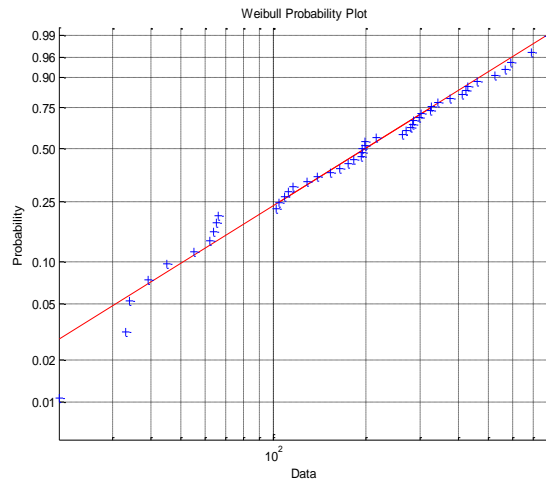


Figure 5.39 Weibull probability plot of 0.5 mm POF.

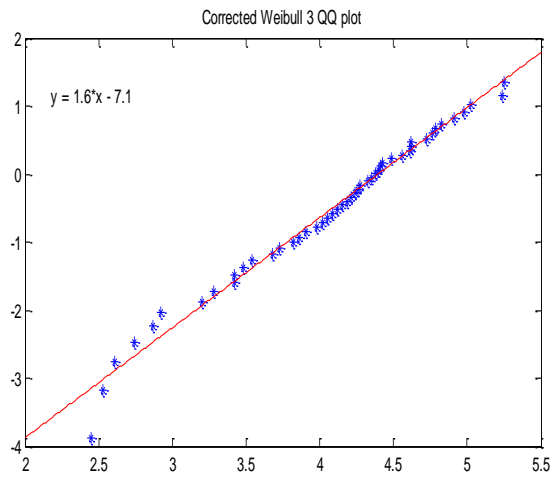


Figure 5.40 Q-Q plot of 0.75 mm POF.

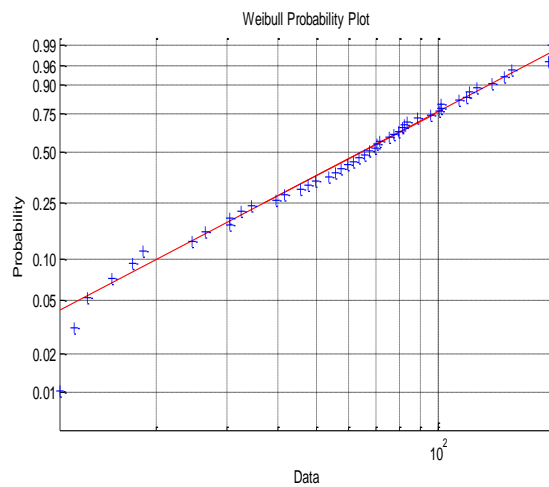


Figure 5.41 Weibull probability plot of 0.75 mm POF.

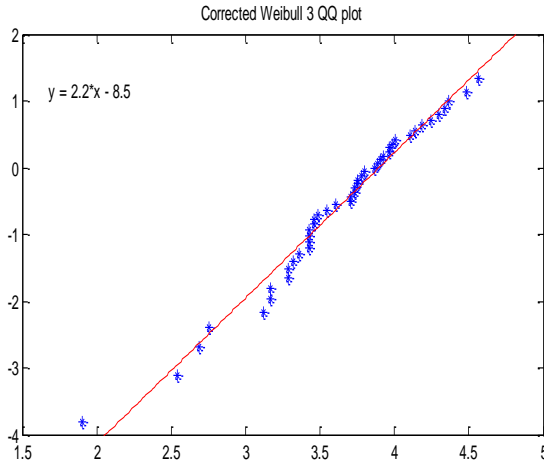


Figure 5.42 Q-Q plot of 1.0 mm POF.

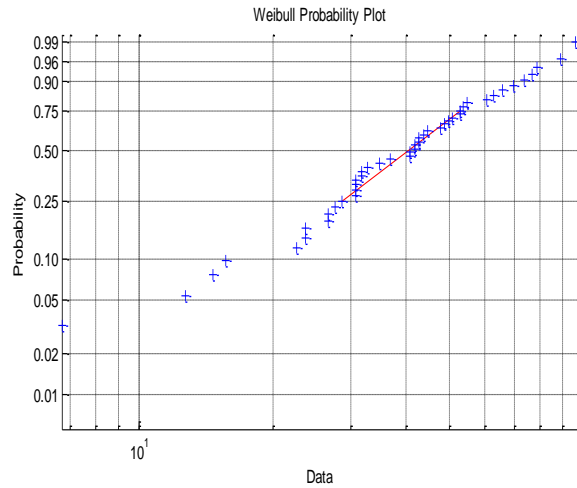


Figure 5.43 Weibull probability plot of 1.0 mm POF.

The three parameters of Weibull distribution are given in Table 5.5. Both W_1 and W_2 decrease dramatically with increasing fiber diameter, and W_3 changes in an opposite manner. W_1 is the shift parameter, which directly reflects the bending resistance of sample. In probability density function, W_2 represents the lateral data distribution and W_3 expresses the vertical data distribution. It implies that there is a relatively centralized distribution of experimental data for thick fiber. The variation in experimental data of number of bending cycles to break is smaller for thicker fiber. The reason behind it could be explained by the large variation of thickness of thin fiber, as given in Table 5.3. It indicates that it is much easier to control the uniformity of fiber with thicker diameter.

Based on the various evaluation methods of Weibull parameters introduced in section 3.44, the results of shift parameter are shown in Table 5.6. It is observed that there are evident differences among different methods. The values obtained from Equation (3.53), which are expressed as W_{14} , are extremely high. The values obtained from other methods are quite similar to each

other. The method based on the calculation with moments gives a slightly lower values with an exception with 1.0 mm POF. It indicates that the calculation results of Weibull parameters shown in Table 5.5 are feasible. Other methods except the last one could be also applied to estimate the Weibull parameters.

Table 5.5 Three parameters of Weibull distribution.

d [mm]	Weibull shift W_1 [cycles]	Weibull scale W_2 [cycles]	Weibull shape W_3 [-]
0.25	588.80	1244.64	1.69
0.4	93.01	1047.22	1.28
0.5	58.91	264.32	1.34
0.75	52.45	80.34	1.69
1.0	31.28	47.62	2.17

Table 5.6 Comparison of Weibull shift parameter according to various evaluation methods.

d [mm]	W_1 [cycles]	W_{10} [cycles]	W_{11} [cycles]	W_{12} [cycles]	W_{13} [cycles]	W_{14} [cycles]
0.25	588.80	698	622.56	765.33	697.21	2132.38
0.4	93.01	193	171.08	230.67	192.53	607.27
0.5	58.91	79	70.94	94.22	78.77	244.26
0.75	52.45	64	61.03	65.29	63.99	193.05
1	31.28	29	15.28	53.21	27.99	92.82

Table 5.7 Logarithmic values of number of bending cycles to break and flexibility of POFs.

d [mm]	E [GPa]	N [cycles]	F_l [N ⁻¹ mm ⁻²]	$\log(d)$	$\log(N)$	$\log(F_l)$
0.25	2.425	1699.46	2.150	-0.602	3.230	0.332
0.4	2.500	1062.84	0.318	-0.398	3.026	-0.498
0.5	3.116	301.47	0.105	-0.301	2.479	-0.979
0.75	3.140	124.15	0.021	-0.125	2.094	-1.678
1	3.185	73.46	0.006	0	1.866	-2.221

Table 5.7 shows the values of number of bending cycles to break and flexibility which is calculated with the modulus from tensile testing according to Equation (4.2) and the corresponding logarithmic values. When the diameter increases, the number of bending cycles to break and the flexibility decrease markedly, especially the value of flexibility with a descent from 2.150 to 0.006 N⁻¹mm⁻². Figure 5.44 illustrates the relation between fiber diameter and

flexibility, as well as the relation between number of bending cycles to break and flexibility. The two linear fitting curves in this figure match well with the experimental data, and are expressed as:

$$\log(d) = 0.24 \times \log(F_l) \quad (5.3)$$

$$\log(N) = 0.57 \times \log(F_l) + 3.12 \quad (5.4)$$

Which indicates the positive relationship between number of bending cycles to fiber failure and flexibility of POF.

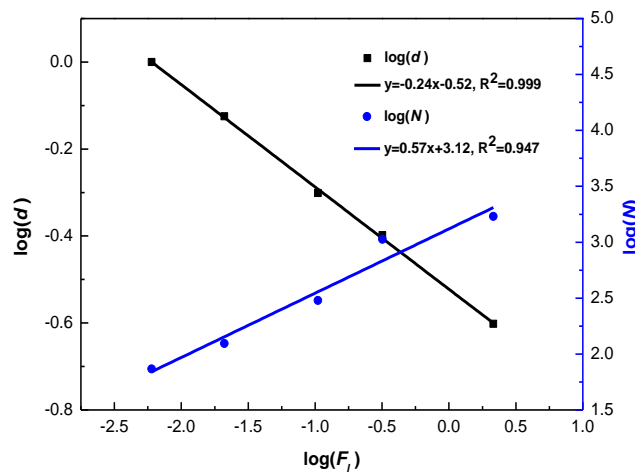


Figure 5.44 Dependences of $\log(d)$ and $\log(N)$ on $\log(F_l)$.

5.5.2 Flex fatigue behavior

Flex fatigue life curve

According to Equation (4.3), the pretension that is applied on the free end of POF is dependent on the ultimate tensile strength. The mean stress-strain curve of 0.25 POF based on the tensile results from section 5.1 is shown in Figure 5.45. The black solid line represents the mean values of experimental data. This line terminates at the first breakage of fiber. The black dash line is a straight line that connects the terminated point and the point in terms of mean values of both tensile strength and strain on the right side. Two red solid lines illustrate the borders of lower and higher 95% *CI* of mean.

The mean values of number of bending cycles at break of 0.25 mm POF with different pretensions are calculated in Table 5.8, as well as the values of *SD* and *CV*. Based on the data in Table 5.8, the fatigue life curve of 0.25 mm POF is drawn in Figure 5.46.

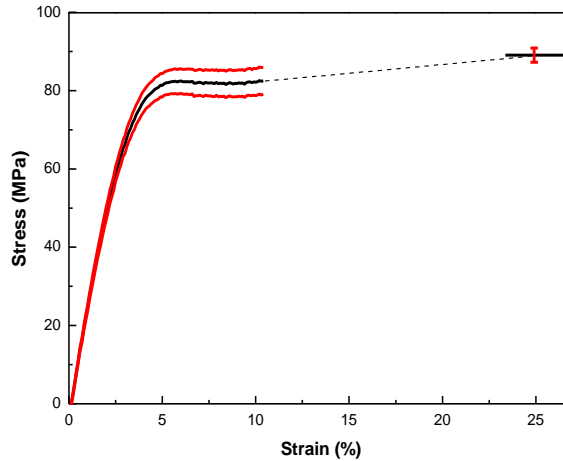


Figure 5.45 Mean curve of stress versus strain of 0.25 mm POF.

Table 5.8 Number of bending cycles at break of 0.25 mm POF.

a_c [%]	Applied stress σ [MPa]	N [cycles]	SD [cycles]	CV [%]
93.33	83.84	2.36	1.21	51.19
88.89	79.85	62.14	4.41	36.34
77.78	69.87	132.58	13.81	42.39
66.67	59.86	224.18	22.15	29.86
55.56	49.9	359.38	75.56	47.41
44.44	39.92	571.32	115.38	35.91
33.33	29.94	1077.96	437.21	40.56
22.22	19.96	1363.54	575.45	42.20
11.11	9.98	1648.08	701.61	42.57
5.55	4.99	1859.46	733.45	39.44
2.22	2	9843.21	2314.78	38.56
1.11	1	16165.7	6153.4	38.14
0.44	0.4	23452.11	8342.32	39.67

There is a significant difference between the mean values of number of bending cycles when the values of a_c are 2.22% and 5.55%. The phenomenon might be explained by the movements of molecular chains. It is well known that, under certain load, the molecular chains are firstly orientated and rearranged; during this period the fiber is stretched straight without any extension. Then the short chains are drawn out from amorphous region. The applied force is undertaken on the long chains until they are broken. Below the value of a_c at 5.55%, 0.25 mm POF might be oriented, resulting in the high flex fatigue resistance to small temporary load. Above this critical value, there is an obvious reduced flex fatigue resistance to larger temporary

load. The similar phenomena are found with the value of 88.89%. Especially when a_c is 93.33%, the bending cycle is only 2.36 with relatively weak flex fatigue resistance.

Usually, the ratio of elaborated fatigue strength to ultimate tensile strength for textile materials varies from 50% to 98%. While in this investigation, the ratio range is boarder. One major reason is attributed to the properties of POF itself. On the other hand, the testing conditions especially the bending angle and the bending speed might affect the results as well. The POFs produced for efficient data transmission generally have the limitation of flexibility, and the bending radius is only eight times of fiber diameter, as shown in Table 4.1. The large bending angle and fast bending speed could initiate easy destruction of POF due to the limited resistance to flex fatigue.

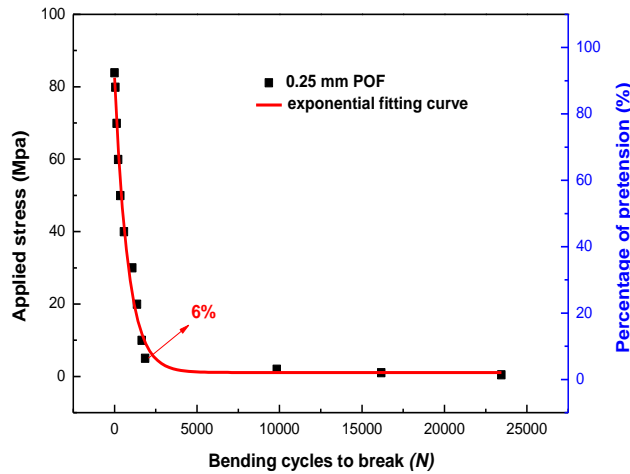


Figure 5.46 $S-N$ curve for 0.25 mm POF.

It is visible from the fatigue life curve of 0.25 mm POF that there is a negative relationship between flex fatigue characteristic and applied stress or a_c . The empirical equation of $S-N$ curve based on the corresponding exponential fitting is given as follows,

$$y = 81.66 \times \exp\left(-\frac{x}{813.29}\right) + 5.44 \quad (5.5)$$

The SEM images in Figure 5.47 represent the morphology of bending fracture of 0.25 mm POF in flex fatigue texting. It is observed that there is an obvious plastic deformation on the fracture surface, which is uneven and sloping down from the stretched side (left side) to the compressed side (right side).

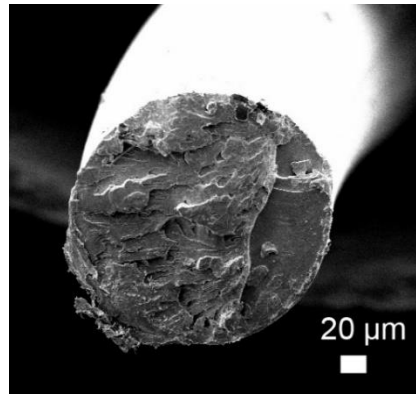


Figure 5.47 Bending fracture of 0.25 mm POF under the pretension of 10% of ultimate tensile strength.

Fatigue sensitivity coefficient

The experimental result of fatigue sensitivity coefficient in this work is markedly different, b equals 0.297 for 0.25 mm POF, as shown in Figure 5.48. It could be explained by the high bending angle or bend speed. The number of bending cycles to break is higher with smaller bending angle or bend speed. Therefore, POE is assumed to be more sensitive to flex fatigue with large bending angle or fast bending speed. The core/cladding structure of POE, the variance of core/cladding thickness ratio and the evenness of cladding could also influence the experimental results unexpectedly. In order to understand better, the tensile testing of samples after flex fatigue testing before fiber fracture was also investigated.

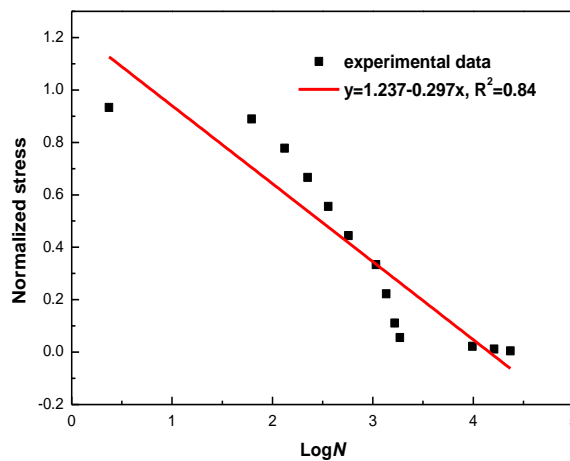


Figure 5.48 Normalized $S-N$ curve for 0.25 mm POE.

Stiffness after flex fatigue testing

Some samples were taken out from the Flexometer device during the flex fatigue experiments without fiber fracture, in order to investigate the stiffness of 0.25 mm POF. It is evident from Figure 5.49 that, when the pretension is below the upper limit of transition zone which is around 22.22% of ultimate tensile strength, there is no significant modulus degradation with the increase in bending cycles from 10 up to 1000. However, the modulus after flex fatigue testing with 10 bending cycles is less than 5% of the modulus calculated in section 5.1, which means there is an evident loss of modulus during 10 bending cycles. It implies that 0.25 mm POF is very sensitive to flex fatigue.

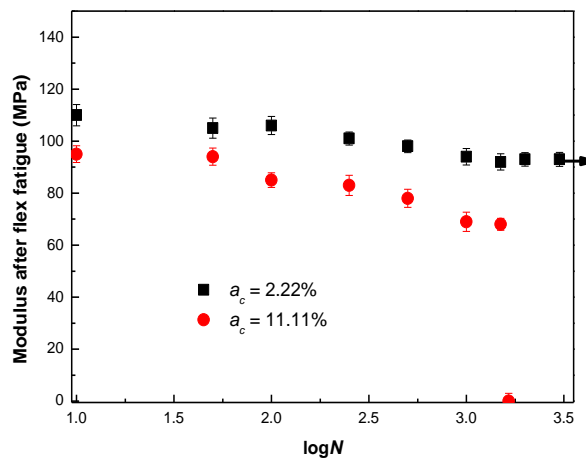


Figure 5.49 Modulus of 0.25 mm POF after flex fatigue testing.

This phenomenon is quite distinct from that of hemp fiber or glass fiber reinforced composites [148]. The bending conditions (bending angle and bending speed) might have an unpredicted influence on POF stiffness, or have a greater impact on POF stiffness than bending cycles in present work. The bending angle and bending speed should be taken into account and studied further.

Chapter 6 Conclusion and Outlook

6.1 Conclusion from experiments

It is summarized from the tensile testing that the widely accepted concept about the inverse relation between diameter and tensile strength of single fiber, the weakest-link theory, also conforms to the results of POFs. The strain value of POF decreases with increase in fiber diameter due to the same crosshead speed and high deformation ability of thin fiber. The modulus rises as the fiber diameter goes up, which is not constant as an intrinsic property. It is attributed to the calculation method of modulus dependent on the dissimilar changes of strength and strain.

From the investigation of strength distribution of POF, it is concluded that the value of tensile strength declines with the increment of gauge length, which could be also explained by the weakest-link theory. The similar phenomenon is also found in the strain value since the same crosshead speed and various gauge lengths result in the different extension rates. The value of modulus is dependent on both strength and strain and varies in the similar manner as fiber diameter. The effect of gauge length on tensile properties might be influenced by the probably visco-plastic properties and interphase properties between core and cladding. In addition, the results also imply that three-parameter Weibull distribution could be a good model not only for investigation of statistical distribution of fiber strength, but also for estimation of the relation between mean fiber strength and gauge length.

The application of nanoindentation technique in the investigation of local mechanical properties of POF core and POF cladding indicates that there are normal tendencies of the relations between loading/holding condition and nanoindentation creep properties. With the increase in loading rate or holding time, the nanoindentation creep deformation goes up accordingly. On the other hand, 0.5 mm POF has a stronger loading time sensitivity in nanoindentation than holding time sensitivity. Meanwhile, it is observed that POF cladding is softer than POF core, which is particularly obvious in the results at various loading time. It is surprising to find that both fiber diameter and cross section direction have influences on hardness properties even though the hardness is assumed to be constant with the same material. The reason behind it could be mainly attributed to the different surface roughness of each sample and the limited number of measurement. The investigation of interphase properties of 0.5 mm POF by nanoindentation method implies that the small nanoindentation depth is expected to give a relatively effective interphase width and the interphase width is estimated to be in the range of 800 ~ 1600 nm roughly, which is still a wide range. To obtain effective interphase properties, the method to obtain finer surface should be developed. Other techniques such as nanoscratch testing might be also employed to figure out the local mechanical properties and interphase properties of POF [99, 149].

The durability of POF is investigated based on tension fatigue testing and flex fatigue testing. The results from tension fatigue testing indicate that the values of total extension and cyclic extension respond to fatigue cycles in the similar way. Both values go up with increasing fatigue cycles. During tension fatigue testing with the same external stress amplitude, if the unloading time is not sufficient for elastic deformation to recover completely or the viscous deformation occurs, the total extension at each stress peak and the cyclic extension in each loading period would accumulate gradually. In addition, both values are affected by the fiber diameter. It is observed that 0.5 mm POF has higher total extension but lower cyclic extension than thicker POFs. The loading/unloading time for all POFs is the same, while the applied stress is different, therefore, the loading/unloading rate for each POF is various. There is longer time for thin POF to deform, leading to the larger total extension consequently. Due to the presence of probably greater proportion of viscous deformation in the whole deformation, the thinner POF induces lower cyclic value. Furthermore, the tensile testing after tension fatigue testing indicates that POFs present significant losses in tensile properties in terms of values of tensile strength, modulus and strain. The thicker the fiber, the larger the losses.

The flex fatigue properties of POF can be characterized with the mean number of bending cycles to break by Flexometer. Based on the results from flex fatigue testing, it is found that the combination of Q-Q plot and three-parameter Weibull distribution is effective for estimation of number of bending cycles to break with different POF diameters. Additionally, there is a positive relationship between number of bending cycles to break and flexibility of POF.

The flex fatigue life curve illustrates the decay exponential relation between applied pretension and flex fatigue life time, which are expressed by the percentage of ultimate tensile strength of POF and the number of bending cycles at break, respectively. The flex fatigue resistance of POF increases with decreasing pretension. In the meantime, the ratio of pretension to ultimate tensile strength of POF varies in a broader range than the common value (50% ~ 90%) of textile materials, and the fatigue sensitivity coefficient of POF is higher than the common value (0.1) of other materials. It is explained mainly by the POF properties and the extensive bending angle or fast bending speed. Compared with the modulus before flex fatigue testing, there is an evident degradation in modulus after flex fatigue testing even though the pretension is below the transition zone in the fatigue life curve. However, the modulus decreases slightly after 10 bending cycles. The variance of modulus after flex fatigue testing indicates that POF is sensitive to bend.

In sum up, POF, as a new material introduced in textile applications, is relatively thick, stiff, brittle and sensitive to bend. Besides, POF consists of a core/cladding structure. Due to these aspects, it is difficult to integrate POFs into fabrics. The basic research on mechanical properties of POF needs more attention and contributions.

6.2 Other findings

POF was initially developed for application in data communication. The present applications extend to a lot of fields. In textile field, the side illumination of luminous fabrics could be accomplished by macro bends of POF in structure design and the surface modification of POF. Another two methods are introduced here to enhance the side illumination of POF fabrics.

6.2.1 Fluorescent fabrics

The side illuminating effect of POF is improved by using the woven fluorescent polyester (PET) fabrics which are wrapped on the surface of naked POF, as shown in Figure 6.1. The left part is the integration of POF and fabric, the right part is only fabric which can be stitched/sewn into textiles like clothes and carpets.

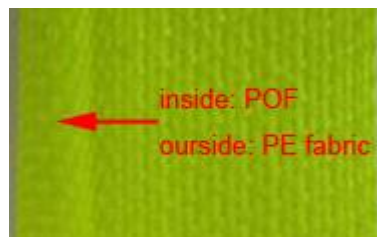


Figure 6.1 Sample of 3 mm POF wrapped with fluorescent PET fabrics.

This idea is based on the emission principle of phosphors. The fluorescent fabric first stores the energy from the light source and then releases slowly. When POF wrapped with fluorescent fabric is connected to the light source continuously, the measured side illumination intensity from the surface of sample increases accordingly, as illustrated in Figure 6.2. Moreover, this method could be also applied to even the light diffusion on the surface of sample.

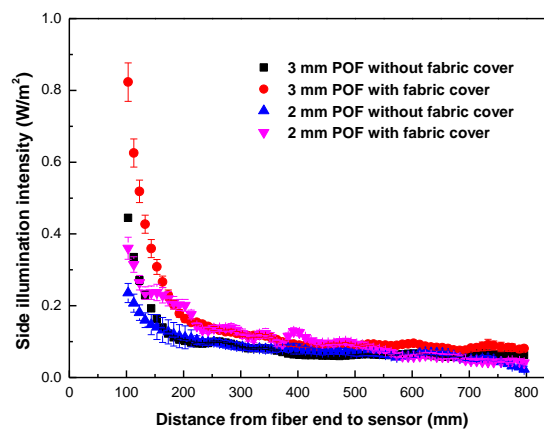


Figure 6.2 Comparison of side illumination intensity of POFs with and without fluorescent PET fabric.

6.2.2 Lensed POF

The side illumination intensity of POF could be also enhanced by the lensed end shape, which could be created by the method of CO₂ laser cutting, as shown in Figure 6.3. Based on the adjustment of the mark speed of laser treatment and the rotation speed of holding device of POF, different lens shapes could be obtained accordingly.

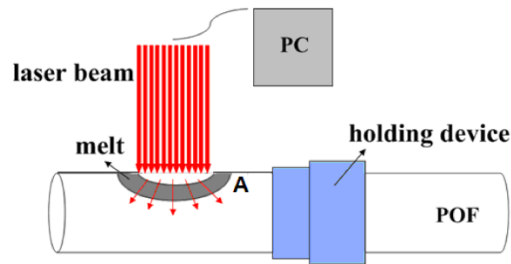


Figure 6.3 Scheme of CO₂ laser cutting.

The perfect ball lens in the end of POF could be achieved, as shown in Figure 6.4. The lensed POF can be used as a convex to receive light for light gathering purpose, or applied as a concave to release light for light distribution purpose.

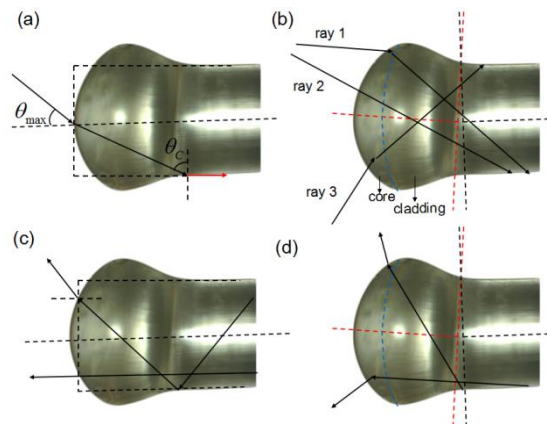


Figure 6.4 Lensed POF: (a) light gathering; (b) light distribution.

6.3 Future work

In the research of POF fabrics, a lot of efforts have been made to obtain luminous fabrics with various pattern designs. There are two major contributions, one is to improve the side illumination of POF fabrics, and another is to develop the manufacturing techniques of luminous fabric with certain patterns. Less research work focuses on the basic investigations about how POFs behave in POF fabrics with respect to flexibility, drapability and durability. This thesis work provides some basic understanding about POF itself, but there are still some confusions left.

In the near future, we will go further with the mechanical properties of POF, mainly regarding the diameter effect on the mechanical properties, the interphase behavior between core and cladding and the fracture mechanism. Additionally, the POF fabrics with dynamic patterns will be developed, and the corresponding mechanical properties in terms of flexibility, drapability and durability will be taken into account on the whole.

Chapter 7 References

1. W. Sturgeon, *Improved Electro Magnetic Apparatus*. Trans. Royal Society of Arts, Manufactures, & Commerce (London) 1825. **43**: p. 37-52.
2. M. Windelspecht, *Groundbreaking Scientific Experiments, Inventions, and Discoveries of the 19th Century, XXII*. 2003: Greenwood Publishing Group.
3. P. Horace, *Processing of Wire from Antiquity to the Future*. Wire Journal International, 2008: p. 58-66.
4. https://en.wikipedia.org/wiki/Optical_fiber
5. C. Brochier and A. A. Lysenko, *Optical Fiber Fabrics*. Fibre Chemistry, 2008. **40**(4): p. 303-307.
6. A. M. Glass, D. J. DiGiovanni, et al., *Advances in Fiber Optics*. Bell Labs Technical Journal, 2000. **5**: p. 168-187.
7. Y. Koike, E. Nihei, et al., *Graded-Index Plastic Optical Fiber Composed of Methyl Methacrylate and Vinyl Phenylacetate Copolymers*. Applied Optics, 1990. **29**(18): p. 2686-2691.
8. Y. Koike. *Progress of Plastic Optical Fiber Technology*. in *22nd European Conference on Optical Communication* 1996.
9. J. Cirillo, *High Speed Plastic Networks (HSPN): A New Technology for Today's Applications*, in *Aerospace and Electronic Systems Magazine, IEEE*. 1996.
10. E. Nihei, T. Ishigure, et al., *Present Prospect of Graded-Index Plastic Optical Fiber in Telecommunication*. IEICE-Transactions on Electronics, 1997. **E80-C**(1): p. 117-122.
11. H. Murofushi. *Low Loss Perfluorinated POF*. in *Proceeding of Fifth International Conference on Plastic Optical Fibres and Applications-POF'96*. 1996. Paris.
12. S. Kinoshita and S. Yoshioka, *Structural Colors in Nature: The Role of Regularity and Irregularity in the Structure*. ChemPhysChem, 2005. **6**: p. 1442-1459.
13. D. Graham-Rowe, *Photonic Fabrics Take Shape*. Nature Photonics, 2007. **1**: p. 6-7.
14. A. Harlin, M. Mailis, et al., *Development of Polymeric Optical Fibre Fabrics as Illumination Elements and Textile Displays*. Autex Research Journal, 2003. **3**: p. 1-8.
15. E. Thiele and R. Arnold, *Gewirkte Lichtnetze-Ein Leuchtendes Beispiel Textiler Innovation*. Kettenwirk-Praxis, 2003. **37**: p. 24-26.
16. D. Kremenáková, V. Lédl, et al., *Active illuminating safety product*, P. o. CZ, Editor. 2013: Czech Republic.

17. J. M. Chua, *Fiber-Optic Heels by Francesca Castagnacci are Sophisticated, Illuminating*, in *Eco-Friendly Shoes, Featured, Wearable Technology, Women's Eco-Fashion*. 2007.
18. M. Daniel, *Light Emitting Fabric*. 1980: United States.
19. K. D. Kaschke, *Optical Fiber Light Emitting Apparatus*. 1996: United States.
20. E. Deflin, V. Koncar, et al. *Bright optical fiber fabric*. in *6th Asian Textile Conference*. 2001. Hong Kong.
21. A. Harlin, H. Myllymaki, et al., *Polymeric Optical Fibres and Future Prospects in Textile Integration*. *Autex Research Journal*, 2002. **2**: p. 132-143.
22. A. F. Abouraddy, M. Bayindir, et al., *Towards Multimaterial Multifunctional Fibres That See, Hear, Sense Communicate*. *Nature Materials*, 2007. **6**: p. 336-347.
23. T. A. C. Flipsen, A. J. Pennings, et al., *Polymer Optical Fiber with High Thermal Stability and Low Optical Losses Based on Novel Densely Crosslinked Polycarbosiloxanes*. *Journal of Applied Polymer Science*, 1998. **67**: p. 2223-2230.
24. M. Rothmaier, M. P. Luong, et al., *Textile Pressure Sensor Made of Flexible Plastic Optical Fibers*. *Sensors*, 2008. **8**: p. 4318-4329.
25. B. Selm, M. Rothmaier, et al., *Novel Flexible Light Diffuser and Irradiation Properties for Photodynamic Therapy*. *Journal of Biomedical Optics*, 2007. **12**: p. 1-7.
26. <http://www.photofrin.com/pdf/patientguide.pdf>
27. S. Mordon, C. Cochrane, et al., *Innovative Engineering Design of A Textile Light Diffuser for Photodynamic Therapy*. *Photodiagnosis and Photodynamic Therapy*, 2011. **8**(2): p. 142-143.
28. M. A. El-Sherif, J. M. Yuan, et al., *Fiber Optic Sensors and Smart Fabrics*. *Journal of Intelligent Material Systems and Structures*, 2000. **11**: p. 407-414.
29. M. Rothmaier, B. Selm, et al., *Photonic Textiles for Pulse Oximetry*. *Optics Express*, 2008. **16**(17): p. 12973-12986.
30. B. Selm, E. A. Gürel, et al., *Polymeric Optical Fiber Fabrics for Illumination and Sensorial Applications in Textiles*. *Journal of Intelligent Material Systems and Structures*, 2010. **21**: p. 1061-1071.
31. M. Krehel, R. M. Rossi, et al., *Characterization of Flexible Copolymer Optical Fibers for Force Sensing Applications*. *Sensors*, 2013. **13**(9): p. 11956-11968.
32. D. Q. Ying, X. M. Tao, et al., *Fabric Strain Sensor Integrated with Looped Polymeric Optical Fiber with Large Angled V-Shaped Notches*. *Smart Material Structure*, 2013. **22**(1): p. 1-10.

33. M. Krehel, M. Schmid, et al., *An Optical Fibre-Based Sensor for Respiratory Monitoring*. *Sensors*, 2014. **14**: p. 13088-13101.
34. D. Morrisa, S. Coyle, et al., *Bio-Sensing Textile based Patch with Integrated Optical Detection System for Sweat Monitoring*. *Sensors and Actuators B*, 2009. **139**(1): p. 231-236.
35. J. Witt, M. Schukar, et al., *Medicinal Textiles with Integrated Polymer-Optical Fibers for Respiration Monitoring*. *Tm-Technisches Messen*, 2008. **75**: p. 670-677.
36. A. Appajaiiah, *Climatic Stability of Polymer Optical Fibers (POF)*, in *Faculty of Mathematics and Natural Sciences*. 2004, The University of Potsdam
37. Y. Koike and R. Nihei, *Method of Manufacturing Plastic Optical Transmission Medium*. 1997: United States.
38. Q. Mao, *Plastic Optical Fiber and Its Application Prospect (In Chinese)*, in *Communications Technology and Standards (Expert Forum)*. 2010: China.
39. M. H. Im, E. J. Park, et al., *Modification of Plastic Optical Fiber for Side-Illumination*. *Human-Computer Interaction*, 2007. **4551**: p. 1123-1129.
40. J. Spigulis, D. Pfafrods, et al., *The "Glowing" Optical Fibre Designs and Parameters*. *Proceedings of SPIE*, 1996. **2967**: p. 231-236.
41. M. Zajkowski, *Emission of Flux Light in 'Side Light' Fiber Optic*. *Proceedings of SPIE*, 2003. **5125**: p. 322-327.
42. J. Shen, X. M. Tao, et al., *Light-Emitting Fabrics Integrated with Structured Polymer Optical Fibers Treated with an Infrared CO₂ Laser*. *Textile Research Journal*, 2012. **0**: p. 1-10.
43. W. Daum, J. Krauser, et al., *POF-Polymer Optical Fibers for Data Communication*. 2002, Berlin Heidelberg: Springer.
44. C. Emslie, *Review Polymer Optical Fibers*. *Journal of Materials Science*, 1988. **23**: p. 2281–2293.
45. T. Kaino, *Polymer Optical Fibers-Polymers for Lightwave and Integrated Optics*, ed. L. A. Hornak. 1992, New York: Marcel Dekker, Inc.
46. J. Zubia and J. Arrue, *Plastic Optical Fibers: An Introduction to Their Technological Processes and Applications*. *Optical Fiber Technology*, 2001. **7**: p. 101-140.
47. A. Weinert, *Plastic Optical Fibers: Principles, Components, Installations*. 1999: Publicis MCD Verlag.
48. [https://en.wikipedia.org/wiki/Poly\(methyl_methacrylate\)](https://en.wikipedia.org/wiki/Poly(methyl_methacrylate))
49. <https://en.wikipedia.org/wiki/Polystyren>

50. <https://en.wikipedia.org/wiki/Polycarbonate>
51. A. Rousseau, B. Boutevin, et al. *Synthesis of Low Absorption Halogenated Polymers for POF in Plastic Optical Fibres and Applications Conference*. 1992. pARIS.
52. M. Beckers, T. Schlüter, et al., *An Innovative Extrusion Technology for the Melt Spinning of Polymer Optical Fibers Used for Light Transmission over Short Distances*. International Fiber Journal 2014. **28**(2): p. 8-10.
53. O. Ziemann, J. Krauser, et al., *POF Handbook: Optical Short Range Transmission Systems (2nd)*. 2008, Berlin: Springer.
54. J. Marcou, *Plastic optical fibres: Practical applications*. 1997, Chichester: Wiley.
55. J. P. Harmon and G. K. Noren, *Optical Polymers-Fibers and Waveguides*. ACS Symposium Series (Book 795). 2001, Washington DC: American Chemical Society.
56. H. S. Nalwa, *Polymer Optical Fibers*. 2004, Valencia, California: American Scientific Publishers.
57. M. G. Kuzyk, *Polymer Fiber Optics-Materials, Physics, and Applications*. Optical Science and Engineering 2007, Boca Raton, Florida: Taylor & Francis.
58. S. Schrader, *Materials for Optical Polymer Fibers and Their Preparation (In German)*, in *Opt-61 Polymer Optical Fibers: Production and Use*, A. Schlachetzkie, K. Dorenwendt, et al., Editors. 1999: Bremerhaven. p. 3-56.
59. A. Weinert, *Plastic Fiber Optic Fundamentals, Components, Installation (In German)*. 1998, Erlangen, Munich: Publicis MCD Verlag.
60. B. Harris, *Fatigue Behavior of Polymer-Based Composites and Life Prediction Methods*, in *Durability Analysis of Structural Composite Systems: Reliability, Risk and Prediction of Safe Residual Integrity*, A. H. Cardon, Editor. 1995. p. 49-84.
61. T. Ishigure, E. Nihei, et al., *Graded-Index Polymer Optical Fiber for High-Speed Data Communication*. Applied Optics, 1994. **33**: p. 4261-4266.
62. T. Nonaka, T. Hosoya, et al., *Plastic Optical Fiber Preform, and Process and Apparatus for Producing the Same*. 1998: United States.
63. B. C. Ho, J. H. Chen, et al., *Method of Making Graded Refractive Index Polymeric Optical Fibers and Optical Fibers Made by the Method*. 1996: United States.
64. T. Yamamoto, Y. Mishina, et al., *Optical Transmission Medium and Process for Producing the Same Based on Vinylidene Fluoride Polymers and Methacrylate Polymers*. 1989: United States.
65. M. Beckers, T. Gries, et al. *Continuous Manufacturing Processes for Graded Index Polymer Fibers in Communication Cable Networks with the Exhibition (in German)*. in *International Trumpet Guild Conference 2013*. Berlin: VDE-Verlag.

66. M. Beckers, T. Schlüter, et al., *An Overview on Fabrication Methods for Polymeric Optical Fibers*. Polymer International, 2015. **64**(1): p. 25-36.
67. https://en.wikipedia.org/wiki/Fatigue_%28material%29
68. J. B. Pethica, R. Hutchings, et al., *Hardness Measurement at Penetration Depths as Small as 20 nm*. Philosophical Magazine A, 1983. **48**(4): p. 593-606
69. W. C. Oliver, *Progress in the Development of a Mechanical Properties Microprobe*. MRS Bulletin, 1986. **11**: p. 15-21.
70. M. F. Doerner and W. D. Nix, *A Method for Interpreting the Data from Depth-Sensing Indentation Instruments*. Journal of Material Research, 1986. **1**: p. 601-609.
71. J. B. Pethica, *Microhardness Tests with Penetration Depths Less Than the Ion-Implanted Layer Thickness*, in *Ion implantation into Metals*, V. Ashworth, W. Grant, et al., Editors. 1982, Pergamon Press: Oxford. p. 147-156.
72. J. L. Loubet, J. M. Georges, et al., *Vickers Indentation Curves of Magnesium Oxide (MgO)*. Journal of Tribology, 1984. **106**(1): p. 43-48.
73. D. Newey, M. A. Wilkens, et al., *An Ultra-Low-Load Penetration Hardness Tester*. Journal of Physics E: Scientific Instruments, 1982. **15**(1): p. 119-122.
74. D. Stone, W. R. LaFontaine, et al., *An Investigation of Hardness and Adhesion of Sputter-Deposited Aluminum on Silicon by Utilizing a Continuous Indentation Test*. Journal of Materials Research, 1988. **3**(1): p. 141-147.
75. J. J. Gilman, *Hardness-a Strength Microprobe*, in *The Science of Hardness Testing and Its Research Applications*, J. H. Westbrook and H. Conrad, Editors. 1973, American Society for Metals. p. 51-74.
76. W. C. Oliver, C. J. McHargue, et al., *Thin Film Characterization Using a Mechanical Properties Microprobe*. Thin Solid Films, 1987. **153**: p. 185-196.
77. W. C. Oliver and G. M. Pharr, *An Improved Technique for Determine Hardness and Elastic Modulus using Load and Displacement Sensitive Indentation Experiments*. Journal of Materials Research, 1992. **7**(6): p. 1564-1583.
78. H. Hertz, *Über die Berührung fester elastischer Körper (in German)*. Journal für die Reine und Angewandte Mathematik, 1881. **92**: p. 156-171.
79. J. Boussinesq, *Potential Applications in Balance and Motion of Elastic Solids (in French)*. 1885, Paris: Gauthier-Villars.
80. A. E. H. Love, *Stress Produced in a Semi-Infinite Solid by Pressure on Part of the Boundary*. Philosophical Transactions of the Royal Society A, 1929. **228**: p. 377-420.
81. A. E. H. Love, *Boussinesq's Problem for a Rigid Cone*. Quarterly Journal of Mathematics, 1939. **10**(1): p. 161-175.

82. I. N. Sneddon, *The Relation Between Load and Penetration in the Axisymmetric Boussinesq Problem for a Punch of Arbitrary Profile*. International Journal of Engineering Science, 1965. **3**(1): p. 47-57.
83. J. W. Hardinga and I. N. Sneddon, *The Elastic Stresses Produced by the Indentation of the Plane Surface of a Semi-Infinite Elastic Solid by a Rigid Punch*. Mathematical Proceedings of the Cambridge Philosophical Society, 1945. **41**(1): p. 16-26.
84. D. Tabor, *A Simple Theory of Static and Dynamic Hardness*. Proceedings of the Royal Society A, 1948. **192**: p. 247-274.
85. N. A. Stillwell and D. Tabor, *Elastic Recovery of Conical Indentations*. Proceedings of the Physical Society 1961. **78**: p. 169.
86. A. P. Ternovskii, V. P. Alekhin, et al., *Micromechanical Testing of Materials by Depression*. Zavodskaya Laboratoriya, 1973. **39**: p. 1620-1624.
87. S. I. Bulychev, V. P. Alekhin, et al., *Mechanical Properties of Materials Studied from Kinetic Diagrams of Load versus Depth of Impression during Microimpression*. Strength of Materials, 1976. **8**(9): p. 1084-1089.
88. M. K. Shorshorov, S. I. Bulychev, et al., *Work of Plastic and Elastic Deformation during Indenter Indentation*. Soviet Physics Doklady, 1982. **26**: p. 769.
89. G. M. Pharr, W. C. Oliver, et al., *On the Generality of the Relationship among Contact Stiffness, Contact Area, and Elastic Modulus during Indentation*. Journal of Materials Research, 1992. **7**(3): p. 613-617.
90. W. C. Oliver and G. M. Pharr, *Measurement of Hardness and Elastic Modulus by Instrumented Indentation: Advances in Understanding and Refinements to Methodology*. Journal of Materials Research, 2004. **19**(1): p. 3-20.
91. G. M. Pharr and A. Bolshakov, *Understanding Nanoindentation Unloading Curves*. Journal of Materials Research, 2002. **17**: p. 2660-2671.
92. Z. S. Ma, S. G. Long, et al., *Loading Rate Sensitivity of Nanoindentation Creep in Polycrystalline Ni Films*. Journal of Materials Science, 2008. **43**: p. 5952-5954.
93. Y. I. Golovin, Y. L. Iunin, et al., *Strain-Rate Sensitivity of the Hardness of Crystalline Materials under Dynamic Nanoindentation*. Doklady Physics, 2003. **48**(9): p. 505-508.
94. B. J. Briscoe, L. Fiori, et al., *Nano-Indentation of Polymeric Surfaces*. Journal of Physics D: Applied Physics, 1998. **31**: p. 2395-2405.
95. J. J. Pang, M. J. Tan, et al., *Nanoindentation study of size effect and loading rate effect on mechanical properties of a thin film metallic glass Cu_{49.3}Zr_{50.7}*. Physica B: Condensed Matter, 2012. **407**(3): p. 340-346.
96. B. J. Briscoe and K. S. Sebastian, *The Elastoplastic Response of Poly(Methyl Methacrylate) to Indentation*. Proceedings of the Royal Society of London A, 1996. **452**: p. 439-457.

97. H. Li and A. H. W. Ngan, *Size effects of nanoindentation creep*. Journal Of Materials Research, 2004. **19**(2): p. 513-522.
98. E. S. Berkovich, *Three-Faceted Diamond Pyramid for Micro-Hardness Testing*. Industrial Diamond Review Journal, 1951. **11**: p. 129-132.
99. A. Hodzic, Z. H. Stachurski, et al., *Nano-Indentation of Polymer-Glass Interfaces Part I. Experimental and Mechanical Analysis*. Polymer, 2000. **41**(18): p. 6895-6905.
100. S. H. Lee, S. Wang, et al., *Evaluation of Interphase Properties in a Cellulose Fiber-Reinforced Polypropylene Composite by Nanoindentation and Finite Element Analysis*. Composites: Part A, 2007. **38**: p. 1517-1524.
101. M. MirafTAB, *Basic Principles of Fatigue*, in *Fatigue Failure of Textile Fibres*, M. MirafTAB, Editor. 2009, Elsevier. p. 3-4.
102. W. A. J. Albert, *Uber Treibseile am Harz*. Archiv Ffir Mineralogie, Geognosie. Bergbau UndHiittenkunde, 1837. **10**: p. 215-234.
103. M. MirafTAB, *Basic principles of fatigue*, in *Fatigue failure of textile fibres*, M. MirafTAB, Editor. 2009, Elsevier. p. 11.
104. J. Militky and S. Ibrahim, *Effect of textile processing on fatigue*, in *Fatigue Failure of Textile Fibers*, M. MirafTAB, Editor. 2009, Woodhead Publishing.
105. J. F. Mandell, *Fatigue Behaviour of Short Fibre Composite Materials*, in *Fatigue of Composite Materials*, K. L. Reifsnider, Editor. 1990, Elsevier Science Publishers B. V.: The netherlands. p. 232-337.
106. J. T. Krause, *Zero Stress Strength Reduction and Transitions in Static Fatigue of Fused Silica Fiber Lightguides*. Journal of Non-Crystalline Solids, 1980. **38-39**: p. 497-502.
107. M. J. Matthewson and C. R. Kurkjian, *Static Fatigue of Optical Fibers in Bending*. Journal of the American Ceramic Society, 1987. **70**(9): p. 662-668.
108. A. R. Bunsell and J. W. S. Hearle, *A Mechanism of Fatigue Failures in Nylon Fibres*. Journal of Materials Science, 1971. **6**: p. 1303-1311.
109. M. Elices and J. Llorca, *Fiber Fracture*. 2002: Elsevier Science Ltd.
110. A. R. Bunsell and J. W. S. Hearle, *The Fatigue of Synthetic Polymeric Fibers*. Journal of Applied Polymer Science, 1974. **18**: p. 267-291
111. R. Olshansky and R. D. Maurer, *Tensile Strength and Fatigue of Optical Fibers*. Journal of Applied Physics, 1976. **47**: p. 4497-4499.
112. C. R. Kurkjian, J. T. Krause, et al., *Strength and Fatigue of Silica Optical Fibers*. Journal of Lighting Technology, 1989. **7**(9): p. 1360-1370.
113. S. F. Cowap and S. D. Brown, *Static Fatigue Testing of a Hermetically Sealed Optical Fiber*. American Ceramic Society Bulletin, 1984. **63**(3): p. 495.

114. M. J. Matthewson, C. R. Kurkjian, et al., *Strength Measurement of Optical Fiber by Bending*. Journal of the American Ceramic Society, 1986. **69**(11): p. 815-821.
115. Sival A Rodrigues Juniors, J. L. Ferracane, et al., *Flexural Strength and Weibull Analysis of a Microhybrid and a Nanofill Composite Evaluated by 3- and 4-point Bending Tests*. Dental Materials, 2008. **24**(3): p. 426–431.
116. G. J. Nelson, M. J. Matthewson, et al., *A Novel Four-Point Bend Test for Strength Measurement of Optical Fibers and Thin Beams-Part I: Bending Analysis*. Journal of Lightwave Technology, 1996. **14**(4): p. 555-563.
117. J. Degrieck and W. V. Paepegem, *Fatigue Damage Modeling of Fibre-Reinforced Composite Materials: Review*. Applied Mechanics Reviews, 2001. **54**(4): p. 279-300.
118. C. Qian, R. P. L. Nijssen, et al. in *14th European Conference on Composite Materials*. 2010. Budapest, Hungary.
119. G. P. Sendeckyj, *Fitting Models to Composite Materials Fatigue Data*, in *Test Methods and Design Allowables for Fibrous Composites (2nd)*, C. C. Chamis, Editor. 1989, American Society for Testing and Materials. p. 245-260.
120. R. Drobina, A. Włochowicz, et al., *Fatigue Curves Elaborated for Selected Worsted Wool Yarns*. Fibres & Textiles in Eastern Europe 2007. **5-6**(64): p. 54-58.
121. P. Kittl and G. Díaz, *Weibull's Fracture Statistics, or Probabilistic Strength of Materials: State of the Art*;. Res Mechanica, 1988. **24**: p. 99-207.
122. H. D. Wagner, *Stochastic Concepts in the Study of Size Effects in the Mechanical Strength of Highly Oriented Polymeric Materials*. Journal of Polymer Science Part B: Polymer Physics, 1989. **27**: p. 115-149.
123. M. Meloun and J. Militký, *Experimental Data Treatment*. 2011, New Delhi: Woodhead Publishing.
124. G. W. Cran, *Moment Estimators for the 3-Parameter Weibull Distribution*. IEEE Transactions on Reliability, 1988. **37**: p. 360-362.
125. D. Kremenakova, R. Mishra, et al., *Selected Topics of Textile and Material Science*. 2011, Pilsen: Publishing House of WBU.
126. J. Wyckoff, L. J. Bain, et al., *Some Complete and Censored Sampling Results for the Three-Parameter Weibull Distribution*. Journal of Statistical Computation and Simulation, 1980. **11**(2): p. 139-151.
127. B. Zenbil, *Estimation Techniques for A Class of Non Regular Distributions*. 1991, Middle East Technical University: Ankara.
128. S. H. Zanakos, *A Simulation Study of Some Simple Estimators for the Three-Parameter Weibull Distribution*. Journal of Statistical Computation and Simulation 1979. **9**(2): p. 101-116.

129. P. Cooke, *Statistical Inference for Bounds of Random Variables* Biometrika, 1979. **66**(2): p. 367-374
130. H. Rinne, *The Weibull distribution A handbook*. 2009, Boca Raton: Chapman & Hall.
131. G. McLachlan and D. Peel, *Finite Mixture Models*. Wiley Series in Probability and Statistics, ed. S. S. W. Walter A. Shewhart. 2005.
132. J. R. Schaff and B. D. Davidson, *Life Prediction Methodology for Composite Structures: Part I-Constant Amplitude and Two-Stress Level Fatigue*. Journal of Composite Materials, 1997. **31**: p. 128-157.
133. H. T. Hahn and R. Y. Kim, *Fatigue Behavior of Composite Laminates*. Journal of Composite Materials 1976. **10**: p. 156-180.
134. T. K. O'Brien and K. L. Reifsnider, *Fatigue Damage Evaluation Through Stiffness Measurements in Boron-Epoxy Laminates*. Journal of Composite Materials, 1981. **15**: p. 55-70.
135. W. J. Duncan, P. W. France, et al., *The effect of Environment on the Strength of Optical Fiber*, in *Strength of Inorganic Glasses*, C. R. Kurkjian, Editor. 1985: New York.
136. R. Joffe, J. Andersons, et al. *Application of Weibull Strength Distribution for Cellulose Fibers with Highly Non-Linear Behavior*. in *17th International Conference on Composite Materials*. July 27-31, 2009. Edinburgh, United Kingdom.
137. N. Pan, H. C. Chen, et al., *The Size Effects on the Mechanical Behaviour of Fibres*. Journal of Material Science, 1997. **32**: p. 2677-2685.
138. M. Yao, *Textile Material Science (3rd, in Chinese)*. 2009, China: China Textile & Apparel Press.
139. J. Cheng, M. F. Fu, et al., *Mechanical and Photoplasticity Research of Polymethyl Methacrylate (in Chinese)*. Journal of Tianjing University, 2000. **33**(1): p. 85-87.
140. S. H. Lee, S. Q. Wang, et al., *Evaluation of Interphase Properties in a Cellulose Fiber-Reinforced Polypropylene Composite by Nanoindentation and Finite Element Analysis*. Composites, Part A: Applied Science and Manufacturing, 2001. **38**: p. 1517-1524.
141. T. H. Courtney, *Mechanical Behavior of Materials*. 1990, New York: McGraw-Hill, Inc.
142. S. Yang, Y. W. Zhang, et al., *Analysis of Nanoindentation Creep for Polymeric Materials*. Journal of Applied Physics, 2004. **95**(7): p. 3655-3666.
143. V. Raman and R. Berriche, *An Investigation of the Creep Processes in Tin and Aluminum using a Depth-Sensing Indentation Technique*. Journal of Materials Research, 1992. **7**(3): p. 627-638.
144. A. K. Bhattacharya and W. D. Nix, *Analysis of Elastic and Plastic Deformation Associated with Indentation Testing of Thin Films on Substrates*. International Journal of Solids and Structures, 1988. **24**(12): p. 1287-1298.

145. G. Feng and A. H. W. Ngan, *Effects of Creep and Thermal Drift on Modulus Measurement using Depth-Sensing Indentatio*. Journal Of Materials Research, 2002. **17**(3): p. 660-668.
146. B. Tang and A. H. W. Ngan, *Accurate Measurement of Tip-Sample Contact Size during Nanoindentation of Viscoelastic Materials*. Journal of Materials Research, 2003. **18**(5): p. 1141-1148.
147. <http://www.baike.com/wiki/PTFE>
148. Y. J. Tong and D. H. Isaac, *Impact and fatigue behaviour of hemp fibre composites*. Composites Science and Technology, 2007. **67**(15-16): p. 3300-3307.
149. J. K. Kim, M. L. Sham, et al., *Nanoscale Characterisation of Interphase in Silane Treated Glass Fibre Composites*. Composites Part A: Applied Science and Manufacturing, 2001. **32**(5): p. 607-618.

Chapter 8 Publications

8.1 Publications in journals

1. J. Huang, D. Kremenakova, and J. Militky, *Flex Fatigue of Side Emitting Optical Fiber*. Advanced Materials and Engineering Materials, 2013. **683**: p. 425-430.
2. J. Huang, D. Kremenakova, and J. Militky, *Hardness Properties of Plastic Optical Fibers by Nanoindentation*. Tekstil Ve Konfeksiyon, 2014. **24**(4): p. 333-338.
3. J. Huang, D. Kremenakova, and J. Militky, *Flex Fatigue Behavior of Plastic Optical Fibers with Low Bending Cycles*. Autex Research Journal, 2015. **15**(2): p. 112-115.
4. J. Huang, D. Křemenáková, J. Militký, and F. B. Mazari, *Strength Distribution of PMMA Plastic Optical Fiber*. Industria Textila, 2015. **5**: p. 265-268.
5. J. Huang, D. Křemenáková, J. Militký, and J. Wiener, *Enhancing Side Illumination of Plastic Optical Fiber by using TiO₂ Particles and CO₂ Laser*. Journal of Laser Applications, 2015. **27**(3).
6. J. Huang, D. Křemenáková, J. Militký, G. Zhu, and Y. Wang, *Evaluation of Illumination Intensity of Plastic Optical Fibers with TiO₂ Particles by Laser Treatment*. Autex Research Journal, 2015. **15**(1): p. 13-18.
7. J. Huang, D. Křemenáková, J. Wiener, J. Militký, and M. Kašparová, *Image Analysis of Micro-Lenses Plastic Optical Fiber by Laser Cutting*. Journal of Russian Laser Research, Under Review, 2015.
8. J. Huang, J. Wiener, D. Křemenáková, and M. Kašparová, *Enhancement of Illumination Polymeric Optical Fiber with Lens End by CO₂ Laser Cutting*. Journal of Laser Applications, Under Preparation, 2015.
9. J. Huang, B. K. Behera, D. Křemenáková, and J. Militký, *Tension-Tension Fatigue of Polymeric Optical Fiber*. Fibers and Polymers, Under Preparation, 2015.
10. J. Huang, D. Křemenáková, J. Militký, V. Lédl, and L. Klara, *Improvement and Evenness of Side Illuminating Effect of Plastic Optical Fibers by Fluorescent Polyester Fabric*. Textile Research Journal, Under Preparation, 2015.
11. D. Kremenakova, J. Militky, and J. Huang, *Characterization of Polypropylene Staple Yarns by Acoustic Dynamic Modulus*. Local Mechanical Properties IX, 2014. **586**: p. 3-7.
12. F. B. Mazari, A. Mazari, D. Kremenakova, and J. Huang, *Effect of UV-Weathering on Flex Fatigue of Plastic Optical Fiber*. Industria Textila, 2015. **66**(4): p. 171-175.

8.2 Publications in book chapters

1. J. Huang, D. Křemenáková, J. Militký, and B. Meryová, *Review on Polymeric Optical Fibers*, in *Selected Properties of Functional Materials*, D. Křemenáková, R. Mishra, J. Militký, J. J. Mareš, and J. Šesták, Editors. 2013: Czech Republic. p. 55-92.

2. R. Mishra, J. Militký, V. Baheti, J. Huang, B. Kale, M. Venkataraman, V. Bele, V. Arumugam, G. Zhu, and Y. Wang, *The Production, Characterization and Applications of Nanoparticles in the Textile Industry*, in *Textile Progress*. 2014. p. 133-226.

8.3 Publications in conferences

1. J. Huang and D. Křemenáková. *Flex Fatigue of Plastic Optical Fiber*. in *Světlanka Workshop*. September 18-20, 2012. Liberec, Czech Republic.
2. J. Huang, D. Křemenáková, and J. Militký. *Flex Fatigue Behaviour of Side Emitting Optical Fiber*. in *Structure and Structural Mechanics of Textiles*. December 3-4, 2012. Liberec, Czech Republic.
3. J. Huang, D. Křemenáková, and J. Militký. *Loading Time Sensitivity of Nanoindentation Creep of Polymeric Optical Fiber*. in *Structure and Structural Mechanics of Textiles*. December 3-4, 2012. Liberec, Czech Republic.
4. J. Huang, D. Křemenáková, and J. Militký. *Flex Fatigue of Side Emitting Optical Fiber*. in *Advanced Materials and Engineering Materials*. December 16-17, 2012. Advanced Materials and Engineering Materials.
5. J. Huang, D. Křemenáková, J. Militký, M. Venkataraman, and Y. Wang. *Interphase Properties in Plastic Optical Fiber by Nanoindentation*. in *TexSci*. September 23-25, 2013. Liberec, Czech Republic.
6. J. Huang, D. Křemenáková, J. Militký, M. Venkataraman, and G. Zhu. *Mechanical Properties of PMMA Plastic Optical Fibers by Nanoindentation*. in *TexSci*. September 23-25, 2013. Liberec, Czech Republic.
7. J. Huang and B. Meryová. *Enhancement of Side emission of Plastic Optical Fibers by Laser treatment*. in *Světlanka workshop*. September 18-20, 2013. Liberec, Czech Republic.
8. J. Huang, L. Klara, D. Křemenáková, J. Militký, G. Zhu, and Y. Wang. *Side Illumination of Optical Fibers Wrapped with Fabric*. in *International Conference on Technical Textiles and Nonwovens*. November 6-8, 2014. Indian Institute of Technology Delhi, India.
9. J. Huang, D. Křemenáková, and J. Militký. *Nanoindentation Properties of Plastic Optical Fiber Interphase*. in *Nanocon*. November 5-7, 2014. Brno, Czech Republic, EU.
10. J. Huang, D. Křemenáková, J. Militký, G. Zhu, and Y. Wang. *Evaluation of Illumination Intensity of Plastic Optical Fibers with TiO₂ Particles by Laser Treatment*. in *14th Autex World Textile Conference*. May 26-28, 2014. Bursa, Turkey.
11. J. Huang, D. Křemenáková, J. Militký, G. Zhu, Y. Wang, and M. Venkataraman. *Side Illumination of Plastic Optical Fibers Wrapped with Fabrics*. in *Workshop Světlanka*. September 16-19, 2014. Rokytnice nad Jizerou, Czech Republic.

12. J. Huang, D. Křemenáková, Y. Wang, G. Zhu, and M. Venkataraman. *Strength Distribution of PMMA Plastic Optical Fiber*. in *Fibers for Progress*. May 21-23, 2014. Liberec, Czech Republic.
13. J. Huang, D. Křemenáková, X. Xiong, T. Yang, G. Zhu, and Y. Wang. *Lighting Effect of Plastic Optical Fiber Wrapped with Fluorescent Fabric*. in *20th International Conference Structure and Structural Mechanics of Textiles*. December 1-2, 2014. Liberec, Czech Republic.
14. D. Křemenáková, J. Militký, and J. Huang. *Characterization of Polypropylene Staple Yarns by Acoustic Dynamic Modulus*. in *9th Local Mechanical Property*. November 7-9, 2012. Levoča, Slovak Republic.
15. M. Venkataraman, R. Mishra, J. Huang, Y. Wang, and G. Zhu. *Evaluation of Thermal Properties of High Performance Nonwoven Padding Fabric*. in *TexSci*. September 23-25, 2013. Liberec, Czech Republic.
16. Y. Wang, J. Wiener, R. Mishra, G. Zhu, M. Venkataraman, J. Huang, and J. Militký. *Study on Ozone Treatment of Aramid Fabrics*. in *TexSci*. 2013. Liberec, Czech Republic.
17. Y. Wang, J. Wiener, G. Zhu, and J. Huang. *Sorption Property of Polyamide Nanofibrous Membrane on Dyestuff for Purifying Wastewater*. in *Nanocon*. October 16-18, 2013. Brno, Czech Republic.
18. Y. Wang, J. Wiener, G. Zhu, J. Huang, and M. Venkataraman. *Apparatus Assembling for Continual Filtration Study of Filter Membrane*. in *TexSci*. September 23-25, 2013. Liberec, Czech Republic.
19. G. Zhu, D. Křemenáková, Y. Wang, J. Huang, and J. Militký. *Study on Heat of Liquid Adsorption of Cotton Fabric*. in *Světlnka workshop*. September 18-20, 2013. Liberec, Czech Republic.
20. G. Zhu, D. Křemenáková, Y. Wang, J. Huang, M. Venkataraman, and J. Militký. *Evaluation of Thermal Conductivity of Hollow Fiber Padding by Experiment*. in *TexSci*. September 23-25, 2013. Liberec, Czech Republic.
21. G. Zhu, J. Militký, Y. Wang, H. Juan, and D. Křemenáková. *Comparison of Effective Thermal Conductivity of Hollow Fibers by Prediction Models and FE Method*. in *AMSED*. September 21-23, 2013. Singapore.
22. J. Militký, D. Křemenáková, J. Huang, and A. P. Aneja. *Flex Fatigue of PET/PEN Fibers*. in *4th International Conference on Textile and Material Science* August 27-28, 2014. Ružomberok, Slovak Republic.
23. Y. Wang, J. Winner, G. Zhu, and J. Huang. *Constant On-line Apparatus to Investigate Filtration*. in *Fiber for Progress*. May 21-23, 2014. Liberec, Czech Republic.
24. Y. Wang, J. Winner, G. Zhu, and J. Huang. *Characterization of Polyamide 6 Nanofibrous Membrane by BET Theory*. in *ICCE-22*. July 13-19, 2014. Malta.

25. Y. Wang, J. Winner, G. Zhu, and J. Huang. *Sorption Kinetics Analysis of Acid Dye on Polyamide6 Nanofibers under Different PH.* in *20th International Conference Structure and Structural Mechanics of Textiles*. December 1-2, 2014. Liberec, Czech Republic.

Annex I

J_ID: JLAPEN DOI: 10.2351/1.4919125 Date: 23-April-15 Stage: Page: 1 Total Pages: 8

PROOF COPY [15004R1] 008503JLA

JOURNAL OF LASER APPLICATIONS

VOLUME 27, NUMBER 3

AUGUST 2015

Enhancing side illumination of plastic optical fiber by using TiO₂ particles and CO₂ laser

Juan Huang,^{a)} Dana Křemenáková, Jiří Militký, and Jakub Wiener

Department of Material Engineering, Faculty of Textile Engineering, Technical University of Liberec, Liberec 461 17, Czech Republic

(Received 16 January 2015; accepted for publication 16 April 2015; published xx xx xxxx)

Plastic optical fiber (POF) is highly appreciated for its applications in glowing textiles. However, fabricating thin POF with good side illuminating effect is a challenge due to the complicated manufacturing processes. CO₂ laser treatment is normally applied to enhance the surface roughness without significant influence on other properties of materials. Titanium dioxide (TiO₂) is widely studied for its high photo activity and thermal stability. The surface modification combined with TiO₂ particles and CO₂ laser treatment was carried out to investigate the side illuminating effect of POF. The images of surface morphology show that TiO₂ particles reduce the thermal damage of POF surface during CO₂ laser treatment. The results from side illumination testing prove that the employment of TiO₂ particles, combined with CO₂ laser treatment, could enhance the side illumination of POF for longer lasting application. Cyclic CO₂ laser treatment can decrease the heat accumulation in POF and may have adverse effect on side illumination. The investigation of tensile testing indicates that only the strain value is more influenced by laser treatment due to the brittleness and low thermal stability of POF material. © 2015 Laser Institute of America. [<http://dx.doi.org/10.2351/1.4919125>]

Key words: plastic optical fiber, side illumination, CO₂ laser, TiO₂ particles

I. INTRODUCTION

Plastic or polymeric optical fiber (POF) is widely utilized as an excellent medium in short haul data communications links based on total internal reflection theory due to its flexibility, anti-impaction, easy installation, large numerical aperture, and affordability. The main applications of POFs in textiles are separated into two aspects, namely, glowing textiles¹⁻⁴ and sensing textiles.⁵ In these fields, POFs with thin diameter can be woven, braided, or knitted with traditional textile yarns (flex, cotton, wool, etc.) into fabric structures, for various decorative and lighting patterns. Apart from the amazing visual art effect, the integration of POFs with textiles is also beneficial to human safety.⁶ POFs can be used to enhance the active safety elements in developing jackets that glow in the nights and can be useful for sportsmen, firemen, and policemen. For these applications, sufficient side illuminating effect is necessary.

In side-emitted optical fiber, light can escape from fiber surface due to either the surface defects or the small difference between core refractive index and cladding refractive index. Hence, it shows stronger lighting effect as compared to end emitting optical fiber. Side emitting POFs with small diameter are difficult to manufacture and therefore a lot of efforts have been devoted to the development of side illumination of optical fibers by surface modifications.⁷⁻¹⁰ The surface is modified using both physical and chemical methods. The physical methods are side notches, asymmetry of

core and cladding geometry, micro bends of fiber and surface abrasion while chemical methods are solvent etching and addition of radiation scattering particles into fiber cladding.

Laser is an energy source that can be applied directly onto the materials with desired power and intensity. It exhibits a number of favorable properties like large beam size, high laser efficiency, easy-operation, low cost, and non-contact system. Laser surface modification is a widely accepted technology for studies on changes of surface characterizations of many materials such as polymers,¹¹ metals,¹² ceramics,¹³ woods,¹⁴ and composites.^{15,16} Laser treatment is used to enhance surface dependent properties like hardness, fatigue, and resistance to wear by treating small areas while keeping other parts unaffected.¹⁷

Titanium dioxide (TiO₂) is a widely studied photocatalyst due to high photoactivity, low toxicity, good chemical and thermal stabilities, and affordability.¹⁸ The refractive index of TiO₂ is relatively higher than that of POFs, leading to more possibility for light emitting out. Additionally, POF is sensitive to heat. It is believed that the addition of TiO₂ particles in fiber cladding would alleviate the heat damage by laser.

This contribution is an attempt to exploit the ability of enhancing the light illumination from the fiber surface by surface modifications with TiO₂ particles and CO₂ laser treatment. First, the surface of naked POFs was modified with TiO₂ particles and then treated by CO₂ laser under different conditions. The surface morphologies of POFs with and without TiO₂ particles after laser treatment were observed by

^{a)} Author to whom correspondence should be addressed; electronic mail: juan.huang@tul.cz

scanning electronic microscopy. The intensity of side illumination of POFs was measured by a self-made semiautomatic device.

II. MATERIALS AND METHODS

A. Materials

Naked POFs with 0.5 mm diameter were prepared in Grace POF Co., Ltd., Taiwan. The core polymer was polymethyl methacrylate (PMMA), and the cladding material was blended by PMMA and Polytetrafluoroethylene (Teflon); the corresponding refractive indices were 1.49 and 1.42, respectively. The minimal bending radius of POFs was 4 mm which was eight times of diameter of the fiber.

B. Methods

1. Sample preparation for laser treatment

There are two steps for sample preparation. The first step was surface modification of POFs by TiO₂ particles (Table I), as shown in Fig. 1. The original size of each TiO₂ particle was around 20 nm. TiO₂ particles are more stable in a state of aggregation. The size of aggregated TiO₂ particles was measured as 100–120 nm by laser scattering method. 2 g TiO₂ particles were mixed with 200 ml isopropyl alcohol (C₃H₈O) at 20 °C. Ultrasonic homogenizer (Ultrasound Bandelin SONOPULS mini20) was utilized to disperse TiO₂ particles evenly into isopropyl alcohol with 50% power for 1 min. The mixture with 10 g/l solid concentration was prepared. One end of POF with 500 mm length was dipped into the mixture and taken out vertically and slowly through one funnel held by small glass balls. The sample with POF full of fine TiO₂ particles on the surface was obtained after drying for 30 s at 20 °C.

Another step was sample arrangement for laser treatment. Both samples modified by TiO₂ and naked POFs were arranged horizontally and fixed by tape on a paper frame with 3 cm thickness, as given in Fig. 2. The interval between each adjacent sample was at least 2 cm in order to eliminate the effect of laser treatment on neighboring samples. The base for laser treatment was flame resistant nonwoven glass fabric.

2. Laser treatment

Laser treatment was carried out by Easy Laser-Marcatex 150/250 Flexi CO₂ laser with 50% duty cycles. The wavelength of CO₂ laser beam was 10.6 μm; the output power was 100 W; the beam size was 0.5 mm; the resolution was 27 × 27 dpi; and the pixel time varied from 30 to 100 μs. Both sides (front and back) of each sample were treated by CO₂ laser to even the surface modification.

TABLE I. Typical physical and chemical properties of TiO₂ particles.

	PK-20
TiO ₂ content (%)	>92.5
Crystal modification	Anatase
Specific surface area (m ² /g) BET (5 points)	70–110

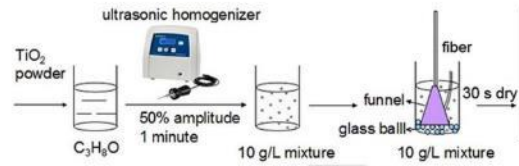


FIG. 1. Surface modification of POF by TiO₂ particles.

The scanning direction of CO₂ laser treatment was designed to be perpendicular to the fiber axis, as shown in Fig. 2. Theoretically, irrespective of scanning direction of CO₂ laser of whether perpendicular or parallel to the fiber axis, the distribution of melted spots on fiber surface should be even and the same if the diameter of laser spot is small enough and the fiber is a perfect cylinder. However, in practice, when the scanning direction is parallel to the fiber axis, the effect of CO₂ laser treatment on fiber surface is comparatively weak due to the asymmetry along fiber axis caused by macrobends during packing or imperfections in manufacturing processes. When the scanning direction is perpendicular to the fiber axis, the laser spots acting on POFs would be dense and strong. The light transmission from each rough point is different and complicated, and the detecting area of sensor (in Fig. 3) is two-dimensional (the sensor is a point detector) and limited. The obtained illumination intensity could decline if the rough points on fiber surface resulting from CO₂ laser treatment do not face the detecting area of sensor. These issues could be alleviated by using perpendicular scanning direction to the fiber axis through CO₂ laser treatment.

3. Scanning electron microscopy

The surface morphology was observed by scanning electron microscopy (SEM) VEGA TS 5130 at 20 kV acceleration voltage, after gold coating.

4. Testing of side illumination intensity

One end of sample was polished with polishing papers and diamond powder until it was smooth enough to maximize the accepted light for fiber before connecting to the

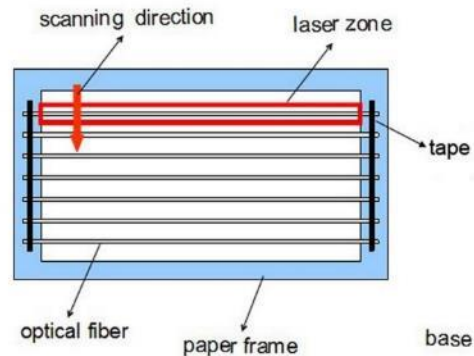


FIG. 2. Samples preparation for CO₂ laser treatment.

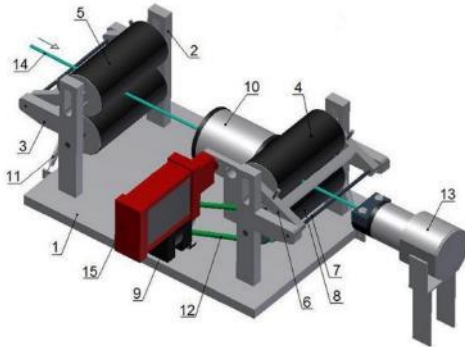


FIG. 3. Apparatus for measurement of illumination intensity of POFs: 1—mainboard, 2—spacers (4×), 3—console, 4—tow roller, 5—guide roller, 6—roller pressing bracket, 7—storage rod, 8—drive roller, 9—stepper motor, 10—tunnel, 11—springs, 12—drive belt, 13—light source, 14—sample, and 15—sensor.

light source. The spectra/wavelength of light source was white light which was the combination of all visible wavelengths. The output flux was 205 lumens.

The semiautomatic device for testing the side illumination intensity of POFs is described in Fig. 3. The sample in the elongated state was connected to the light source (13) through two sets of rollers (4 and 5), the head roller (4) was controlled by the stepper motor MSHC 100B41 Sankyo (9), the illumination intensity of sample was measured by the sensor THOR LABS PM 100 USB (15), which was connected with the computer system. The measurement was performed in a dark environment and related experimental parameters are given in Table II.

5. Tensile testing

Tensile testing was carried out on Instron-4411 at 20 °C and 65% relative humidity, in order to investigate the changes of mechanical properties of POFs before and after treatments by TiO₂ particles and CO₂ laser. The gauge length was set as 200 mm, and the testing speed was 100 mm/min. 50 times were averaged for each sample.

III. RESULTS AND DISCUSSION

A. Surface morphology

SEM results for surface morphology of POFs are shown in Fig. 4. It may be seen from the figure that the untreated POF (A) exhibits smooth surface. The treated POF (D) is dispersed with aggregated TiO₂ particles. The TiO₂ particles on fiber surfaces (E and F) are fine and less observable. As a

TABLE II. Testing condition of illumination intensity of POFs.

Parameters	Value (mm)
Step size	5
Length measured	200
Fiber length	500
Distance between light source and sensor	175

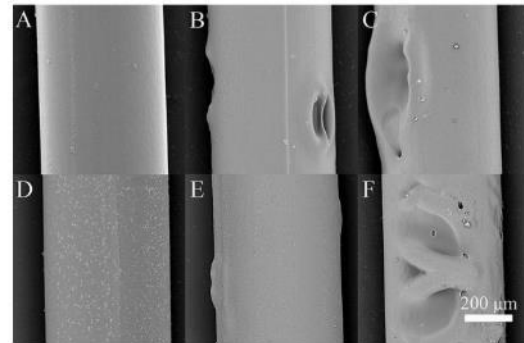


FIG. 4. Surface images of samples treated by CO₂ laser with different pixel time. POFs without TiO₂ particles: (a) 0 μ s, (b) 100 μ s, and (c) 150 μ s; POFs with TiO₂ particles: (d) 0 μ s, (e) 100 μ s, and (f) 150 μ s.

matter of fact, POF can hold only parts of TiO₂ particles properly. The TiO₂ particles with the diameter above 300 nm are too large to penetrate by diffusion deeper into the fiber mass. The TiO₂ particles are adsorbed on the fiber surface by physical interactions (such as hydrophobic forces, hydrogen bonds, and van der Waals forces) rather than chemical bonds. During the processes of laser treatment, some TiO₂ particles might be detached from POF surface.

There are significant differences between samples before and after CO₂ laser treatment. The dimensions of melted holes on POFs with TiO₂ particles (E and F) are obviously smaller than those without TiO₂ particles (B and C). It can be implied that TiO₂ particles could ease the surface damage during CO₂ laser treatment due to the low coefficient of thermal conductivity of TiO₂ particles. The usage of TiO₂ particles can enhance the thermal stability of POF.

Long pixel time gives high laser energy and more laser treating time in CO₂ laser treatment, resulting in acceleration of thermal damage and severe fiber destruction due to limited thermal resistance of PMMA. There are visible “necks” and melted holes distributed on POF when the pixel time is above 150 μ s, leading to decreasing optical property of POF and increasing possibility of POF fracture.

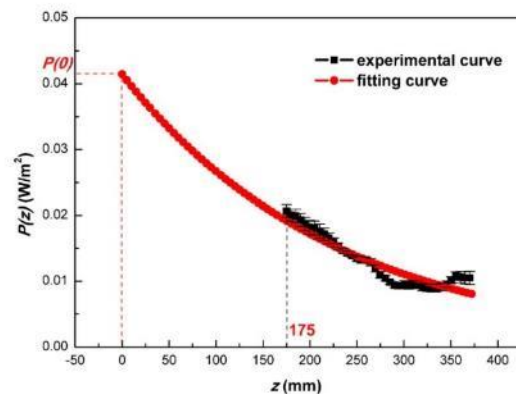


FIG. 5. Comparison of experimental curve and fitting curve: POF with TiO₂ particles after CO₂ laser treatment at 70 μ s pixel time.

TABLE III. Parameters of side illumination of POFs with and without TiO₂ particles before CO₂ laser treatment.

Fiber state	$P(0)$ (W/m ²)	$P(z = 375 \text{ mm})$ (W/m ²)	a (dB/mm)
Without TiO ₂ particles	0.020	0.0055	0.015
With TiO ₂ particles	0.032	0.0057	0.020

B. Intensity of side illumination

The attenuation coefficient a in decibel per unit length is usually determined by the input optical power $P(0)$ and the output optical power $P(z)$, and described as follows:^{19–21}

$$az = 10 \times \log_{10}[P(0)/P(z)], \quad (1)$$

$$\log P(z) = -az/10 + \log P(0), \quad (2)$$

$$y = kx + q, \quad (3)$$

where z is the measured distance of optical fiber. The transformation equation (2) derived from Eq. (1) is related to the linear fitting curve of logarithm of output power versus measured distance, which can be represented in its general form, as shown in Eq. (3), the input power and attenuation coefficient a are expressed as

$$P(0) = 10^q, \quad (4)$$

$$a = -10 \times k, \quad (5)$$

where k and q are two parameters (slope and intercept, respectively) of the linear fitting curve. The intensity of side illumination can be estimated with Eqs. (4) and (5), as shown in Fig. 5

$$P(z) = P(0)10^{-az/10}. \quad (6)$$

1. Effect of TiO₂ particles on side illumination of POFs by CO₂ laser

Compared to POF without TiO₂ particles, POF with TiO₂ particles displays bigger values of $P(0)$ and $P(z = 375 \text{ mm})$, as given in Table III. This means TiO₂ particles could enhance the side illumination of POF at the distance of 375 mm. It can be explained by the properties of TiO₂ particles. TiO₂ particles have the refractive index of

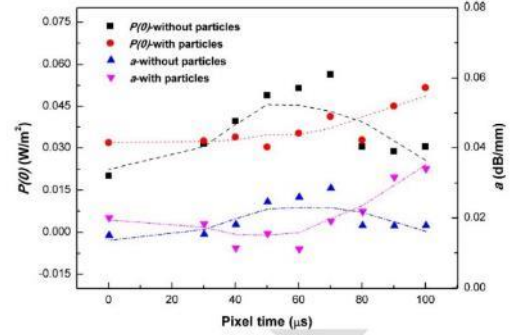


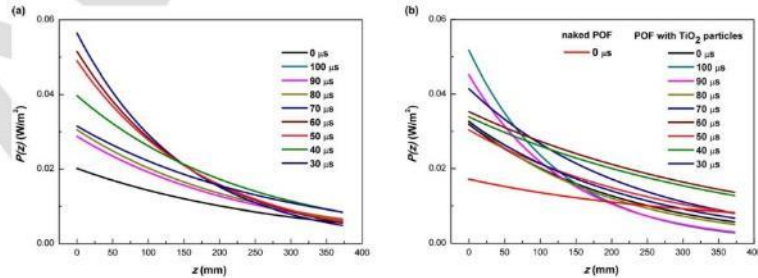
FIG. 6. Dependence of input illumination intensity and attenuation coefficient on pixel time: dots-experimental data, dashed line-smoothed data.

2.5, which is higher than PMMA. Thus, if TiO₂ particles are embedded in or covered on POF cladding, the light could be most probably refracted rather than reflected on the interface of fiber core and fiber cladding, leading to the enhanced side illumination intensity.

The side illumination intensity of POF with TiO₂ particles is less than that of POFs without TiO₂ particles if the distance arrives to a critical point of 400 mm. The modification by TiO₂ particles increases the surface roughness and opacity of POF, resulting in the proportionately incremental optical loss. It is assumed that the use of TiO₂ particles is working on the enhancement of side illumination of POF only at certain distances.

Figure 6 shows the dependences of $P(0)$ and a on pixel time. In the case of POF without TiO₂ particles, the values of input intensity and attenuation coefficient vary in the similar manner. Both of them increase gradually to reach the peak at 70 μs pixel time and then decrease with the increment of pixel time. For POF with TiO₂ particles, the input intensity goes up continuously as the pixel time increases; the attenuation coefficient goes down to the lowest point at 60 μs pixel time and rises evidently after that.

It implies that CO₂ laser treatment could play an effective role in enhancing the side illumination in some cases (in term of measured distance), as shown in Fig. 7(a). All POFs display stronger side illuminating effect with the distance of 375 mm, while only POFs treated at 40 and 70 μs pixel time can continue the enhanced side illumination at the distance

FIG. 7. Simulated curves of side illumination intensity versus distance: (a) POFs without TiO₂ particles and (b) POFs with TiO₂ particles.

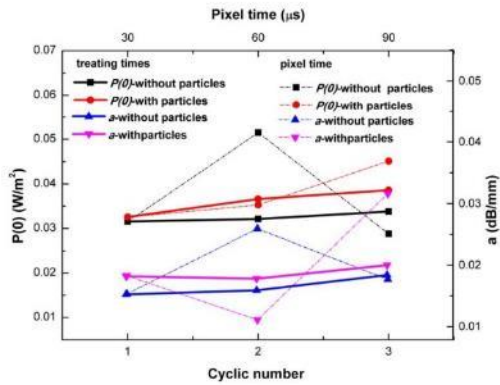


FIG. 8. Comparison of input illumination intensity and attenuation coefficient between normal laser treatment and cyclic laser treatment with the same total pixel time.

more than 375 mm, this longer distance is still limited due to the higher attenuation coefficient in both cases than that in untreated POF.

The combined treatment of TiO₂ particles and CO₂ laser might have a positive effect on enhancement of side illumination for POF in a relatively long distance, since TiO₂ particles can reduce the attenuation coefficient and give high input intensity when the pixel time is less than 80 μs, as shown in Fig. 7(b). The best results can be found at 40 and 60 μs pixel time, which could lead to stronger side illumination at longer distance compared with the best conditions for naked POFs.

2. Effect of cyclic CO₂ laser treatment on side illumination of POFs

Cyclic laser treatment was considered in order to reduce the heat accumulation inside POF during CO₂ laser treatment. Even though the laser energy and treating time rise with the higher pixel time, the laser energy is still unclear in this study. The smallest pixel time (30 μs) is considered for the cyclic laser treatment regarding to the low thermal stability of POF.

According to the results in Fig. 8 (solid curves), it is found that both values of $P(0)$ and a for two samples with and without TiO₂ particles increase according to the increase

in cyclic number. It is difficult to estimate the enhancement of side illuminating effect by the values of $P(0)$ and a . Only if $P(0)$ increases and a decreases, the side illumination should increase, on the contrary, only if $P(0)$ decreases and a increases, the side illumination should decrease. Combined with the results with 30 μs pixel time in Fig. 9, it reveals that cyclic laser treatment would lead to reduced side illumination of naked POF at the distance of 375 mm, and strengthen side illumination of POF with TiO₂ particles in the same distance.

In addition, the results also indicate that addition of TiO₂ particles could not enhance the side illumination in the case of one cyclic number laser treatment at 30 μs pixel time. However, TiO₂ particles can improve the thermal stability of the whole sample during laser treatment and thereby enhance the side illumination under certain conditions (pixel time and measured length). When the pixel time is 30 μs, the influence of improved thermal stability by TiO₂ particles on side illumination might be smaller than the influences of opacity and higher surface roughness, resulting in higher optical loss. When the pixel time is 40 or 60 μs, the light attenuation is controlled and side illumination is enhanced by TiO₂ particles.

In order to specify the effect of cyclic laser treatment, the results between normal laser treatment and cyclic laser treatment are compared at the same total pixel time. That is to say, the results from laser treatments with two cyclic number and three cyclic number are compared with those from normal laser treatments at 60 μs pixel time and 90 μs pixel time, respectively.

For naked POF, cyclic laser treatment shows lower values of both input intensity and attenuation coefficient at total 60 μs pixel time and higher values of both input intensity and attenuation coefficient at total 90 μs pixel time than normal laser treatment. For POF with TiO₂ particles, the phenomena are opposite. Combined with the results in Fig. 9, it demonstrates when the total pixel time is 90 μs, the cyclic treatment is effective on enhancement of side illumination of both POFs with and without TiO₂ particles.

During the processes of continuous cyclic laser treatment, the effects of CO₂ laser treatment and TiO₂ particles are more complicated. After each cyclic laser treatment, samples would not be in the same state (straight state at the beginning) and become loose gradually. The treated points on fiber surface might shift from the previous ones. As a result, the dimensions and the number of holes could not be estimated. The

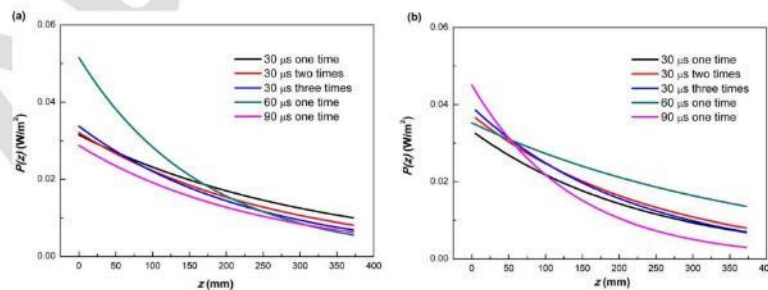


FIG. 9. Simulated curves of side illumination versus distance of samples for cyclic laser treatment: (a) without TiO₂ particles and (b) with TiO₂ particles.

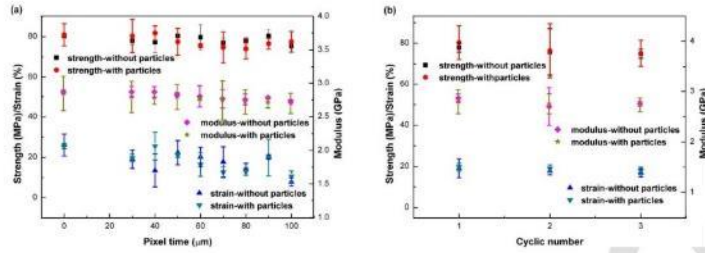


FIG. 10. Tensile properties of samples after CO₂ laser treatment: (a) normal treatment and (b) cyclic treatment.

holes might be deep, narrow, and with less number, or shallow, narrow, and with more number, or shallow, border with less number. Both thermal damage and deviation of fiber axis are considered as the possible reasons for light attenuation.²² Consequently, the light transmission and side illuminating effect become complicated and unexpected.

C. Mechanical properties

Initially, there is no significant change in mechanical properties by using TiO₂ particles for both normal laser treatment and cyclic laser treatment, as shown in Fig. 10. Gradually, there is perceptible change in mechanical properties according to the increasing pixel time of CO₂ laser treatment. Both tensile strength and modulus for all samples decrease slightly, but strain declines obviously with increasing pixel time. It is contributed to the low thermal stability and brittleness of POF itself. The working temperature is in the range of -20—+70 °C. When laser energy reaches or exceeds this limit, the brittle POF displays severe damage and is easy to break, as shown in Fig. 11.

IV. CONCLUSIONS

The surface treatments of POFs with TiO₂ particles and CO₂ laser were employed to investigate the side illuminating effect of POFs. With normal CO₂ laser treatment with the pixel time from 30 up to 100 μs, the side illumination of naked POFs could be enhanced only in a limited distance. This may be attributed to large input intensity and attenuation coefficient.

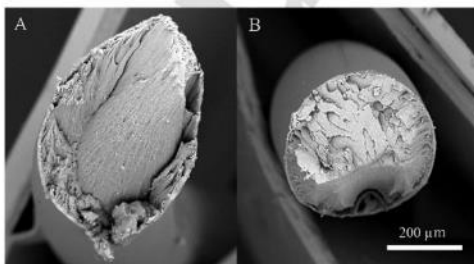


FIG. 11. Fracture images of samples: (a) untreated POF, (b) naked POF after CO₂ laser treatment with 100 μs pixel time.

The use of TiO₂ particles improves the thermal stability of POF and reduces the transparency of POF simultaneously. If the influence of improved thermal stability on side illumination is dominant, the side illumination might increase in a long distance; if the influence of reduced transparency on side illumination is major, the side illumination might decrease beyond a short distance. Overall, the combination of TiO₂ particles and laser treatment can benefit the side illumination to an extent.

Cyclic laser treatment has more complicated effect on side illumination. Since the laser spots are not guaranteed to act in the same areas on sample surface, the side illumination is difficult to estimate accordingly due to the unexpected influences on light transmission. Compared to normal laser treatment in terms of the same total pixel time, the cyclic laser treatment only with total 90 μs pixel time might work on the enhancement of side illumination of both naked POF and POF with TiO₂ particles in certain distance.

TiO₂ particles play less significant role in tensile properties of POF than CO₂ laser treatment which weakens the strain value with increasing pixel time due to the thermal defects on fiber surface and the brittleness of fiber material.

The side illumination is dependent on input intensity, attenuation coefficient as well as the measured distance. The long fiber length should be considered. If the laser energy is clear with each pixel time, it would be easy to understand the heat transfer in the testing environment during CO₂ laser treatment.

ACKNOWLEDGMENT

This work was supported under SGS project-48006 by Technical University of Liberec.

- ¹A. Harlin, H. Myllymaki, and K. Grahn, "Polymeric optical fibres and future prospects in textile integration," *Autex Res. J.* **2**, 132–143 (2002).
- ²A. Harlin, M. Makinen, and A. Vuorivirta, "Development of polymeric optical fibre fabrics as illumination elements and textile displays," *Autex Res. J.* **3**, 1–8 (2003).
- ³J. C. Wang, B. Yang, B. H. Huang, and Z. M. Jin, "Design and development of polymeric optical fiber jacquard fabric with dynamic pattern display," *Text. Res. J.* **82**, 967–974 (2012).
- ⁴J. C. Wang, B. H. Huang, and B. Yang, "Effect of weave structure on the side-emitting properties of polymer optical fiber jacquard fabrics," *Text. Res. J.* **83**, 1170–1180 (2013).
- ⁵K. Krebber, S. Liehr, and J. Witt, "Smart technical textiles based on fiber optic sensors," *Proc. SPIE* **8421**, 319–344 (2012).

- ⁶D. Křemenáková, V. Lédl, J. Militký, B. Bübelová, and B. Meryová, "Certified product n. 24997 active illuminating safety product," patent office CZ.4.3 (2013).
- ⁷M. H. Im, E. J. Park, and C. H. Kim, "Modification of plastic optical fiber for side-illumination," *Human-Comput. Interact.* **4551**, 1123–1129 (2007).
- ⁸J. Spigulis, D. Pfafrods, M. Stafekis, and W. Jelinska, "The "glowing" optical fibre designs and parameters," *Proc. SPIE*, **2967**, 231–236 (1996).
- ⁹M. Zajkowski, "Emission of flux light in "side light" fiber optic," *Proc. SPIE*, **5125**, 322–327 (2002).
- ¹⁰J. Shen, X. M. Tao, D. Q. Ying, C. Y. Hui, and G. F. Wang, "Light-emitting fabrics integrated with structured polymer optical fibers treated with an infrared CO₂ laser," *Text. Res. J.* **0**, 1–10 (2012).
- ¹¹M. F. Jensen, M. Noerholm, L. H. Christensen, and O. Geschke, "Microstructure fabrication with a CO₂ laser system: Characterization and fabrication of cavities produced by raster scanning of the laser beam," *Lab Chip* **3**, 302–307 (2003).
- ¹²G. Duffet, P. Sallamand, and A. B. Vannes, "Improvement in friction by cw Nd:YAG laser surface treatment on cast iron cylinder bore," *Appl. Surf. Sci.* **205**, 289–296 (2003).
- ¹³P. P. Shukla and J. Lawrence, "Fracture toughness modification by using a fibre laser surface treatment of a silicon nitride engineering ceramic," *J. Mater. Sci.*, **45**, 6540–6555 (2010).
- ¹⁴A. Petutschnigg, M. Stöckler, F. Steinwendner, J. Schnepfs, H. Güttler, J. Blinzer, H. Holzer, and T. Schnabel, "Laser treatment of wood surfaces for ski cores: An experimental parameter study," *Adv. Mater. Sci. Eng.* **2013**, 1–7.
- ¹⁵J. Wiener and S. Shahidi, "Morphological and mechanical changes of glass fibers mat by CO₂ laser," *J. Text. Inst.* **105**, 187–195 (2014).
- ¹⁶S. Dadbin, "Surface modification of LDPE film by CO₂ pulsed laser irradiation," *Eur. Polym. J.* **38**, 2489–2495 (2002).
- ¹⁷W. M. Steen, "Review article: Laser material processing—an overview," *J. Opt. A: Pure Appl. Opt.* **5**, S3–7 (2003).
- ¹⁸Y. Wang, Y. Huang, W. Ho, L. Zhang, Z. Zou, and S. Lee, "Biomolecule-controlled hydrothermal synthesis of C-N-S-tridoped TiO₂ nanocrystalline photocatalysts for NO removal under simulated solar light irradiation," *J. Hazard. Mater.* **169**, 77–87 (2009).
- ¹⁹M. Zajkowski, "Emission of flux light in "side light" fiber optic," *Proc. SPIE* **5125**, 322–327 (2002).
- ²⁰M. Zajkowski, "Luminous flux emission calculation analysis in side light illumination optical fibers," *Proc. SPIE* **5775**, 440–445 (2005).
- ²¹S. Kwan, "Principles of optical fibers," in *Partial Fulfillment of Course Requirement for MatE 115* (San Jose State University, California, 2002).
- ²²W. Daum, J. Krauser, P. E. Zamzow, and O. Ziemann, *POF: Polymer Optical Fibers for Data Communication* (Springer, Berlin, 2002), Chap. 6, pp. 225–250.